Digital Signal Processing in Coherent Optical Radio over Fiber Systems

Neda Nabavi

A thesis submitted in partial fulfillment of the requirements for the
Doctorate in Philosophy degree in Electrical and Computer Engineering

School of Electrical Engineering and Computer Science
Faculty of Engineering
University of Ottawa

© Neda Nabavi, Ottawa, Canada, 2017

Abstract

Coherent communication systems became practical with the advent of integrated electronic circuits capable of supporting Digital Signal Processing (DSP) at speeds compatible with line rates. Much of the complexity and expense of the functions required in a coherent receiver to compensate for optical channel uncertainties and impairments could be transferred to DSP algorithms. The aim of the research presented in this thesis is to develop radical breakthrough DSP algorithms and design new architectures for the digital coherent optical receiver within the RF-Cité system and optical fiber network supported distributed millimeter wave wireless antenna system.

The model of an optical channel is fundamental for understanding phase and polarization drift, chromatic dispersion, polarization mode dispersion and other drawbacks of the fiber optic systems in order for the signal processing algorithm to compensate these effects. In this thesis firstly an evaluation of the optical channel model that accurately describes the single mode fiber as a coherent transmission medium is reviewed through analytical, numerical and experimental analysis.

Secondly, an original approach to the design of a digital coherent optical receiver is proposed which can adapt to random time-varying state of polarization (SOP) for both the local oscillator and signal. To address the problem, two different methods of polarization diverse recovery of the modulation with carrier phase estimation and elimination of sign ambiguity are performed and verified by numerical simulations. The results show the accurate recovery of the modulation and error-free constellation demodulation.

Furthermore, inspired by former investigations, the theoretical analysis of a novel microwave photonic integrated circuit (MPIC) implementations of various building blocks used within the RF-Cité architecture is presented. The application of the proposed circuit in RoF systems is demonstrated by computer simulations using the Virtual Photonics Inc. software and OptiSuite packages. The performance of the proposed MPIC in a RoF system is assessed through advance modulation format techniques that have been employed in many wireless communication standards owing to their high spectral efficiency. In the DSP module, delay compensation is applied to synchronize the received signal, and the system performance is evaluated by measuring the error vector magnitude of the received signal using single-mode fiber. This scheme removes the temperature control requirement; an undesirable feature in terms of energy consumption considerations.

Also, a modified polarization demultiplexing algorithm is employed to classify the input polarizations that transmit two independent channels that are mixed randomly as the light is propagating in the optical fiber. This novel technique enables blind algorithms to accurately track polarization channel alignment, through achieving accurate polarization de-multiplexing obtained by numerical simulations and experiments.

Dedicated to

Dr. Shahin Nematizadeh

Acknowledgements

I would like to acknowledge my supervisor – Dr. Trevor James Hall, for his guidance on theory, simulation and experiments, as well as technical writing, throughout the course of my graduate studies. In addition to the unwavering support, his knowledge and diverse interest in various subject areas has enabled me to maintain multiple perspectives in research.

I would like to express my gratitude to the members of my examination committee, Dr. Karin Hinzer, Dr. Ahmad Atieh, Dr. Martin Bouchard, Dr. Sophie LaRochelle and Dr. Winnie Ye for investing time and providing valuable feedbacks. I would like to express the deepest appreciation to my committee chair, Dr. Majid Mohammadian for his encouragement and patience.

I am very thankful to Dr. Ramón Maldonado-Basilio for the valuable discussions, many of which have been inspirational and critical in helping me accomplish this work.

I would like to acknowledge Peng Liu for his assistance in experiments and experimental setup construction. Special thanks are given to Dr. Wei Yang and Dr. Sawsan Abdul-Majid for their great technical support.

Financial assistance from the University of Ottawa excellence scholarship, Ontario Graduate Scholarship (OGS), Nicole Bégin-Heick Scholarship and Natural Sciences and Engineering Research Council of Canada (NSERC) is gratefully acknowledged.

I would like to acknowledge my colleagues and friends in PTLab at University of Ottawa for their friendly supports.

I would also like to acknowledge my parents who have taught me that no challenge is too great to undertake and for their encouragement. Also, to Nasim, thank you for always believing in me. I could not have asked for a better sister. I give my sincere thanks to my brother-in-law Ali, for his encouragement during the course of this thesis and my adorable lovely cute nephew Amir, who gave me so many smiles and bringing joy during my hectic schedule and difficult situations.

Last but most important, special appreciation is expressed to Shahin, my husband; the man who has made all the difference in my life, for his everlasting encouragement and love. Thank you Shahin for being my fountain of strength during the toughest of times.

Publications

Papers published in refereed journals

N. Nabavi, T. J. Hall, "Symmetric signal and local oscillator polarization diverse coherent optical receiver", *Opt. Express* **24**(3), 2391–2405 (2016).

N. Nabavi, R. Maldonado-Basilio, and T. J. Hall, "Numerical Analysis of a Multi-Function Photonic Integrated Circuit for Coherent Radio-over-Fiber", *J Lightw. Tech.* **34**(15), 3538–3543 (2016).

N. Nabavi**,** T. J. Hall, "Tracking channel alignment in blind polarization de-multiplexing", *Opt. Commun.* **349***,* 114–121(2017).

Journal article in preparation

N. Nabavi, P. Liu, and T. J. Hall, "An Optical Channel Modeling of a Single Mode Fiber as a Coherent Transmission Medium", to be submitted to *Journal of the Optical Society of America B.* (2017).

Conferences

N. Nabavi, T. J. Hall, "Ambiguity elimination of Independent Component Analysis for polarization channel alignment tracking", proceedings of *IEEE Photonics Conference (IPC)*, Reston, VA, USA, Oct 2015.

N. Nabavi, T. J. Hall**,** "Recovering symmetry in coherent digital polarization diversity optical receiver", proceedings of *IEEE Photonics Conference (IPC)*, Reston, VA, USA, Oct 2015.

R. Maldonado-Basilio, N. Nabavi, K. Aulakh, M. Hassan, and T. J. Hall, "Photonic Integrated Circuit for Millimeter-Wave Signal Generation by Frequency Multiplication", proceedings of *IEEE Photonics Conference (IPC)*, Reston, VA, USA, Oct 2015.

Abstracts

N. Nabavi**,** S. Abdul-Majid, and T. J. Hall, "Symmetric Dual Polarization Diverse Digital Optical Coherent Receiver", *Photonic North*, Ottawa, Canada, June 2015.

N. Nabavi, T. J. Hall**,** "Demultiplexing by Independent Component Analysis in Coherent Optical Transmission: the Polarization Channel Alignment Problem", *Photonic North*, Ottawa, Canada, June 2015.

Acronyms

ACF	Auto Correlation Function
ADC	Analogue to Digital Converter
AWG	Arbitrary Waveform Generator
AWGN	Additive White Gaussian Noise
B2B	Back-to-Back
BS	Beam Splitter
CD	Chromatic Dispersion
CMA	Constant Modulus Algorithm
CO	Central Office
DFB	Distributed Feedback
DFT	Discrete Fourier Transform
DGD	Differential Group Delay
DQPSK	Differential Quadrature Phase-Shift Keyed
DSP	Digital Signal Processing
DUT	Devices Under Test
DWDM	Denth Wavelength Division Multiplexing
EAM	Electro-Absorption Modulator
EVM	Error-Vector Magnitude
FBG	Fiber-Bragg Grating
FIR	Finite Impulse Response (FIR)
FOH	First-Order Harmonics
ICA	Independent Component Analysis
IDFM	Inverse Discrete Fourier Transform
IM-DD	Intensity-Modulation Direct Detection
IQ	In-phase and Quadrature
IQM	In-phase and Quadrature Modulator
ISI	Inter-Symbol-Interference
LO	Local Oscillator
MMI	Multi-Mode Interference coupler
MMW	Millimeter-Wave
MPIC	Microwave Photonic Integrated Circuit
MRC	Maximal Ratio Combining
MZI	Mach–Zehnder interferometer
NRZ	Non-Return-to-Zero
OCR	Optical Coherent Receiver
OFDM	Orthogonal Frequency Division Multiplexing
OMA	Optical Modulation Analyzer
QAM	Quadrature Amplitude Modulation
ONU	Optical Network Units
OSNR	Optical Signal-to-Noise Ratio
PBS	Polarization Beam Splitter
PC	Polarization Controller
PDG	Polarization Dependent Gain
PDL	Polarization Dependent Loss
PIC	Photonic Integrated Circuit
PMD	Polarization Mode Dispersion
PON	Passive Optical Networks
PRBS	Pseudo Random Binary Signal

PSP	Principle States of Polarizations
QAM	Quadrature Amplitude Modulation
QPSK	Quadrature Phase-Shift Keying
RBS	Polarization Beam Splitter
RF	Radio Frequency
RIN	Relative Intensity Noise
RU	Remote Unit
RoF	Radio-over-Fiber
SDE	Stochastic Differential Equation
SER	Symbol-Error-Ratio
SMF	Single-Mode Fiber
SNR	Signal-to-Noise Ratio
SOP	State Of Polarization
SSB	Single-Sideband
SSMF	Standard Single-Mode Fiber
TE	Transverse Electrical
TM	Transverse Magnetic
TOH	Third-Order Harmonic

Table of Contents

List of Figures

Fig.4.9. Architecture of the OFDM system used to further assess the performance of the proposed MPIC in the RoF system. IFFT: inverse fast Fourier transform; DAC: digital to analog converter; ADC: analog to digital converter; IQM: IQ-modulator; FFT: fast Fourier transform.

Fig.4.10. Simulated EVM for the RoF system versus wireless channel SNR for OFDM signal transmission using 5 km single-mode fiber. Solid line denotes a fit to a logarithmic function of the EVM.

Fig.5.1. Schematic diagram of a polarization diverse coherent receiver. Polarization diversity refers to the input signal. TE (horizontal) and TM (vertical) polarization components are illustrated in green and blue, respectively [34].

Fig.5.2. (a) Chord length corresponding to the arc length, (b) two orthogonal non-intersecting geodesics σ_I and σ_{II} on the manifold, (c) tangent vectors orthogonal to the geodesic I or II.

Fig.5.3. Evolution of simulated states of polarization (SOP) on the Poincaré sphere for (a) 100, (b) 1000, (c) 10000, and (d) 100000 samples.

Fig.5.4. Signal power of (a) channel 1 and (b) channel 2 before diversity combining. Combined signal power after applying ICA algorithm with and without proposed projection method are shown in gray and red respectively in (c) and (d).

Fig.5.5. Channel alignment using ICA method before and after applying the proposed projection algorithm are shown in red and blue respectively.

Fig.5.6. Constellation of the demodulated signal using ICA algorithm with proposed projection method for (a) channel 1 and (b) channel 2 for SNR of 14.77 dB.

Fig.5.7. Experimental setup for testing the tracking channel alignment algorithm. (DFB – distributed feedback laser, AWG – arbitrary waveform generator, A– amplifier, IQM – in-phase quadrature modulator, PBS – polarization beam splitter, PC– polarization controller, SMF– Single Mode Fiber, LO – local oscillator, OMA– optical modulation analyzer, DSP – digital signal processing).

Fig.5.8. Principle of signal flow of the N4391A.

Fig.5.9. Constellation of the demodulated signal using CMA algorithm for (a) polarization X , (b) polarization Y. (e) and (f) are the counterparts of (a) and (b) using CMA-modified algorithm. Constellation of the demodulated signal after carrier phase estimation of polarization de-multiplexed signals using CMA for (c) polarization X and (d) polarization Y. (g) and (h) are the counterparts of (c) and (d) after carrier phase estimation of de-multiplexed signals using modified CMA. Projection method shows improvement in recovery of the constellation diagram of the received signals for both channels. The SNR of channel 1 and channel 2 are measured as 12.6 dB and 10.8 dB respectively.

1 Chapter: Introduction

1.1 Background

Cities have become the major units in the global economy and are responsible for the bulk of innovation. Urban planners envisage a "Digital City" in which ubiquitous broadband wireless and computing access provide all imaginable services to citizens, enterprises, and public services. The vision is of a city that is information rich, economically efficient and effective, clean, healthy, and aesthetically pleasing [1-3]. However, total energy consumption in information and communications networks is rising unsustainably as increased use outstrips energy efficiency gains. This is a concern both in terms of cost, rising pollution local to the city (especially in developing economies) and, climate change via its contribution to global greenhouse gas emissions.

The energy consumption from the expanding use of information and communications technology (ICT) is unsustainable with present drivers. In 2015, ICT consumed around 4% of overall worldwide electricity consumption [4], In a recent study, the share of ICT global electricity usage by 2030 was estimated at 21% in a likely scenario and 51% in the worst-case [5]. Reducing consumption of energy by all ICT devices and systems is a key to capture the full potential of ICT in resource efficiency.

Access network technology is advancing rapidly to provide greater reach, to serve increasing numbers of users, to accommodate increasing bandwidth demands, and to provide the convenience of ‘un-tethered’ wireless connection. The Digital City use case scenario represents the ultimate termination-point of this trend. For RF wireless to accommodate bandwidth hungry applications, a transition to operation in the mm-wavelength region of the RF spectrum is required. At these frequencies, and in cluttered urban environments, the range is reduced. Good coverage then requires the use of pico-cellular networks with a correspondingly increased density of antennas: a 60 GHz wireless access point may be deployed every 10 m in a Digital City. Distributed antenna systems lead to a welcomed reduction in overall energy consumption relative to mono-antenna systems but require a distribution network [6]. It is well established that optical fiber links offer orders of magnitude lower energy consumption compared to other technologies. With fiber optic technology capable of providing the required information capacity larger than both wireless connections and copper cable, advances in technology have enabled more data to be conveyed over long distances [7, 8].

Optical fiber-based networks have intrinsic characteristics that support a move toward networks that reduce energy consumption, waste, and the total cost of ownership (TCO) for a network through longer product lifecycles. Recent innovations in copper chipsets for 10GBase-T applications have brought power consumption for copper networks down to between 1 and 2 watts over shorter distances and about 3.5W at full 100-meter reach capability. Fiber networks, in comparison, may use less than 1W to transmit the 10-GbE signal over 400 meters of fiber. Over time the power savings from a fiber-based network can be meaningful, especially in data center applications where there may be thousands of connections [9]. One arrives consequently at an architecture in which RF signals are optically distributed between the central office and the wireless access points.

In the past, information was encoded most conveniently in the intensity of light only, which may be directly detected. The coherence of the light (i.e. whether or not its phase and polarization state are well-defined) is not a major concern in direct detection systems. Fiber ‘exhaustion’ is a perennial concern of network operators as the installation of new fibers in the ground is extremely costly. The potential of coherent optical communications to stave-off fiber exhaustion in the face of increasing demand for greater bandwidth was understood in the 1980s. Modulation formats that make use of phase and polarization are vastly more spectrally efficient than intensity modulated direct detection but necessarily require coherent detection (i.e. a measurement of the complex amplitude of the field rather than its intensity). The lack of control one had over the phase, in bulk optical systems, and phase and polarization, in fiber-optic systems, presented a huge challenge to the analogue receivers investigated in the 1980's. The research was abandoned following the invention of the Erbium doped fiber amplifier that enabled wavelength division multiplexing (WDM) to stave-off fiber exhaustion for two decades. Coherent communication systems finally became practical around 2010 with the advent of integrated electronic circuits capable of supporting Digital Signal Processing (DSP) at speeds compatible with line rates. Much of the complexity and expense of the functions required in a coherent receiver to compensate for optical channel uncertainties and impairments, including local oscillator frequency offset and drift; and to decode advanced modulation formats could be transferred to DSP algorithms.

The advent of digital coherent transmission constitutes a technological breakthrough in communications. A real-time coherent receiver using DSP, can perform data recovery, carrier phase estimation, polarization de-multiplexing and dispersion compensation for an advanced modulated format system in the electrical domain. Transmission capacity have been improved from the de facto 10 Gbit/s limit of previous systems to recent demonstrations of 1 Tbit/s per-channel transmission. In addition, equalization of waveform distortions can be performed adaptively through DSP. This has led to the elimination of some optical components such as the wavelength dispersion compensation module and variable dispersion compensator used in conventional systems.

1.2 Motivation and objectives

My overarching goal is, via my research to develop radical breakthrough DSP algorithms which will in part enable the vision of a sustainable digital city to promote equality of access to information amongst its citizens and provide them with economic and social benefits via affordable broadband access while containing growth in energy consumption. In my PhD program, I work on DSP algorithm development for an optical fiber network supported distributed millimeter wave wireless antenna system. In a radical departure from the orthodox analogue RF-over-fiber (RoF) paradigm, the “RF-Cité” architecture exploits modern digital coherent optical transmitters and receivers together with spectrally efficient methods of digital RF transport over coherent optical fiber transmission as a solution to high density, high capacity, and energy efficient wireless access. The measurement of the complex amplitude of the optical field yields a linear channel that is a composition of the wireless and optical channels which facilitates impairment correction by DSP. A local oscillator (and in principle power) may be distributed optically using the same distribution network as the signal. Information may be carried in the amplitude, phase and polarization of the optical field. Additionally, the selectivity of a coherent receiver is very well suited to dense multiple access networks with the potential to transform a ‘converged’ wavelength division multiplexed passive optical network (WDM-PON) and RoF architecture to greatly increased levels of multiplexing.

1.3 Thesis scope and outline

To design, analyze and evaluate new architectures for the digital coherent receiver within the RF-Cité, this thesis is comprised of theoretical studies, modeling, and experimentation which aim to provide deeper insights on the performances of coherent receivers and a multi-function photonic integrated circuit for coherent Radio-over-Fiber. The scope of this thesis comprises four important points:

- *Experimental analysis of the optical channel model that accurately describes the single mode fiber transfer matrix*: The numerical modeling of the single mode fiber as an optical coherent transmission medium and experimental measurement is used to determine the polarization drift as a function of time for a fixed length of fiber.

- *Theoretical analysis of symmetric signal and local oscillator polarization diverse coherent optical receiver*: A new symmetric digital coherent receiver has been designed and a novel DSP algorithm proposed to mitigate the impairments of the optical channels.
- *Study of a multi-function photonic integrated circuit for coherent Radio-over-Fiber*: The application of a novel microwave photonic integrated circuit to implement some building blocks within the RF-Cité architecture has been investigated for the first time.
- *Experimental verification of mitigating channel impairments on a single mode fiber:* This mainly includes testing the proposed DSP algorithm to accurately track polarization channel alignment, through accurate polarization de-multiplexing obtained by numerical simulations and experiments.

1.4 Organization of the Thesis

This thesis consists of a collection of scientific articles, each of them presented as a chapter. The remainder of this thesis is organized as follows. Chapter 2 reports a dynamic model of a single mode fiber as a coherent transmission medium which concerns the evolution of the polarization state and its wavelength dependence – which has the potential to be generalized to multimode/space division multiplexed scenarios. The results provided in this chapter are going to be submitted for publications. I developed the theoretical model. I designed the experiment and Peng Liu helped me in building the experimental setup. I generated and interpreted the simulation and experimental results and wrote the manuscript. Dr. Hall contributed to the interpretation of the results, and revised the manuscript.

Chapter 3 introduces an improved coherent optical receiver architecture that compensates for a random drift in the state of polarization (SOP) of both the signal and the local oscillator (LO). The design proposed eliminates the need for a local oscillator laser and the associated power demand of the thermo-electric coolers at the location of the optical coherent receiver. This architecture also relaxes the characterization of the local oscillator laser by facilitating the use of an off-the-shelf laser or, the distribution of the local oscillator from the fiber network or central offices. The results provided in this chapter were published as an article in Optics Express in 2016. Dr. Hall and I developed the theoretical model. I generated and interpreted the simulations and wrote the manuscript. Dr. Hall revised the manuscript.

Aided with DSP, combining microwave and fiber optic-based technologies, chapter 4 offers the possibility of increasing transmission capacity, reducing energy consumption, and the cost of multi-Gb/s wireless access networks by introducing a digital coherent radio-over-fiber (RoF) system comprising a microwave photonic integrated circuit (MPIC) as the main building block. The results provided in this chapter are published as an article in Journal of Lightwave Technology in 2016. I designed the model, generated and interpreted the simulation results and wrote the manuscript. Dr. Maldonado Basilio and Dr. Hall contributed to revision of the manuscript.

Chapter 5 reports a tracking channel alignment algorithm to classify the input polarizations that transmit two independent channels that are mixed randomly as the light is propagating in the optical fiber. The proposed algorithm is beneficial for aerial fiber, multimode systems and where the changes in polarization are fast due to environmental perturbations. The results provided in this chapter are published as an article in Optics Communications in 2017. I developed the theoretical model and implemented the numerical methods used for the theoretical analysis. I designed the experiment and Parya Samadian helped me in building the experimental setup. I interpreted the simulation and experimental results, and wrote the manuscript. Dr. Hall contributed to the development of the theoretical model, the interpretation of the results and, revised the manuscript.Chapter 6 concludes this thesis and presents suggestions for future work.

2 Chapter: Channel modeling in a single mode fiber

2.1 Introduction

In order for the signal processing algorithms to compensate the drawbacks of the fiber optic systems, understanding the realistic model of the optical channel is necessary. Single mode fibers are favorite choice in today optical communication systems as they support a higher bandwidth, reach and transmission speed than multimode fibers and provide lower signal interruption [10, 11]. Therefore, appreciation of a single mode fiber as a substantial optical waveguide is essential.

An ideal dielectric waveguide possesses translation symmetry along its axis [12]. As a consequence, it supports an infinite number of waveguide modes of which a finite number are guided (i.e. bound to the structure). The modes satisfy an orthogonality relation. Additionally, if the waveguide is circularly symmetric (i.e. an optical fiber), the modes occur in orthogonally polarized degenerate pairs [13, 14].

Consequently, an ideal 'single' mode fiber (SMF) supports two orthogonally polarized degenerate guided modes. In the case of weakly guiding waveguides, these modes may be considered to be linearly polarized to a good approximation. The effect of small perturbations of the structure of the ideal fiber on light propagation may be described in terms of the ideal modes by a coupling between their overall amplitudes [15]. Coupling to higher order modes provides a loss mechanism in which energy leaks away by diffusing to higher order modes. However, provided that the perturbation is very slowly varying, significant coupling only occurs between nominally degenerate modes and there is no radiation loss [16]. In a single mode fiber, polarization mode dispersion (PMD) is a random phenomenon that takes place due to birefringence in the fiber that originates from asymmetry caused by an elliptical core, stress, bend, or twist. Polarization mode dispersion stems from the random birefringence which yields different group velocities of the two orthogonal polarizations modes [17]. This polarization effect causes mode coupling and random changes in state-of-polarization (SOP) in a long haul transmission [17, 18]. Since polarization mode dispersion, together with chromatic dispersion (CD), is a major source of pulse distortion and pulse spreading in high speed optical transmission systems, which is also a cumulative effect as a function of the length of the fiber [19-21], it has been studied in detail theoretically and experimentally. Various techniques have been proposed to overcome the PMD barrier, such as the new generation of coherent optical receivers based on digital signal processing (DSP) [22-25] and the deployment of orthogonal frequency-division multiplexing (OFDM) in optical communication systems [26-32]. Nevertheless, this phenomenon still needs further investigations in order to allow an improvement of the transmission capacity, speed, and performance level of a fiber optic communication system [17]. The effective compensation of the dynamic channel impairments such as PMD and CD, can be achieved with finite impulse response (FIR) filters [33]. Hence, a MIMO equalizer which compensates the dynamic impairments of the channel using four filters that have the inverse Jones matrix of the dynamic channel can be used [34].

Due to the dynamic nature of PMD, an adaptive equalization of this impairment using MIMO coherent receivers is required. This has been achieved by utilization of constant modulus algorithm (CMA), which works blindly without any training data to be required [35]. The use of CMA [36] is popular, because of its simplicity, applicability to different modulation formats and immunity to phase noise [37,38]. However, the choice of initial tap values is a major determinant of CMA convergence [39-41]. The CMA with high-order FIR filters can resolve the polarization-mode-dispersion (PMD) effectively, but has the singularity problem which is caused by polarization-dependent loss (PDL) [42]. However, when the amount of PDL is small enough to be neglected, CMA always achieves desired results [43]. On the other hand, independent component analysis (ICA) method can be used to compensate PMD and PDL with a 2×2 matrix of filters, and it can be combined with nonlinearity compensation when fiber nonlinearity becomes prominent [44].

In a single mode fiber, assuming that there is no PDL, the channel matrix is a unitary transformation that is continuous with propagation distance and optical frequency [36]. The longitudinal dependence of the birefringence motivates a stochastic evolution of the PMD vector along the fiber length [19, 45]. The stochastic behavior of SOP with wavelength in the PMD affected fiber has been studied in [46] concluding that the SOP variations in the buried fibers stems from random mode coupling and the birefringence distribution. However, the mathematical derivation of birefringence has not been provided. Although, the autocorrelation function (ACF), which presents information on autocorrelation bandwidth of the fiber-optic channel has been extensively studied but the stochastic derivations only describes ACF of the PMD vector [47-53]. While the prior works are all concerned about polarization mode dispersion and differential group delay in the optical fiber, the numerical analyses and experimental observations in this chapter, have a different objective than the PMD focused studies. This chapter concerns the evolution of the polarization state and its wavelength dependence – The decorrelation of the relative polarization state of two carriers offset in frequency as required for remote heterodyning.

The rest of the chapter is organized as follows. The theory behind the evolution of polarization of light in a single mode fiber is described in Section 2.2. The Stokes vector representation of polarization of light and the diffusion of state of polarizations over the whole Poincaré sphere is discussed in section 2.3. In section 2.4, through recasting the polarization dispersion equations, it is realized that the Poole's equation [45] is the Lax pair equation in terms of Lie Groups and algebras. In section 2.5, the stochastic differential equation is derived which solves the problem of evolution of the state of polarization with distance. The fluctuations in time of the state-of-polarization is explored in section 2.6 where the experimental observations contribute further insight through studying the time correlation structure of the state of polarization by calculating the cross-correlation and cumulative probability functions of it's components. Furthermore, it has been shown that the diffusion of state of polarizations over the whole Poincaré sphere predicted for evolution in space is not seen in the fluctuations in time. Finally, the chapter closes with the drawing of important conclusions in Section 2.7.

2.2 Evolution of polarization of light in a single mode fiber

Since single mode fiber supports two orthogonal polarization modes, the electrical field of the signal can be represented using a Jones vector [17,54]. The polarization of light guided by a single mode optical fiber evolves along the axis of fiber according to:

$$\frac{\partial \boldsymbol{a}}{\partial z} = i\boldsymbol{H}\boldsymbol{a}, \qquad \textit{Equation 2.1}$$

where $\boldsymbol{a}=\begin{bmatrix} a_1 \\ a_2 \end{bmatrix}$ is a vector of the overall complex amplitudes of the two ideal guided modes, which in the weakly guiding case may be considered to represent horizontal and vertical linear polarization states [55]. The coupling arises from environmental fluctuations, and coupling coefficients are functions of position and time which can be described statistically. Eq. 2.1 has solution:

$$\boldsymbol{a}(z) = \boldsymbol{U}(z)\boldsymbol{a}(0), \quad \frac{\partial \boldsymbol{U}}{\partial z} = i\boldsymbol{H}\boldsymbol{U}.$$

Since the waveguide is lossless, the total power must be conserved and $\boldsymbol{U}$ must be unitary. A sufficient condition for $\boldsymbol{U}(z)$ to be unitary is that $\boldsymbol{H}$ should be self-adjoint (i.e. $\boldsymbol{H}^\dagger = \boldsymbol{H}$). Substituting $\boldsymbol{H}$ with $\boldsymbol{H}^\dagger$ yields $\frac{\partial}{\partial z}(\boldsymbol{U}^\dagger\boldsymbol{U}) = 0$, and hence $\boldsymbol{U}^\dagger\boldsymbol{U}$ is a constant equal to identity. Therefore, the coupling matrix $\boldsymbol{H}$ can be specified by four real functions:

$$\boldsymbol{H} = \begin{bmatrix} h_0 + h_1 & h_2 - ih_3 \\ h_2 + ih_3 & h_0 - h_1 \end{bmatrix}. \qquad \textit{Equation 2.2}$$

Defining $\widetilde{\boldsymbol{U}} = \exp(-i\varphi)\,\boldsymbol{U}$, where φ refers to an overall phase perturbation accumulated over the fiber and then taking the derivative of $\widetilde{\boldsymbol{U}}$ with respect to z results in:

$$\frac{\partial \widetilde{U}}{\partial z} = i\widetilde{\boldsymbol{H}}\widetilde{\boldsymbol{U}}, \qquad \textit{Equation 2.3}$$

where $\widetilde{\boldsymbol{H}} = \boldsymbol{H} - \frac{\partial \varphi}{\partial z}\boldsymbol{I}$. Setting $\varphi(\mathrm{z}) = \int_0^{\mathrm{z}} h_0 dz = \frac{1}{2}\int_0^{\mathrm{z}} \mathrm{Tr}(\boldsymbol{H})dz$, yields $\mathrm{Tr}(\widetilde{\boldsymbol{H}}) = 0$. Therefore, if the primary goal is to describe the evolution of polarization, the coupling matrix may be taken as traceless.

In a coherent detection scheme, the coherent receiver must be phase diverse to compensate for fluctuations in the overall phase [56]. It follows from $\frac{\partial}{\partial z}\mathrm{Ln}(\det(\boldsymbol{U})) = \mathrm{Tr}\left(\boldsymbol{U}^{-1}\frac{\partial \boldsymbol{U}}{\partial \mathrm{z}}\right) = \mathrm{Tr}\left(\frac{\partial \boldsymbol{U}}{\partial z}\boldsymbol{U}^{-1}\right)$, that one is at liberty to set $\det(\boldsymbol{U}) = 1$ when the state of polarization only of interest, i.e. $\boldsymbol{U}$ may be chosen as a member of the special unitary group in two dimensions SU(2). Every member of SU(2) has the Caley-Klein representation [57]:

$$\boldsymbol{U} = \begin{bmatrix} c & b \\ -b^* & c\,* \end{bmatrix} \quad |c^2| + |b^2| = 1, \qquad \textit{Equation 2.4}$$

that can be parameterized in terms of three Euler angles ξ, μ, and γ:

$$\begin{cases} c = \cos(\xi)\exp[i(\gamma+\mu)] \\ b = \sin(\xi)\exp[i(\gamma-\mu)] \end{cases}. \qquad \textit{Equation 2.5}$$

The overall phase has no effect on the observed polarization state. To show this, we consider a unit intensity source at $z = 0$ that is first linearly polarized in the horizontal direction yielding: $\boldsymbol{a}(z) = \begin{bmatrix} c \\ -b^* \end{bmatrix} = \exp\left[i\left(\mu+\frac{\pi}{2}\right)\right]\begin{bmatrix} \cos(\xi)\exp\left[i\left(\gamma-\frac{\pi}{2}\right)\right] \\ \sin(\xi)\exp\left[-i\left(\gamma-\frac{\pi}{2}\right)\right] \end{bmatrix}$, and then the vertical direction: $\boldsymbol{a}(z) = \begin{bmatrix} c \\ b^* \end{bmatrix} = \exp\left[-i\left(\mu-\frac{\pi}{2}\right)\right]\begin{bmatrix} \cos\left(\xi-\frac{\pi}{2}\right)\exp\left[i\left(\gamma-\frac{\pi}{2}\right)\right] \\ \sin\left(\xi-\frac{\pi}{2}\right)\exp\left[-i\left(\gamma-\frac{\pi}{2}\right)\right] \end{bmatrix}$. It can be seen in either case that $(\mu \pm \frac{\pi}{2})$ is an overall phase and has no effect on the recorded polarization state. In the case of a single polarization source, the angle μ cannot be distinguished from the overall phase in which it may be subsumed.

If the source polarization is modulated, a coherent receiver must be phase diverse on each polarization channel to compensate for fluctuations in the two different overall phases. Conceivably, there may be advantages in tracking separately the overall phase φ and the differential phase 2μ between polarization channels. In terms of polarization only, it is therefore found that only two phases are of significance which is consistent with the definition of the state of polarization as independent of overall magnitude and phase of the Jones vector: $a(z)=\begin{bmatrix} a_1 \\ a_2 \end{bmatrix} = \begin{bmatrix} |a_1|\exp(i\theta_1) \\ |a_2|\exp(i\theta_2) \end{bmatrix} = \begin{bmatrix} cos(\alpha)\exp(i\vartheta) \\ sin(\alpha)\exp[-i\vartheta] \end{bmatrix}$, where,

$$\begin{cases} \vartheta = \frac{1}{2}(\theta_1-\theta_2) \\ \alpha = \tan^{-1}\frac{|a_2|}{|a_1|} \end{cases}. \qquad \textit{Equation 2.6}$$

2.3 Stokes vector representation

The coherency matrix embodies all the information on the second order statistics of the components of the optical signal and it is given by:

$$\boldsymbol{\Psi} = \langle \boldsymbol{a}\boldsymbol{a}^{\dagger} \rangle = \begin{bmatrix} \langle a_1 a_1^* \rangle & \langle a_1 a_2^* \rangle \\ \langle a_2 a_1^* \rangle & \langle a_2 a_2^* \rangle \end{bmatrix}.$$

Equation 2.7

The bracket $\langle\cdot\rangle$ denotes an ensemble average. In the perfectly coherent case, each member of the ensemble is identical and the brackets may be removed. So, $\boldsymbol{\Psi} = \frac{1}{2} s_0 \sigma_0 + \frac{1}{2} \vec{\boldsymbol{s}} \cdot \vec{\boldsymbol{\sigma}}$, where $\boldsymbol{s} = [s_1 \quad s_2 \quad s_3]^{\mathrm{T}}$ and $\boldsymbol{\sigma} = [\boldsymbol{\sigma}_1 \quad \boldsymbol{\sigma}_2 \quad \boldsymbol{\sigma}_3]^{\mathrm{T}}$ are the Stokes vector and Pauli spin vector respectively. The Pauli spin matrices $\boldsymbol{\sigma}_0$, $\boldsymbol{\sigma}_1$, $\boldsymbol{\sigma}_2$, and $\boldsymbol{\sigma}_3$ are defined as [58]:

$$\begin{aligned} \boldsymbol{\sigma}_0 &= \begin{bmatrix} 1 & 0 \\ 0 & 1 \end{bmatrix} \quad \boldsymbol{\sigma}_1 = \begin{bmatrix} 1 & 0 \\ 0 & -1 \end{bmatrix} \\ \boldsymbol{\sigma}_2 &= \begin{bmatrix} 0 & 1 \\ 1 & 0 \end{bmatrix} \quad \boldsymbol{\sigma}_3 = \begin{bmatrix} 0 & -i \\ i & 0 \end{bmatrix}. \end{aligned}$$

Equation 2.8

Note, the commutation relations follows: $[\boldsymbol{\sigma}_1, \boldsymbol{\sigma}_2] = 2i\boldsymbol{\sigma}_3$, $[\boldsymbol{\sigma}_2, \boldsymbol{\sigma}_3] = 2i\boldsymbol{\sigma}_1$, and $[\boldsymbol{\sigma}_3, \boldsymbol{\sigma}_1] = 2i\boldsymbol{\sigma}_2$.

A Hermitian inner product $(\cdot,\cdot)$ and induced norm $[\![\cdot]\!]$ on $\mathbb{C}^{\mathrm{n \times n}}$ are defined by $(\boldsymbol{X}, \boldsymbol{Y}) = \mathrm{Tr}(\boldsymbol{X}\boldsymbol{Y}^{\dagger}) = \sum_{ij} x_{ij} y_{ij}^*$ and $[\![\boldsymbol{X}]\!] = (\boldsymbol{X}, \boldsymbol{X})^{\frac{1}{2}}$, respectively. Noting that $(\boldsymbol{\sigma}_i, \boldsymbol{\sigma}_j) = 2\delta_{ij}$, then $s_i = (\Psi, \sigma_i)$, $s_0 = (\Psi_{11} + \Psi_{22})$, $s_1 = (\Psi_{11} - \Psi_{22})$, $s_2 = (\Psi_{12} + \Psi_{21})$ and $s_3 = i(\Psi_{12} - \Psi_{21})$, where (s_0, s_1, s_2, s_3) are the four Stokes parameters. In the completely polarized case: $s_0 = |a_1|^2 + |a_2|^2$, $s_1 = |a_1|^2 - |a_2|^2$, $s_2 = 2|a_1||a_2|\cos(2\vartheta)$ and $s_3 = 2|a_1||a_2|\sin(2\vartheta)$. Since, $|\vec{\boldsymbol{s}}| = \sqrt{(|a_1|^2 - |a_2|^2)^2 + 4|a_1|^2|a_2|^2} = s_0$, complete information on the state of polarization is therefore provided by the unit Stokes vector, $\hat{\boldsymbol{s}} = \frac{1}{s_0}\vec{\boldsymbol{s}}$. For ease of exposition, perfect coherence and unit total intensity can be assumed. The Jones and Stokes vectors are then of unit length and the tildes may be omitted. The Stokes vector evolves with propagation as $\boldsymbol{\Psi}(z) = \boldsymbol{a}(z)\boldsymbol{a}^{\dagger}(z)$. Taking the derivative of $\boldsymbol{\Psi}(z)$ with respect to z results in $\frac{\partial \boldsymbol{\Psi}}{\partial z} = i[\boldsymbol{H}, \boldsymbol{\Psi}]$, where $\boldsymbol{H} = \vec{\boldsymbol{h}} \cdot \vec{\boldsymbol{\sigma}}$. It follows that:

$$[\boldsymbol{H}, \boldsymbol{\Psi}] = i(\vec{\boldsymbol{h}} \times \vec{\boldsymbol{s}}) \cdot \vec{\boldsymbol{\sigma}},$$

Equation 2.9

where $\frac{\partial \vec{s}}{\partial z} = -\vec{\boldsymbol{h}} \times \vec{\boldsymbol{s}}$, $\frac{\partial s_0}{\partial z} = 0$ and $\frac{\partial \vec{s}}{\partial z} \cdot \vec{\boldsymbol{h}} = 0$. Therefore, the tangent vector to the trajectory $\vec{\boldsymbol{s}}(z)$ is perpendicular to $\vec{\boldsymbol{h}}(z)$ and the length of $\vec{\boldsymbol{s}}$ is a constant of the motion. Hence, the Stokes vector stays on the Poincaré sphere and rotates anti-clockwise as viewed from the origin about the birefringence vector $\vec{\boldsymbol{h}}$ as z advances.

2.4 Chromatic dispersion of polarization

Chromatic dispersion of the polarization is manifest as a change in the state of polarization with frequency. Assuming that there is no polarization dependent loss (i.e. the magnitude of the Jones vector is invariant to the state of polarization), the transmission matrix remains unitary:

$$\boldsymbol{U}(\omega, z)\boldsymbol{U}^{\dagger}(\omega, z) = \boldsymbol{I}. \qquad \text{Equation 2.10}$$

Differentiating Eq. 2.10 with respect to ω yields $\left(\frac{\partial}{\partial \omega}\boldsymbol{U}\right)\boldsymbol{U}^{\dagger} = \boldsymbol{iG}$, where $\boldsymbol{G}$ is a Hermitian matrix. If, $\det(\boldsymbol{U}(\omega, z)) = 1$, then $\frac{\partial}{\partial \omega}\ln(\det(\boldsymbol{U})) = \mathrm{Tr}\left(\frac{\partial \boldsymbol{U}}{\partial \omega}\boldsymbol{U}^{-1}\right)$, which implies $\mathrm{Tr}(\boldsymbol{G}) = \boldsymbol{0}$ and therefore:

$$\frac{\partial \boldsymbol{U}}{\partial \omega} = i\boldsymbol{G}\boldsymbol{U}. \qquad \text{Equation 2.11}$$

The same argument repeated with ω substituted by z yields:

$$\frac{\partial \boldsymbol{U}}{\partial z} = i\boldsymbol{H}\boldsymbol{U}, \qquad \text{Equation 2.12}$$

where $\boldsymbol{H}$ is a traceless Hermitian matrix. Taking the second derivative of Eq. 2.11 with respect to z, and of Eq. 2.12 with respect to ω while taking into consideration that the mixed second partial derivatives must agree for continuous $\boldsymbol{U}$ follows:

$$\frac{\partial \boldsymbol{H}}{\partial \omega} - \frac{\partial \boldsymbol{G}}{\partial z} + i[\boldsymbol{H}, \boldsymbol{G}] = 0. \qquad \text{Equation 2.13}$$

In the context of PMD studies Eq. (2.13) is known as Poole's equation [45,59]. It most commonly arises in studies of integrable non-linear equations for which $\boldsymbol{H}$ and $\boldsymbol{G}$ are known as a 'Lax pair' and are considered to be elements of a Lie Algebra (a linear vector space that is also an algebra with the Lie bracket $[.,.]$ as its product) [60]. The focus then is on the nonlinear partial differential equations that are generated by a particular choice of Lie Algebra. The solution of the nonlinear equation then has a representation in terms of the Lie Group associated with the Lie Algebra: $\boldsymbol{H} = \frac{1}{i}\frac{\partial \boldsymbol{U}}{\partial z}\boldsymbol{U}^{\dagger}, \quad \boldsymbol{G} = \frac{1}{i}\frac{\partial \boldsymbol{U}}{\partial \omega}\boldsymbol{U}^{\dagger}$.

In the present case of single mode fiber, the Group is SU(2) and the algebra is su(2). The Pauli spin matrices form a basis for su(2) which enables the equation to be recast in terms of real three dimensional vectors $\boldsymbol{h} = [h_1 \quad h_2 \quad h_3]^{\mathrm{T}}$ and $\boldsymbol{g} = [g_1 \quad g_2 \quad g_3]^{\mathrm{T}}$:

$$\frac{\partial \boldsymbol{h}}{\partial \omega} - \frac{\partial \boldsymbol{g}}{\partial z} = 2\boldsymbol{h} \times \boldsymbol{g}$$ *Equation 2.14*

Also, note that a derivation of a coupled mode equations for a perturbed waveguide leads to the model:

$$\boldsymbol{H} = \omega \overline{\boldsymbol{H}} \quad \equiv \quad \boldsymbol{h} = \omega \overline{\boldsymbol{h}},$$ *Equation 2.15*

where $\overline{\boldsymbol{H}}, \ (\overline{\boldsymbol{h}})$ are expected to only have weak dependence on ω. The Poole's equation then is a means of deducing certain properties of $\boldsymbol{G}$ from assumed properties of $\boldsymbol{H}$. $\boldsymbol{H}$ then enters as the coefficient of a variable coefficient linear equation for $\boldsymbol{G}$ $(\boldsymbol{g})$:

$$\frac{\partial \boldsymbol{G}}{\partial z} - i[\boldsymbol{H}, \boldsymbol{G}] = \frac{\partial \boldsymbol{H}}{\partial \omega}$$
$$\equiv$$
$$\frac{\partial \boldsymbol{g}}{\partial z} + 2\boldsymbol{h} \times \boldsymbol{g} = \frac{\partial \boldsymbol{h}}{\partial \omega}$$

Compared with Eq. (6.15) in [17] $\boldsymbol{g}$ is identified as the 'PMD vector' $\vec{\boldsymbol{\tau}}$ and $\boldsymbol{h}$ as the 'birefringence vector' $\vec{\boldsymbol{\beta}}$.

We assume that $\boldsymbol{h}$ is adequately characterized as a three dimensional vector with components that are independent identically distributed Gaussian processes which is experimentally verified in section 2.6.

2.5 Formulating the problem as a stochastic differential equation

The basic tool for describing random phenomena is the probability theory as we can determine the distributions of all finite dimensional random vectors produced by the random process [61]. In the present case, since $\boldsymbol{h}$ not only acts as a Langevin source but also provides some coefficients of differential equation, the equation must be interpreted as a Stochastic Differential Equation (SDE). Formulating the problem as a SDE helps to obtain predictions for stochastic structure of $\boldsymbol{G}\,(\boldsymbol{g})$ such as autocorrelation function and probability density distribution.

Substituting Eq. 2.15 in Eq. 2.14 yields: $\frac{dg}{dz} = \overline{\boldsymbol{h}} + 2\omega\boldsymbol{g} \times \overline{\boldsymbol{h}}$. Defining $\overline{\boldsymbol{h}} = v\frac{dw}{dz}$, then Eq. 2.14 can be rewritten in the form of:

$$\mathrm{d}\boldsymbol{g} = v(I + 2\omega\boldsymbol{g}\,\times)\mathrm{d}w \qquad \textit{Equation 2.16}$$

Comparing with the canonical form:

$$d\boldsymbol{X}_t = \boldsymbol{\mu}(\boldsymbol{X}_t, t)dt + \boldsymbol{\sigma}(\boldsymbol{X}_t, t) \circ d\boldsymbol{W}_t$$

$$\boldsymbol{X}_t \equiv \boldsymbol{g}$$

$$t \equiv \mathrm{z}$$

$$\boldsymbol{\mu}(\boldsymbol{X}_t, t) \equiv \boldsymbol{0}$$

$$\boldsymbol{\sigma}(\boldsymbol{X}_t, t) \equiv v(\boldsymbol{I} + 2\omega\boldsymbol{g}\,\times)d\boldsymbol{w}$$

$$\mathrm{d}\boldsymbol{W}_t \equiv \mathrm{d}\boldsymbol{w}$$

Hence:

$$\mathrm{d}\boldsymbol{g} \equiv \boldsymbol{\sigma}(\boldsymbol{g}) \circ \mathrm{d}\boldsymbol{w}$$

$$\boldsymbol{\sigma}(\boldsymbol{g}) \equiv v(\boldsymbol{I} + 2\omega \boldsymbol{g} \times) = v \begin{bmatrix} 1 & -2\omega g_3 & 2\omega g_2 \\ 2\omega g_3 & 1 & -2\omega g_1 \\ -2\omega g_2 & 2\omega g_1 & 1 \end{bmatrix}$$

In the Stratonovich interpretation [62] the corresponding Fokker-Planck equation [63] is:

$\frac{\partial f}{\partial z} = \frac{1}{2} \sum_{k=1,3} \sum_{i=1,3} \frac{\partial}{\partial g_i} \left\{ \sigma_{ik} \sum_{j=1,3} \frac{\partial}{\partial g_i} \left[\sigma_{jk} f \right] \right\}$ *Equation 2.17*

Note:

$$\frac{\partial}{\partial g_i}[\sigma_{ik}\varphi] = \frac{\partial}{\partial g_i}[(\boldsymbol{\sigma e}_k, \boldsymbol{e}_i)\varphi] = \left(\frac{\partial \boldsymbol{\sigma}}{\partial g_i}\boldsymbol{e}_k, \boldsymbol{e}_i\right)\varphi + (\boldsymbol{\sigma e}_k, \boldsymbol{e}_i)\frac{\partial \varphi}{\partial g_i} = 2v\omega(\boldsymbol{e}_i \times \boldsymbol{e}_k, \boldsymbol{e}_i)\varphi + \sigma_{ik}\frac{\partial \varphi}{\partial g_i}$$

$$\frac{\partial}{\partial g_i}[\sigma_{ik}\varphi] = \sigma_{ik}\frac{\partial \varphi}{\partial g_i}$$

Hence, Eq. 2.17 may be rewritten as:

$$\frac{\partial f}{\partial z} = \frac{1}{2} \sum_{k=1,3} \sum_{i=1,3} \sum_{j=1,3} \sigma_{ik}\sigma_{jk} \frac{\partial^2 f}{\partial g_i \partial g_i}$$

it can be recast as:

$$\frac{\partial f}{\partial z} = \frac{1}{2} \sum_{i=1,3} \sum_{j=1,3} D_{ij} \frac{\partial^2 f}{\partial g_i \partial g_i}$$

$$D_{ij} = \sum_{j=1,3} \boldsymbol{\sigma}_{ik} \boldsymbol{\sigma}_{jk}$$

Equivalently:

$$\frac{\partial f}{\partial z} = \frac{1}{2} Tr(\boldsymbol{D}\boldsymbol{\mathcal{H}}(f))$$

$$\mathcal{H}_{ij}(f) = \frac{\partial^2 f}{\partial g_i \partial g_i}$$

Where $\mathrm{Tr}(\boldsymbol{AB}^T) = \sum_{ij} \boldsymbol{A}_{ij}\boldsymbol{B}_{ij}$, and the fact that the Hessian [64] $\boldsymbol{\mathcal{H}}$ is symmetric has been used.

Note: $\boldsymbol{D} = \boldsymbol{\sigma\sigma}^T$, and: $\boldsymbol{\sigma} = v(\boldsymbol{I} + 2\omega \boldsymbol{g} \times)$, $\boldsymbol{\sigma^T} = v(\boldsymbol{I} - 2\omega \boldsymbol{g} \times)$.

Hence:

$$\boldsymbol{D} = v^2(\boldsymbol{I} - 4\omega^2 \boldsymbol{g} \times \boldsymbol{g} \times)$$

In the special case $\omega = 0$ the equation reverts to the standard Wiener process in three dimensions and the Fokker-Planck equation simplifies to:

$$\frac{\partial f}{\partial z} = \frac{1}{2}v^2 \mathrm{Tr}(\boldsymbol{\mathcal{H}}(f)) = \frac{1}{2}v^2\left(\frac{\partial^2 f}{\partial g_1^2} + \frac{\partial^2 f}{\partial g_2^2} + \frac{\partial^2 f}{\partial g_3^2}\right)$$

And the solution is:

$$f(\boldsymbol{g}) = \left[\frac{1}{\sqrt{2\pi}\sqrt{v^2 z}}\right]^3 \exp\left[-\frac{1}{2}\frac{(\boldsymbol{g}\cdot\boldsymbol{g})}{v^2 z}\right]$$

This is confirmed by:

$$\frac{1}{f}\frac{\partial^2 f}{\partial g_i \partial g_i} = \frac{\partial \mathrm{Ln} f}{\partial g_i}\frac{\partial \mathrm{Ln} f}{\partial g_i} + \frac{\partial \mathrm{Ln} f}{\partial g_i \partial g_i}$$ *Equation 2.18*

Hence:

$$\frac{1}{f}\boldsymbol{\mathcal{H}}(f) = \frac{1}{v^4 z^2}(\cdot, \boldsymbol{g})\boldsymbol{g} + \frac{1}{v^2 z}\boldsymbol{I}$$

$$v^2 \frac{1}{2} Tr\left\{\frac{1}{f}\boldsymbol{\mathcal{H}}(f)\right\} = \frac{1}{2}\frac{1}{v^2 z^2}(\boldsymbol{g}, \boldsymbol{g}) - \frac{3}{2}\frac{1}{z}$$

$$\frac{1}{f}\frac{\partial f}{\partial z} = -\frac{3}{2}\frac{1}{z} + \frac{1}{2}\frac{1}{v^2 z^2}(\boldsymbol{g}, \boldsymbol{g}).$$

Note the rotational invariance that follows from:

$$(\boldsymbol{Rg}, \boldsymbol{Rg}) = (\boldsymbol{R}^T\boldsymbol{Rg}, \boldsymbol{g}) = (\boldsymbol{g}, \boldsymbol{g}).$$

This rotational invariance is to be expected even in the general case given that there is nothing physical to distinguish one component of $\boldsymbol{h}$ from any other and hence the same applies to $\boldsymbol{g}$.

In the general case:

$$\frac{\partial f}{\partial z} = \frac{1}{2}\mathrm{Tr}\big(\boldsymbol{D}\boldsymbol{\mathcal{H}}(f)\big) - 4v^2\omega^2 \sum_{j=1,3} g_j \frac{\partial f}{\partial g_j}$$
$$\boldsymbol{D} = v^2\boldsymbol{I} - 4v^2\omega^2 \boldsymbol{g} \times \boldsymbol{g} \times$$

Note:

$$\boldsymbol{g} \times \boldsymbol{g} \times (\cdot) = (\cdot, \boldsymbol{g})\boldsymbol{g} - (\boldsymbol{g}, \boldsymbol{g})\boldsymbol{I}$$

$$\boldsymbol{D} = [v^2 + 4\omega^2(\boldsymbol{g}, \boldsymbol{g})]\boldsymbol{I} - 4v^2\omega^2(\cdot, \boldsymbol{g})\boldsymbol{g}$$

Defining:

$$f = \exp[\mathcal{P}(z;\xi)]$$
$$\xi = (\boldsymbol{g},\boldsymbol{g})$$

and substituting in Eq. 2.18:

$$\frac{1}{f}\frac{\partial^2 f}{\partial g_i \partial g_j} = \frac{\partial lnf}{\partial g_i}\frac{\partial lnf}{\partial g_j} + \frac{\partial^2 lnf}{\partial g_i \partial g_j} = \left(\mathcal{P}_{\xi\xi} + \mathcal{P}_{\xi}^2\right)\frac{\partial \xi}{\partial g_i}\frac{\partial \xi}{\partial g_j} + \mathcal{P}_{\xi}\frac{\partial^2 \xi}{\partial g_i \partial g_j}$$
$$\Rightarrow$$
$$\frac{1}{f}\boldsymbol{\mathcal{H}}(f) = 4\left(\mathcal{P}_{\xi\xi} + \mathcal{P}_{\xi}^2\right)(\cdot,\boldsymbol{g})\boldsymbol{g} + 2\mathcal{P}_{\xi}\boldsymbol{I}$$
$$\boldsymbol{D}\frac{1}{f}\boldsymbol{\mathcal{H}}(f) = 4v^2\left(\mathcal{P}_{\xi\xi} + \mathcal{P}_{\xi}^2 - 2\omega^2\mathcal{P}_{\xi}\right)(\cdot,\boldsymbol{g})\boldsymbol{g} + 2v^2\mathcal{P}_{\xi}\left(1 + 4\omega^2(\boldsymbol{g},\boldsymbol{g})\right)\boldsymbol{I}$$
$$\frac{1}{2}\frac{1}{f}Tr\left(\boldsymbol{D}\boldsymbol{\mathcal{H}}(f)\right) = 2v^2\left(\mathcal{P}_{\xi\xi} + \mathcal{P}_{\xi}^2 - 2\omega^2\mathcal{P}_{\xi}\right)\xi + 3v^2\mathcal{P}_{\xi}(1 + 4\omega^2\xi)$$
$$\frac{1}{f}\frac{\partial f}{\partial z} = \mathcal{P}_z$$

Therefore:

$$\mathcal{P}_z(\xi) = 2v^2\left(\mathcal{P}_{\xi\xi} + \mathcal{P}_{\xi}^2 - 2\omega^2\mathcal{P}_{\xi}\right)\xi + 3v^2\mathcal{P}_{\xi}(1 + 4\omega^2\xi) - 8\omega^2 v^2\xi\mathcal{P}_{\xi} = 3v^2\mathcal{P}_{\xi} + 2v^2\left(\mathcal{P}_{\xi\xi} + \mathcal{P}_{\xi}^2\right)\xi$$

Let:

$$\mathcal{P}(\xi) = c_0 + c_1\,\xi$$

Hence:

$$\mathcal{P}_{\xi} = c_1$$
$$\mathcal{P}_{\xi}^2 = c_1^2$$
$$\mathcal{P}_{\xi\xi} = 0$$

Therefore:

$$\frac{dc_0}{dz} + \frac{dc_1}{dz}\xi = 3v^2 c_1 + 2v^2(c_1^2)\xi$$
$$\Rightarrow$$
$$\frac{dc_0}{dz} = 3v^2 c_1$$
$$\frac{dc_1}{dz} = 2v^2 c_1^2$$

The solution for c_0 and c_1 are:

$$c_1(z) = \frac{1}{-2v^2 z - 2a}$$
$$c_0(z) = Log(b) - \frac{3}{2}Log(2v^2 z + 2a)$$

Where *a* and *b* are constant of integration. So $f(\boldsymbol{g})$ is:

$$f(\boldsymbol{g}) = \frac{b}{(2v^2 z + 2a)^{\frac{3}{2}}}exp\left(-\frac{(\boldsymbol{g}.\boldsymbol{g})}{2(v^2 z + a)}\right)$$
$$(\boldsymbol{g}.\boldsymbol{g}) = g_1^2 + g_2^2 + g_3^2$$

Setting $b = \pi^{-\frac{3}{2}}$ and defining σ_0 as the standard deviation for $z = 0$, the standard deviation σ of the normal distribution is equal to: $\sigma = \sqrt{(\upsilon^2 z + a)}$ and the formula for $f(\boldsymbol{g})$ is a normal distribution for three dimensions:

$$f(\boldsymbol{g}) = \frac{1}{(2\pi)^{\frac{3}{2}}\sigma^3} exp\left(-\frac{g_1^2+g_2^2+g_3^2}{2\sigma^2}\right) \qquad \textit{Equation 2.19}$$

According to Eq. 2.19, as $z \rightarrow \infty$ the standard deviation of the probability distribution tends to the square root of the length:

$$\lim_{z\rightarrow\infty} \sigma = \nu\sqrt{z} \qquad \textit{Equation 2.20}$$

2.6 Fluctuations of SOP: Experimental and numerical results

To further assess the channel modeling, a series of experiments were performed using Agilent technologies polarimeter. The instruments used were Agilent N7788B optical component analyzer and Agilent N7714A multiple tunable laser source. The wavelength of the laser and the power of the laser were set to 1550 nm and 10 mW, respectively. The experimental setup is depicted in Fig. 2.1. The experiment was triggered having the light linearly polarized in the horizontal direction at *z*=0 and sampling rate of 0.05 kHz with the 15 seconds logging intervals and the Stokes parameters were recorded for *N* number of samples. The devices under test (DUT) were a 20 km standard Corning SMF28 fiber spool and 5 km outdoor SMF28 fiber.

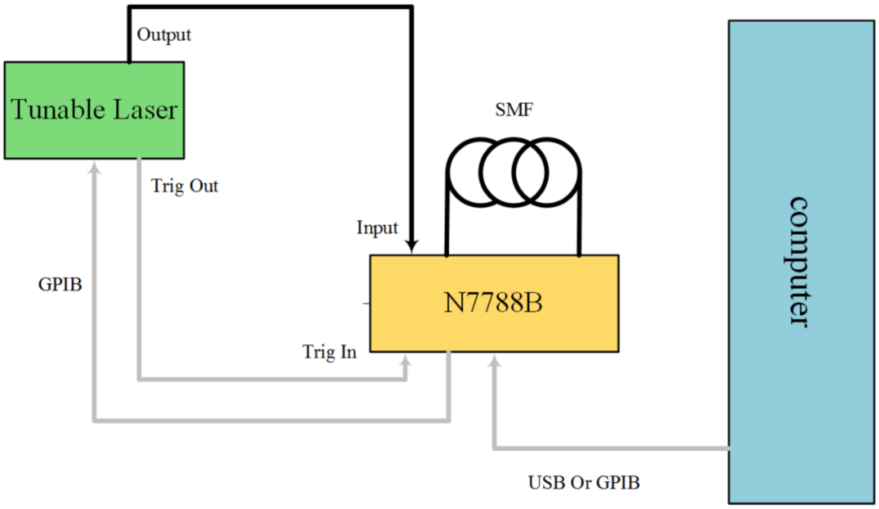

Fig. 2.1. Schematic diagram of the setup for swept-wavelength SOP measurements using the N7788B. The gray and black arrows refer to electrical and optical connections respectively.

A 24 hour experiment of recording SOP for a 5 km outdoor fiber is illustrated in Fig. 2.2(a). Recorded states of polarization are located around the South Pole of the sphere. Note, the start and end SOPs are not located at the same points, which suggest the drift of polarization is not periodic for a 24 hours span. Only SOPs for every 4 hours are visualized to illustrate its trajectory over the 24 hours recording time. Conducting the test with the 20 km long indoor fiber with duration of 38 hours suggests the drift is not having the same statistics as in previous one (outdoor) as shown in Fig. 2.2(b).

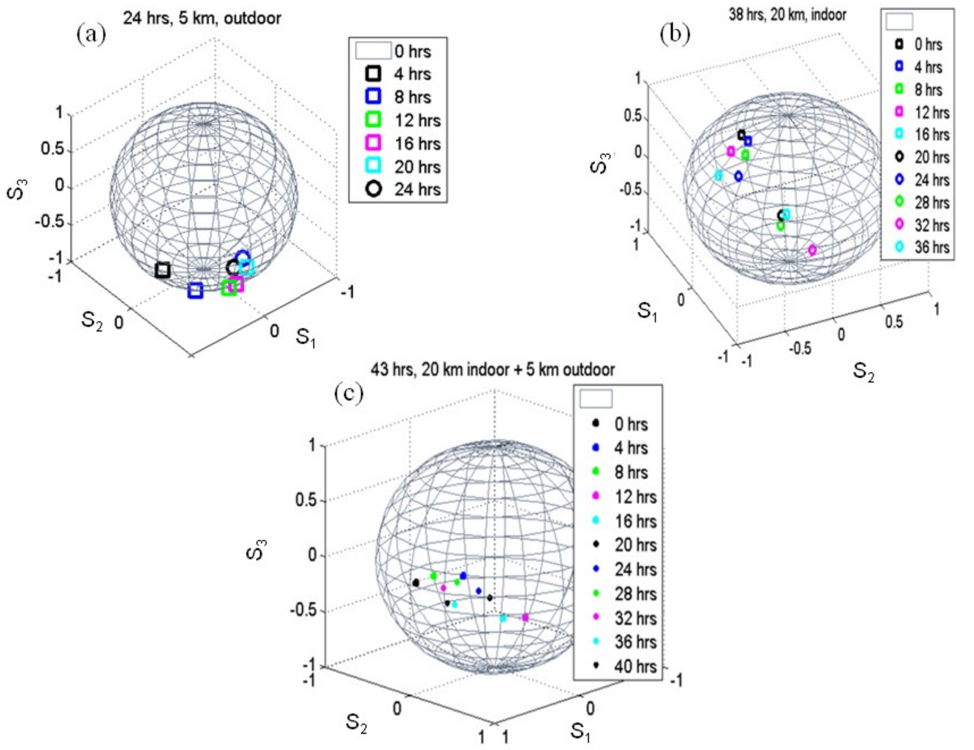

Fig. 2.2. (a) 24hr, 5km, outdoor recorded states of polarization (SOP) are located around the South Pole of the sphere. SOPs for every 4 hrs are visualized, (b) The SOP for a 38hr, 20 km long indoor fiber. In a relatively short observation time of 4 hr, the polarization drift is more localized relative to the outdoor measurement, which indicates the indoor fiber provides relatively more stable SOP in this particular experiment, (c) The results of this measurement are a combination of the indoor (20 km) and outdoor (5 km) SOPs.

The starting point for the SOP, and after 24 hours appears to be ‘closer’ relative to the previous test which suggest these SOPs may follow a quasi periodic trajectory with a 24 hours periodicity. In a relatively short observation time (e.g. 4 hour), the polarization drift is more localized relative to the outdoor measurement, which indicates the indoor fiber provides relatively more stable SOP in this particular experiment. Figure 2.3(c) shows the results of the third measurement which obtained by concatenation of the indoor (20 km) and outdoor (5 km) fibers. It seems the ‘local’ statistics are dominated by the outdoor fiber span, but the statistics for a long observation time are by the indoor fiber span. The evolution of states of polarization with time is also assessed by numerical simulations as depicted in Fig. (2.3). Independent randomly-drifted states of polarization are modeled as a Brownian motion on the SU(2) manifold which is isomorphic to the three-dimensional surface of the sphere in four dimensions S^3. The motion on S^3 is locally approximated by a random walk on its tangent plane $\mathbb{R}^3$. The drifting SOP is visualized as a motion on the Poincaré sphere.

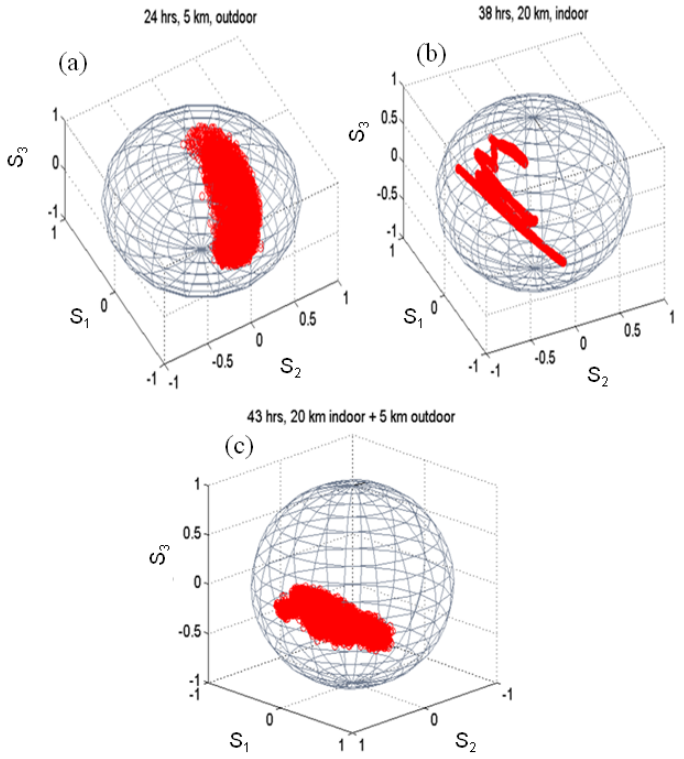

Fig. 2.3. Continuous trajectories of SOP for (a) 24 hrs using 5 km of outdoor fiber, (b) 38 hrs using 20 km indoor fiber, and (c) 43 hrs, 20 km indoor and 5 km outdoor fiber.

Essentially, the Brownian motion has one adjustable parameter which is the variance of the 'step size' the trajectory receives each sample time. The variance has been reduced so that for the same number of samples the motion remains localized to a region – more samples then show increased diffusion over the sphere. The motion is that of a single 'particle' – the SOP that is being buffeted about along random white Gaussian tangent vectors and then projected back onto the surface of the sphere. The SOP is calculated as a Jones vector with three independent angular co-ordinates. The actual SOP is represented as the outer product of this Jones vector and this ‘coherency matrix’ is stored as the trace. The coherency matrix may be represented as its co-ordinates – Stokes parameters – when represented by a basis consisting of the Pauli spin matrices.

Similar to our observations, a relatively slow polarization drift is observed, with small changes of the polarization from sample to sample. All the data is localized to a small region of the Poincaré sphere which suggests much longer observation periods and more likely much longer fiber lengths are required to see the SOP diffuse over the whole surface of the sphere. The SOP changes, although small, slowly cover the whole Poincaré sphere. The fiber spool experimental data resembles samples of some random distribution. The experimental data confirms that the SOP in the two cases is more stable than anticipated and the buried fiber significantly more stable. The frequency (tunable laser) dependent evolution of the SOP and its statistics will yield further information. The obtained results suggest that state of polarization of the outdoor link (qualitatively) most closely follows a Brownian motion in time on the Poincaré sphere, albeit it does not manage to cover the whole sphere in 24 hours in current conditions.

2.6.1 Probability distribution of birefringence vector

The state of polarization of two light waves close in frequency slowly de-correlates with long distance transmissions [52]. However, it has been proved that for two eigenmodes the first order polarization dispersion is zero and they are called principal states of polarizations [18]. These two orthogonal polarization states are frequency independent to first order. Considering each PSP to have a delay in the time domain, the difference between their group delays is called differential group delay. The data recorded can serve to help development of data analysis methods, as the theory indicates no information about the time behavior of long term cross-correlations. This is because of the fact that theory uses ensemble averages whereas measurement necessarily uses time averages. An assumption of ergodicity only implies that space averages would equal ensemble averages. But the length of the fiber cannot be varied in a practical measurement. Therefore, we shall consider modeling random processes by dynamical systems as considered in ergodic theory since the formulation and proof of ergodic theorems are more natural in the dynamical system context.

The basic focus of the ergodic theory is the development of conditions under which sample or time averages consisting of arithmetic means of a sequence of measurements on a random process converged to a probabilistic or ensemble average of the measurement. This analysis then can be extended to the channel matrix. Considering:

$$\boldsymbol{R}(\xi_1, \xi_2) = \langle \boldsymbol{U}(\xi_1)\boldsymbol{U}^{\dagger}(\xi_2)\rangle, \qquad \textit{Equation 2.21}$$

as expected, the ensemble average converges to a weighted identity with the weight decaying as the difference between ξ_1 and ξ_2. Here ξ is any variable (time, frequency, space). The output Stokes space parameters, were measured in different time segments. The averaged measurement results are then compared with the result of non-linear methods of spectral analysis.

In order to see the temporal behavior of the data, the time correlation structure of the data obtained from the test with the 20 km long indoor fiber with duration of 38 hours has been explored. Fig. 2.4. shows the zero cross-correlation between the first component and the other two components that has been calculated by computing short time cross-correlations as a function of the displacement (lag) of one relative to the other. The short time cross-correlations between the second (third) component and the other two components demonstrated results rather identical to those in Fig. 2.4 which implicates that the components are uncorrelated, and for a Gaussian process is equivalent to independence. The cumulative probability functions of the second birefringence components (h_2) for both 1545 nm and 1555 nm wavelengths has been computed and shown in Fig. 2.5 which implicates that the result is consistent with Gaussian statistics. The cumulative probability function of the first (h_1) and third (h_3) birefringence component follows the same pattern. As indicated in Fig. 2.3, no non-stationary behavior (e.g. periodicity corresponding to day/night) has been found. The result predicts each component to be independent identically distributed zero mean Gaussian processes. The results of the single mode case are easily generalized to the multimode case. In the multimode case, the relevant group becomes SU(2n). The algebra is su(2n) for which the Gell-Mann matrices [65] form a basis.

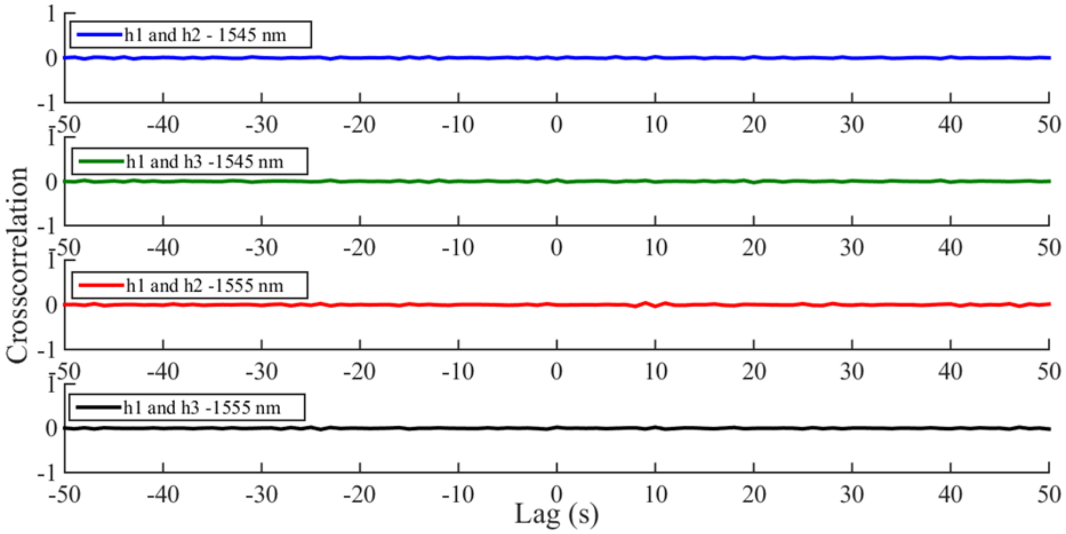

Fig. 2.4. Crosscorrelation between components of the birefringence vector ($\boldsymbol{h}$) for 1545 nm and 1555 nm wavelengths. h_1, h_2, and h_3 corresponds to first, second and third components of the 3 dimensional birefringence vector ($\boldsymbol{h}$).

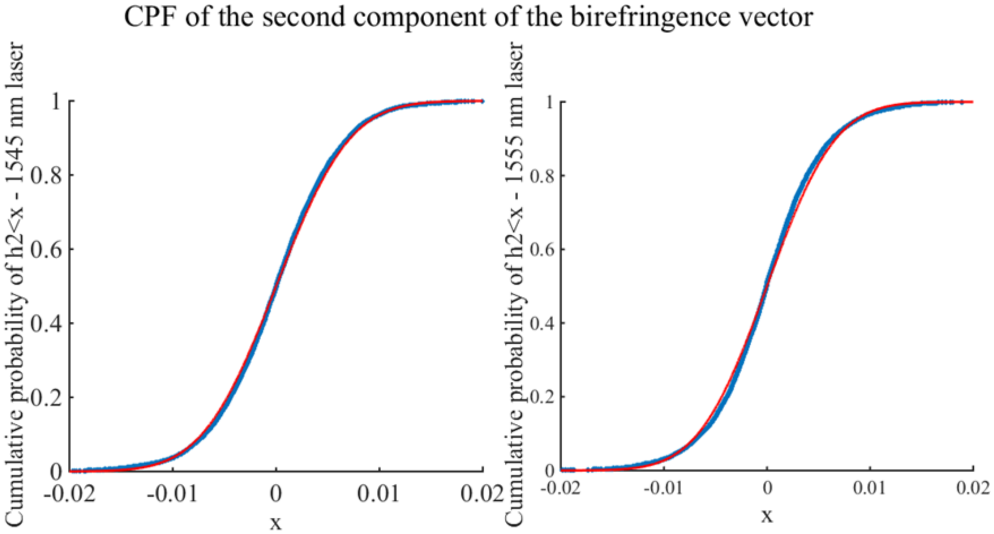

Fig. 2.5. The cumulative probability distribution of the second component (h_2) of the three-dimensional birefringence vector $\boldsymbol{h}$ for two laser wavelengths of 1545 nm and 1555 nm. Solid red line denotes the standard normal distribution and the blue dots denote to the recorded data distribution.

2.7 Conclusion

This chapter studied the evolution of the state of polarizations in a single mode fiber as a coherent transmission medium. A single mode fiber channel of fixed length is characterized by the drift in time of the frequency dependent state-of-polarization. It has been realized that the Poole's equation is the Lax pair in terms of Lie Groups and algebras which is an improvement in appreciation of ad hoc algebra. Also, the stochastic differential equation is derived which dynamically solves the evolution of the state of polarization with distance rather than time.

The experimental results verified the assumption of each birefringence component being independent identically distributed zero mean Gaussian processes. This result is important since it provides realistic requirements for the construction of mathematical models of physical random phenomena. The results obtained for the single mode fiber can be simply generalized to the multimode case.

3 Chapter: Symmetric signal and local oscillator polarization diverse coherent optical receiver

3.1 Introduction

Digital coherent optical receivers are an inseparable component of modern optical communication systems. The capability of demodulating optical signals employing advanced modulation formats, which provide enhanced spectral efficiency, is amongst their noteworthy properties [66]. Detecting both the real and imaginary parts of the electrical field of propagating light permits the compensation of linear impairments such as chromatic dispersion in fiber-optic transmission systems, which is effectively possible through coherent optical receivers enhanced by digital signal processing (DSP) [67-69]. DSP can also enable polarization mode dispersion mitigation despite its stochastic nature [70]. Laboratory demonstrations and field trials have confirmed the theoretical predictions and have made possible the practical realization of high capacity coherent optical transmission systems. Numerous studies have investigated new algorithms and structures to improve the capability of coherent receivers. This has led to the elimination of some optical components such as the wavelength dispersion compensation module and variable dispersion compensator used in conventional systems [71-82]. The transmission capacity has been improved from the de facto 10 Gbit/s limit of previous systems to recent demonstrations of 1 Tbit/s per-channel. In addition, equalization of waveform distortions can be performed adaptively through DSP.

The front-end of a conventional polarization diverse coherent optical receiver transforms the complex amplitude of the optical field into the electrical domain by homodyne detection yielding four outputs, namely the in-phase and quadrature (IQ) components of the complex amplitudes for horizontal and vertical signal polarizations [83-86]. In these typical polarization diverse coherent optical receivers, one input port is allocated to an intense laser operating as a local oscillator (LO) with fixed polarization (a known and time-invariant state of polarization (SOP)) and the other port to an amplitude and phase modulated signal, which in the general case has a time-varying SOP after its propagation through several kilometers of optical fiber [87,88]. In this chapter, an alternative yet original approach is proposed that provides an opportunity to design a coherent optical receiver that accommodates a random time-varying SOP for both the LO and signal [89,90]. The proposed architecture comprises two conventional coherent optical receiver front-ends in tandem, where the SOP of the LO is first divided into its two orthogonal components and then distributed to each coherent optical receiver front-end module. The advantages of this architecture are twofold. On the one hand, it may facilitate the use of an off-the-shelf laser source performing as a LO with arbitrary SOP. On the other hand, it may motivate the distribution of the LO from the fiber network or central offices, releasing the need for a LO laser and the associated power demand of the thermo-electric coolers at the location of the optical coherent receiver. To correctly combine the signals, two distinct techniques of dual port polarization diversity based on the MRC method have been used. The concept is validated by numerical simulations, where a differential quadrature phase-shift keyed (DQPSK) signal and a LO field both subject to an independent random time-varying SOP are first generated. The signal and LO fields are mixed by the two receiver front-ends to provide eight baseband variables that are digitally processed by the MRC algorithm. The eight variables are the in-phase and quadrature components of the four products of the two components of the signal

Jones vector and the complex conjugate of the two components of the LO Jones vector. Accurate recovery of the modulated input signal is obtained and illustrated by constellation diagrams. The rest of the chapter is organized as follows. The proposed architecture of a true polarization diverse coherent optical receiver for both signal and LO is described in section 3.2. The dual port polarization diversity approach based on MRC is presented in section 3.3, along with two variants of the MRC method. Numerical results that validate the proposed approach are presented in section 3.4. The chapter closes with the drawing of important conclusions.

3.2 Proposed coherent optical receiver architecture

In conventional polarization diverse coherent receivers, the LO must be linearly polarized; either horizontal polarization is used (transverse electrical (TE)) followed by a beam splitter (BS), or alternatively linear polarization inclined at 45 degrees is used followed by a polarization beam splitter (PBS), where inevitably a polarization rotator is needed to convert the transverse magnetic (TM) output of the PBS to TE. Unlike the LO, the input signal possesses an arbitrary SOP and its orthogonal components are split by a PBS. This expedient is necessary irrespective of whether or not the signal is single- or dual- polarization multiplexed at the transmitter. In the latter case, the drifting SOP results in the two modulated components of the transmitted signal being present within the two components of the polarization of the received signal in the form of two different slowly time-varying linear combinations. These mixtures may be demultiplexed subsequently by DSP on the basis of the independence of the modulations. The optical signals are organized using a polarization rotator as appropriate into two co-polarized signal-LO pairs corresponding to the two combinations of the two components of the signal and the single component of the LO polarization. The co-polarized signal-LO pairs pass through the 90-degree hybrid modules, are mixed by the balanced photoreceivers to form baseband electrical signals, which are digitized by the analog to digital converters and then processed by the DSP module. The structure of the conventional coherent receiver is depicted in Fig. 3.1 [91-96].

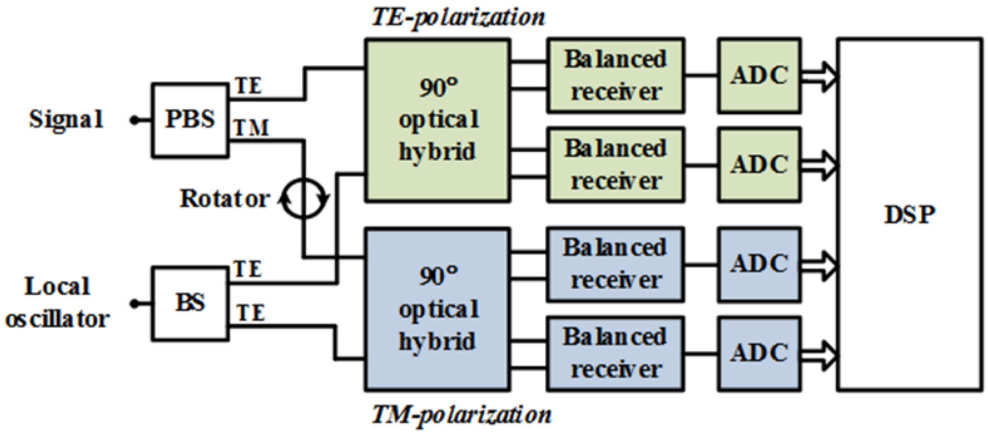

Fig. 3.1. Schematic diagram of a conventional polarization diverse coherent receiver. Polarization diversity refers to the input signal. TE (horizontal) and TM (vertical) polarization components are illustrated in green and blue, respectively.

If the SOP of both signal and reference are allowed to be subject to drift, it is likely that the pair of components entering each of the 90-degree hybrids fade simultaneously. In this situation, the output of the conventional coherent receiver will be degraded, resulting in a poor signal-to-noise ratio (SNR) at the DSP sampling time. The idea of classical diversity techniques is duplication of information: a diversity receiver coherently combines multiple replicas of the transmitted signal. If the replicas fade independently, the probability of the combined signal fading is substantially reduced. To improve the performance of the conventional coherent receiver, rather than combining the signals generated by the two components of the signal polarization, the diversity technique applied in the DSP module may be extended to combine the four signals generated by all combinations of the two polarization components of the signal and LO after the polarization of the pairs of components, which generate the diversity signals, are brought into alignment. The practical realization of the diversity approach can be achieved by considering the proposed architecture of a coherent optical receiver shown in Fig. 3.2. It comprises a pair of two conventional coherent optical receiver front-ends with the addition of an input stage of beam splitters for signal and LO, which are used to form the four combinations of their polarization components. The proposed architecture can be understood as symmetric because the input ports used for the signal and reference inputs may be interchanged with no effect on the operation of the receiver.

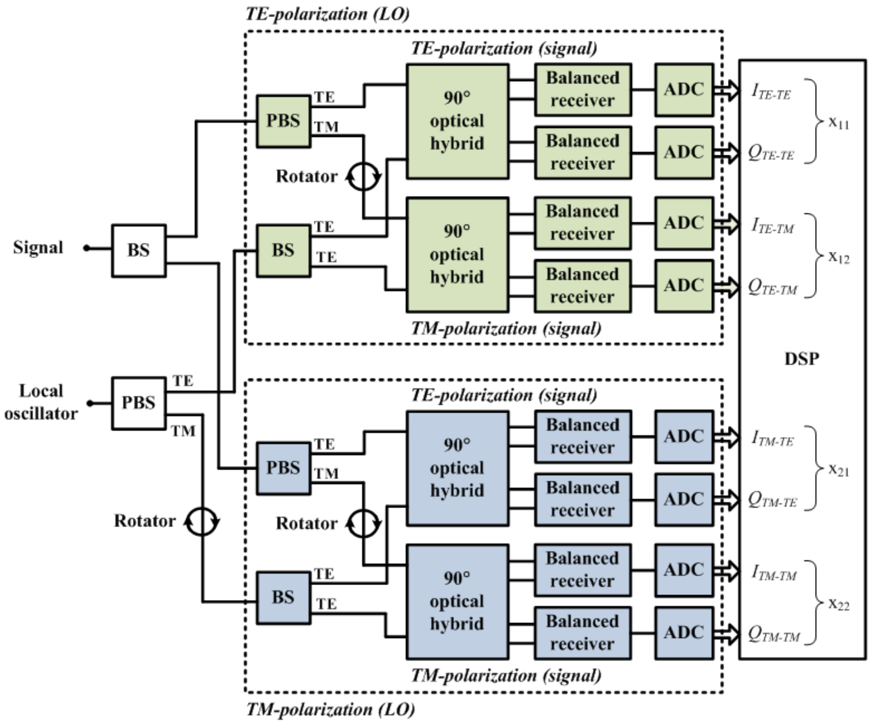

Fig. 3.2 Proposed schematic of a symmetric polarization diverse coherent receiver for both signal and local oscillator. Modules making use of the TE (horizontal) and TM (vertical) polarizations of the local oscillator are illustrated in green and blue, respectively.

3.3 Theoretical approach

3.3.1 Maximal Ratio Combining

MRC is a technique commonly used in wireless communications to mitigate fading due to multi-path reception. The idea is to form a weighted combination of several channels each containing a replica of the signal with greater weight given to channels with higher signal to noise ratio and lower weight given to channels with lower signal to noise ratio. For independent additive white Gaussian noise (AWGN) channels, the optimum weights are proportional to the channel SNR. Multipath reception also results in the replica of the signal having different carrier phases from channel to channel. It is, therefore, essential that the replicas are all brought into carrier phase alignment so that the replicas sum coherently. In other words, MRC method works as a matched filter in the spatial domain. By using MRC on independently fading channels, the probability of an outage due to all channels fading simultaneously decreases rapidly with number of channels being combined. The architecture of the MRC approach is shown in the schematic diagram of Fig. 3.3.

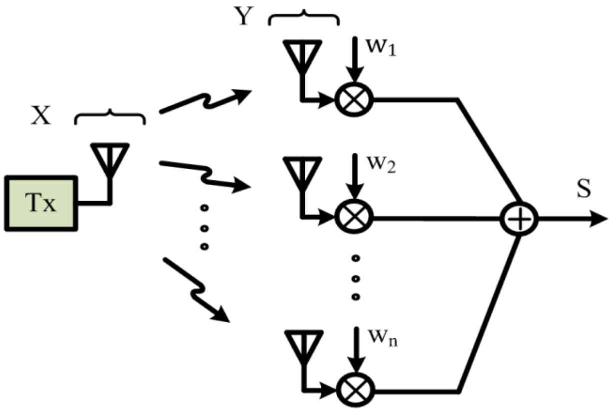

Fig. 3.3. Maximal ratio combining is deployed as the polarization diversity technique to combine the multiple received signals. T_x: transmitter, X: transmitted signal, Y: received signal, w_i: weights, S: weighted sum.

In the case of fading caused by polarization drift, the fading of the diversity channels is anti-correlated which is advantageous because it is then impossible for the output of the diversity combiner to fade. Indeed, by properly combining the diversity channels, the output can be rendered independent of the SOP of both signal and LO. In the case of a single-port (dual-port) polarization diverse coherent optical receiver, there are two (four) diversity channels corresponding to the number of homodyne beat signals generated by the two (four) combination of the two components of the signal polarization and the one (two) component(s) of the polarization of the LO after the polarization of these components are brought into alignment by polarization rotators. The state of polarization of the signal and the LO are described by the two complex components (TE & TM) of their respective unit Jones vectors. The two (four) baseband signals correspond to the product of each of the components of the signal Jones vector with the complex conjugate of the one (two) component(s) of the LO Jones vector. In the case of single-port polarization diversity, the diversity signals correspond to signal-LO polarization component pairs TE-TE and TM-TE. As the signal SOP varies, it is possible for one of these two signals to fade. Provided fading is entirely due to SOP drift (and not due to fading of the overall signal intensity) when one component of a Jones vector fades the other component becomes strong. It is therefore not possible for both diversity channels to fade simultaneously when the LO polarization is fixed appropriately. Similarly, in the case of dual-port polarization diversity, the diversity signals correspond to signal-LO polarization component pairs TE-TE, TE-TM, TM-TE, and TM-TM. As the signal and LO SOP vary independently, it is possible that a pair of the four signals generated corresponding to the same component of the signal polarization fade. Similarly, it is possible that a pair of the four signals generated corresponding to the same component of the LO polarization fade. However, provided fading is entirely due to SOP drift (and not due to fading of the overall signal intensity), then when one component of a Jones vector fades the other component becomes strong. It is, therefore, impossible for all four of the generated signals to fade simultaneously.

Let the N diversity signals to be combined be represented by the components of a complex vector $\boldsymbol{y} = \boldsymbol{x} + \boldsymbol{\varepsilon}$, where the complex vector $\boldsymbol{x}$ represents the wanted signals and $\boldsymbol{\varepsilon}$ represents additive noise. The diversity combiner forms the weighted sum $s(\boldsymbol{y}) = (\boldsymbol{y}, \boldsymbol{w})$, where $(\boldsymbol{u}, \boldsymbol{v}) = \sum_{j=1,N} \boldsymbol{u}_j \boldsymbol{v}_j^*$ is the standard inner product, s is a linear functional and the weight vector is defined as $\boldsymbol{w} = [\, w_1 \;\; w_2 \; \ldots w_n]^T$, with $\|\boldsymbol{w}\|^2 = (\boldsymbol{w}, \boldsymbol{w}) = 1$. The objective is to maximize the signal power to noise power ratio:

$$\mathcal{E} = \frac{\langle |s(\boldsymbol{x})|^2 \rangle}{\langle |s(\boldsymbol{\varepsilon})|^2 \rangle} = \frac{\boldsymbol{w}^\dagger \langle \boldsymbol{x}\boldsymbol{x}^\dagger \rangle \boldsymbol{w}}{\boldsymbol{w}^\dagger \langle \boldsymbol{\varepsilon}\boldsymbol{\varepsilon}^\dagger \rangle \boldsymbol{w}} \qquad \textit{Equation 3.1}$$

where $\langle \cdot \rangle$ denotes the ensemble average, $\langle \boldsymbol{x}\boldsymbol{x}^\dagger \rangle$ is the covariance of the signal and $\langle \boldsymbol{\varepsilon}\boldsymbol{\varepsilon}^\dagger \rangle$ is the covariance of the noise. The purpose of the ensemble averaging is to isolate the slowly varying part of the signal due to fading from any rapidly varying part due to modulation. In practice, the ensemble averages must be estimated using short-time averages.

Equating to zero the Fréchet derivative [97] of $\mathcal{E}$ with respect to $\boldsymbol{w}^\dagger$ leads to the generalized eigenvector–eigenvalue problem: $\langle \boldsymbol{x}\boldsymbol{x}^\dagger \rangle \boldsymbol{w} = \lambda \langle \boldsymbol{\varepsilon}\boldsymbol{\varepsilon}^\dagger \rangle \boldsymbol{w}$, where $\lambda = [\boldsymbol{w}^\dagger \langle \boldsymbol{x}\boldsymbol{x}^\dagger \rangle \boldsymbol{w}]/[\boldsymbol{w}^\dagger \langle \boldsymbol{\varepsilon}\boldsymbol{\varepsilon}^\dagger \rangle \boldsymbol{w}]$ is automatically satisfied by any eigenvector–eigenvalue pair. The eigenvalue is the signal to noise power ratio (SNR) at the output of the combiner and hence the eigenvector corresponding to the largest eigenvalue yields the optimum weight vector. Since the noise covariance matrix is positive definite and, therefore, has a square root, setting $\boldsymbol{u} = \langle \boldsymbol{\varepsilon}\boldsymbol{\varepsilon}^{\dagger} \rangle^{1/2} \boldsymbol{w}$ yields the standard eigenvector–eigenvalue problem:

$$\left(\langle \varepsilon\varepsilon^{\dagger} \rangle^{-1/2} x\right)\left(\langle \varepsilon\varepsilon^{\dagger} \rangle^{-1/2} x\right)^{\dagger} \boldsymbol{u} = \lambda \boldsymbol{u} \qquad \textit{Equation 3.2}$$

The term on the left-hand side of Eq. 3.2 is a non-negative definite projection operator onto the one-dimensional subspace spanned by $\langle \boldsymbol{\varepsilon}\boldsymbol{\varepsilon}^{\dagger} \rangle^{-1/2} \boldsymbol{x}$. There is therefore only one non-zero eigenvalue that corresponds to an eigenvector lying in the complex subspace of all scalar multiples of the vector. $\overline{\boldsymbol{w}} = \langle \boldsymbol{\varepsilon}\boldsymbol{\varepsilon}^{\dagger} \rangle^{-\mathbf{1}} \overline{\boldsymbol{x}} / \left\| \langle \boldsymbol{\varepsilon}\boldsymbol{\varepsilon}^{\dagger} \rangle^{-\mathbf{1}} \boldsymbol{x} \right\|$. The normalization of the weight vector is also effective at removing amplitude modulation if the modulation index is less than 100%.

As first formulated, one needs to know separately the covariance of the signal $\langle \boldsymbol{x}\boldsymbol{x}^{\dagger} \rangle$ and noise $\langle \boldsymbol{\varepsilon}\boldsymbol{\varepsilon}^{\dagger} \rangle$. Consider a second formulation in which the objective is to maximize the signal plus noise power subject to the constraint of a weight of unit norm. The objective function is then:

$$\mathcal{E} = \boldsymbol{w}^{\dagger} \langle \boldsymbol{y}\boldsymbol{y}^{\dagger} \rangle \boldsymbol{w} + \boldsymbol{\lambda}(1 - \boldsymbol{w}^{\dagger}\boldsymbol{w}) \qquad \textit{Equation 3.3}$$

where λ is a Lagrange multiplier. Equating to zero the Fréchet derivative of $\mathcal{E}$ with respect to $\boldsymbol{w}^{\dagger}$ yields the eigenvector–eigenvalue problem $\langle \boldsymbol{y}\boldsymbol{y}^{\dagger} \rangle \boldsymbol{w} = \lambda \boldsymbol{w}$ which has the merit that an estimate of the covariance of the signal plus noise only is required. The optimum weight again corresponds to the largest eigenvalue. Moreover, assuming the noise and signal are uncorrelated then $\langle \boldsymbol{y}\boldsymbol{y}^{\dagger} \rangle = \langle \boldsymbol{x}\boldsymbol{x}^{\dagger} \rangle + \langle \boldsymbol{\varepsilon}\boldsymbol{\varepsilon}^{\dagger} \rangle$ and the eigenvalue is equal to the signal power plus the noise power at the output of the combiner. In addition, if the noise in each channel is independent and has identical variance σ^2 then $\langle \boldsymbol{\varepsilon}\boldsymbol{\varepsilon}^{\dagger} \rangle = \sigma^2 \boldsymbol{I}$. The eigenvectors found are then identical to that found in the first formulation. Given a suitable estimator of $\langle \boldsymbol{y}\boldsymbol{y}^{\dagger} \rangle$ and sufficient signal to noise ratio, the variance of the estimate will not interchange the eigenvectors ranked by eigenvalue and the eigenvector with largest eigenvalue will agree with the first formulation.

Although $\bar{\boldsymbol{w}}$ has unit norm by construction and is an eigenvector corresponding to the largest eigenvalue and therefore is a valid weight vector that maximizes the SNR, it is not uniquely defined and one cannot simply set $\boldsymbol{w} = \bar{\boldsymbol{w}}$. This follows from the invariance of $\boldsymbol{y}\boldsymbol{y}^{\dagger}$ to multiplication of $\boldsymbol{y}$ by a unimodular phase factor and the equivalence of eigenvectors under multiplication by a unimodular phase factor. The current weight vector $\boldsymbol{w}_{n+1}$ is consequently determined recursively by the update rule:

$$\boldsymbol{w}_{n+1} = (\boldsymbol{w}_n, \bar{\boldsymbol{w}}_{n+1})\bar{\boldsymbol{w}}_{n+1}, \qquad \textit{Equation 3.4}$$

where $\bar{\boldsymbol{w}}_{n+1}$ is the current eigenvector and $\boldsymbol{w}_n$ is the previous weight vector. The recursion is initialized by setting $\boldsymbol{w}_0 = \bar{\boldsymbol{w}}_0$. Note this update rule is invariant to the particular eigenvector selected to represent its equivalence class under scaling by a unimodular phase factor. The unimodular phase factor $(\boldsymbol{w}_n, \bar{\boldsymbol{w}}_{n+1})$ ensures that w_{n+1} is the closest valid current eigenvector to the previous weight vector (recall $\|\boldsymbol{w}_n\| = \|\bar{\boldsymbol{w}}_{n+1}\| = 1$). This simple expedient tracks the component to the carrier phase contributed by the diversity combiner and prevents any wild variations of the phase due the peculiarities of the process of selection of a representative eigenvector by a particular eigenvector–eigenvalue solution method.

3.3.2 Dual polarization diversity

The in-phase and quadrature signals provided by the balanced photodetectors at the outputs of the hybrids (Fig. 3.2) form the four complex beat signal components $x_{jk} = (\boldsymbol{E}_s, \boldsymbol{e}_j)(\boldsymbol{E}_r, \boldsymbol{e}_k)^*$, where $\boldsymbol{E}_s$ and $\boldsymbol{E}_r$ are the Jones vectors representing the signal and reference (LO) fields and $\boldsymbol{e}_1 \boldsymbol{e}_2$ are orthonormal Jones vectors that represent the linear TE and TM polarizations. These four components x_{jk} constitute a 2×2 complex matrix signal formed by the outer product of the signal and the reference field vectors $\boldsymbol{X} = \boldsymbol{E_s}\boldsymbol{E_r^\dagger}$. One may then write $\boldsymbol{Y} = \boldsymbol{X} + \boldsymbol{E}$, where $\boldsymbol{Y} = [y_{11} \quad y_{12} \quad ; \quad y_{21} \quad y_{22}]$ represents the signal plus noise, $\boldsymbol{X} = [x_{11} \quad x_{12} \quad ; \quad x_{21} \quad x_{22}]$ represents the signal and $\boldsymbol{E} = [E_{11} \quad E_{12} \quad ; \quad E_{21} \quad E_{22}]$, represents additive white Gaussian noise. Similarly, one can define a 2×2 weight matrix $\boldsymbol{W} = [w_{11} \quad w_{12} \quad ; \quad w_{21} \quad w_{22}]$. The diversity combiner forms the weighted sum $\boldsymbol{S}(\boldsymbol{Y}) = [\boldsymbol{Y}, \boldsymbol{W}]$ where the Frobenius inner product of 2×2 complex matrices is defined by $[\boldsymbol{U}, \boldsymbol{V}] = \mathrm{Tr}(\boldsymbol{U}\boldsymbol{V}^\dagger) = \sum_{j=1,2} u_{jj} v_{jj}^*$, and S is a linear functional. The signal plus noise power from the combiner is $\langle|\boldsymbol{S}|^2\rangle = [\langle\mathbb{P}\rangle\boldsymbol{W}, \boldsymbol{W}]$, where $\mathbb{P}(\cdot) = [\cdot, \boldsymbol{Y}]\boldsymbol{Y}$ is a linear operator on matrices representable in a suitable basis as a 4×4 matrix $\mathbb{P} \equiv \boldsymbol{Y} \otimes \boldsymbol{Y}^\dagger$ where $\otimes$ is the Kronecker tensor product. In the following, two different methods of dual-port polarization diversity are described.

3.3.2.1 Unconstrained weight matrix method

Following the second formulation of the MRC method, the objective is to maximize the mean signal plus noise power subject to the constraint that the weight vector has unit norm. The objective function $\mathcal{E}$ is then:

$$\mathcal{E} = [\langle\mathbb{P}\rangle \circ \boldsymbol{W}, \boldsymbol{W}] + \lambda\{1 - [\boldsymbol{W}, \boldsymbol{W}]\} \qquad \textit{Equation 3.5}$$

where λ is a Lagrange multiplier. Equating the Fréchet derivative of $\mathcal{E}$ with respect to $\boldsymbol{W}^\dagger$ (or $\boldsymbol{W}$) to zero yields the eigenvector–eigenvalue problem: $\langle\mathbb{P}\rangle \circ \boldsymbol{W} = \lambda\boldsymbol{W}$. If the weight matrix $\boldsymbol{W}$ is an eigenvector, then $\mathcal{E}$ will be equal to λ. If the fluctuation of $\boldsymbol{Y}$ is entirely due to identically distributed independent AWGN, then the only change to $\langle\mathbb{P}\rangle$ is the addition of an identity weighted by the noise variance. This raises the value of eigenvalues by the noise variance and leaves the eigenvector with the largest eigenvalue unchanged. Given a suitable estimator of $\langle\mathbb{P}\rangle$ and sufficient signal to noise ratio, the variance of the estimate will not interchange the eigenvectors ranked by eigenvalue and the eigenvector with largest eigenvalue will provide the optimum weight matrix.

3.3.2.2 Constrained weight matrix method

A tighter constraint is provided by a weight matrix defined as the outer product of two vectors: $\boldsymbol{W} = \boldsymbol{u}\boldsymbol{v}^\dagger$, in which case: $\mathcal{E} = [\langle \mathbb{P} \rangle \circ (\boldsymbol{u}\boldsymbol{v}^\dagger), \boldsymbol{u}\boldsymbol{v}^\dagger] + \lambda\{1 - [\boldsymbol{u}\boldsymbol{v}^\dagger, \boldsymbol{u}\boldsymbol{v}^\dagger]\}$. Equating the Fréchet derivative of $\mathcal{E}$ with respect to $u^\dagger$ and $v^\dagger$ reduces the problem to a pair of two-dimensional eigenvector–eigenvalue problems:

$$\begin{aligned} \boldsymbol{X}^\dagger \boldsymbol{X} \boldsymbol{v} &= (\lambda - \sigma^2)\boldsymbol{v} \\ \boldsymbol{X}\boldsymbol{X}^\dagger \boldsymbol{u} &= (\lambda - \sigma^2)\boldsymbol{u} \end{aligned}$$

Equation 3.6

Naturally, $\boldsymbol{Y}^\dagger\boldsymbol{Y}$ and $\boldsymbol{Y}\boldsymbol{Y}^\dagger$share the same eigenvalues and so the common eigenvalue λ is not an issue. The choice of normalization $(\boldsymbol{u}, \boldsymbol{u}) = 1$ and $(\boldsymbol{v}, \boldsymbol{v}) = 1$ ensures that $[\boldsymbol{W}, \boldsymbol{W}] = 1$. Under the same assumptions regarding noise as in the preceding, the optimum weight matrix $\overline{\boldsymbol{W}} = \overline{\boldsymbol{u}}\overline{\boldsymbol{v}}^\dagger$ is given by the outer product of the eigenvectors $\overline{\boldsymbol{u}}, \overline{\boldsymbol{v}}$ corresponding to the largest eigenvalue.

The virtue of the constrained method is that only a pair of two-dimensional eigenvector–eigenvalue problems is involved which may be solved analytically rather than a four-dimensional eigenvector–eigenvalue problem which is best solved numerically. The analytic calculations require the explicit form of $\langle \boldsymbol{Y}^\dagger\boldsymbol{Y} \rangle$ and $\langle \boldsymbol{Y}\boldsymbol{Y}^\dagger \rangle$ as follows:

$$\langle \boldsymbol{Y}^\dagger\boldsymbol{Y} \rangle = \begin{bmatrix} \langle y_{11}^* y_{11} \rangle + \langle y_{21}^* y_{21} \rangle & \langle y_{11}^* y_{12} \rangle + \langle y_{21}^* y_{22} \rangle \\ \langle y_{12}^* y_{11} \rangle + \langle y_{22}^* y_{21} \rangle & \langle y_{12}^* y_{12} \rangle + \langle y_{22}^* y_{22} \rangle \end{bmatrix}$$

Equation 3.7

and:

$$\langle \boldsymbol{Y}\boldsymbol{Y}^\dagger \rangle = \begin{bmatrix} \langle y_{11} y_{11}^* \rangle + \langle y_{12} y_{12}^* \rangle & \langle y_{11} y_{21}^* \rangle + \langle y_{12} y_{22}^* \rangle \\ \langle y_{21} y_{11}^* \rangle + \langle y_{22} y_{12}^* \rangle & \langle y_{21} y_{21}^* \rangle + \langle y_{22} y_{22}^* \rangle \end{bmatrix}$$

Equation 3.8

Although each of these two matrices is constructed from eight components of the covariance matrix; together they do not exhaust all sixteen components of the covariance matrix encoded in the tensor ⟨ℙ⟩. Taking Hermitian symmetry into account, there are ten independent components of which six are used.

3.4 Architecture of DSP module

The first step towards the validation of the theoretical approach developed in the preceding section is the generation of a differential-QPSK modulated signal at the transmitter. Even and odd bits of a binary non-return-to-zero (NRZ) data stream are split and used to modulate the amplitude of an in-phase and quadrature phase copy of a common carrier which are combined to generate the four states of the QPSK signal. After both in-phase and quadrature components of the signal are coherently detected and conditioned to form the signals x_{ij}, DSP algorithms are applied to recover the transmitted data. As illustrated in Fig. 3.4, the DSP module consists of four subsystems: 1) dispersion compensation, 2) polarization diversity, 3) carrier phase estimation, and 4) demodulation and visualization of recovered data. Each of these subsystems is briefly described in the following subsections.

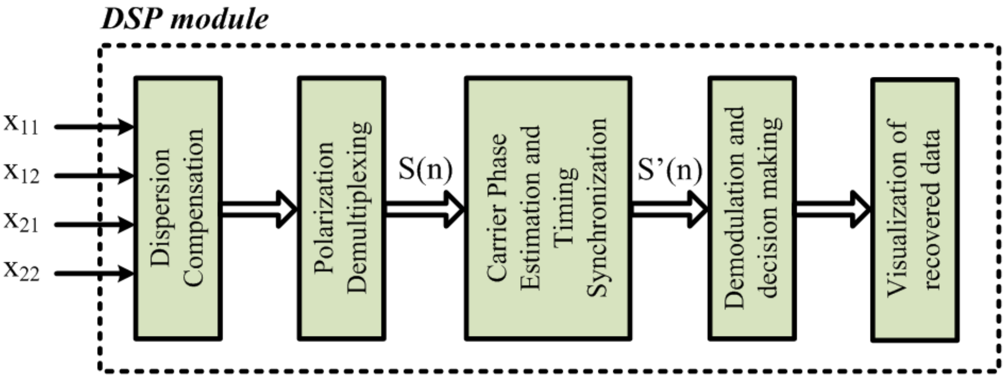

Fig. 3.4. Architecture of DSP module at the end of coherent receiver

3.4.1 Dispersion compensation

In a single mode fiber, polarization mode dispersion (PMD) is a random phenomenon that takes place due to birefringence in the fiber that originates from asymmetry caused by an elliptical core, stress, bend, or twist. PMD stems from the random birefringence which yields different group velocities of the two orthogonal polarizations modes. This polarization effect causes mode coupling and random changes in SOP in a long haul transmission [98,99]. Since the existence of PMD and chromatic dispersion (CD) in optical transmission causes inter-symbol-interference (ISI) in high speed systems, dispersion compensation techniques using DSP are essential for mitigation of linear dispersion effects and has been regarded as one of the important approaches to increase the capacity of high data rate optical transmission systems [100,101]. Neglecting fiber nonlinearity, the single mode fiber can be considered as a phase-only filter having the transfer function of:

$$F(z,\omega) = \exp\left(-j\frac{D\lambda^2 z}{4\pi c}\omega^2 + j\frac{S\lambda^4 z}{24\pi^2 c^2}\omega^3\right), \qquad \textit{Equation 3.9}$$

which represents fiber dispersion and the dispersion slope for multi-channel application. In Eq. 3.9 ω is the angular frequency, λ is wavelength, z is propagation distance, c is the speed of light in vaccum, D is dispersion coefficient in fiber, S is the residual dispersion slope, and j denotes the complex number$\sqrt{-1}$. It is clear that multiplication of the output to the inverse of this transfer function results in dispersion effect compensation [102].

3.4.2 Polarization diversity

This block implements the algorithms described in section 3 in order to select the eigenvector with largest eigenvalue as weight vector for the purpose of polarization demultiplexing.

3.4.3 Carrier phase estimation

The phase of the carrier is unknown and must be retrieved from the received signal. Here, a carrier phase recovery subsystem is implemented for the special case of DQPSK. As shown in Fig. 3.5, the approach consists of raising the complex combined signal (i.e., the output of the MRC module) to the fourth power in order to remove the modulation, phase unwrapping to provide continuity in time, and then dividing by four to provide the compensatory phase [103]. The use of DQPSK modulation overcomes a residual sign ambiguity.

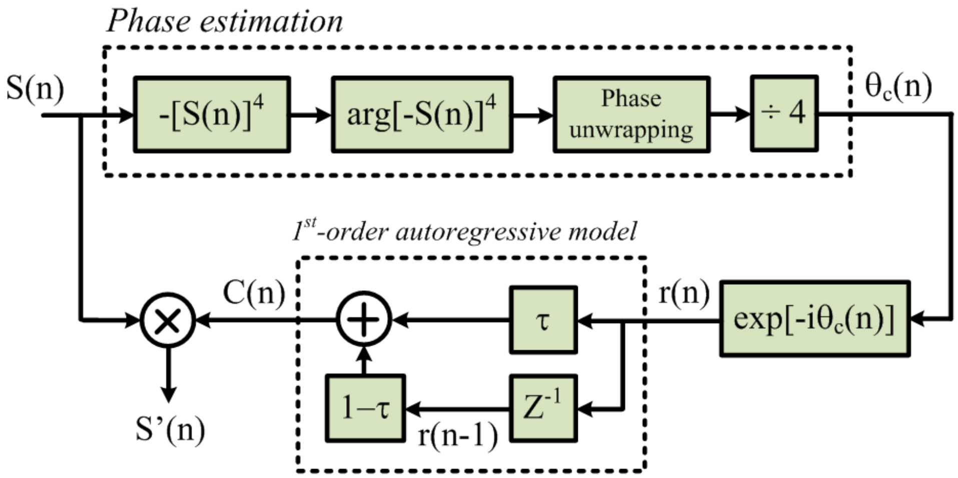

Fig. 3.5. Carrier phase estimation and timing synchronization subsystems

3.4.4 Demodulation: sign ambiguity resolution and error estimation

In DQPSK the information is carried by the phase difference between two consecutive symbols, the current symbol is detected using the prior symbol as a reference and a $\pi/4$ rotation of the constellation is performed to simplify the symbol decision. As illustrated in Fig. 3.6, a multiplication of the current symbol by the complex conjugate of the previous symbol is performed for both received and transmitted data. In the decision unit, the sign of both real and imaginary parts of the products are compared respectively. An indication that the received and transmitted symbols are located in different quadrants is detected if the sign of the real parts (or the sign of the imaginary parts) of the received product is different from the corresponding transmitted product. A decision is made based on the error flag and the demodulation histogram is visualized according to the number of detected symbols in each quadrant.

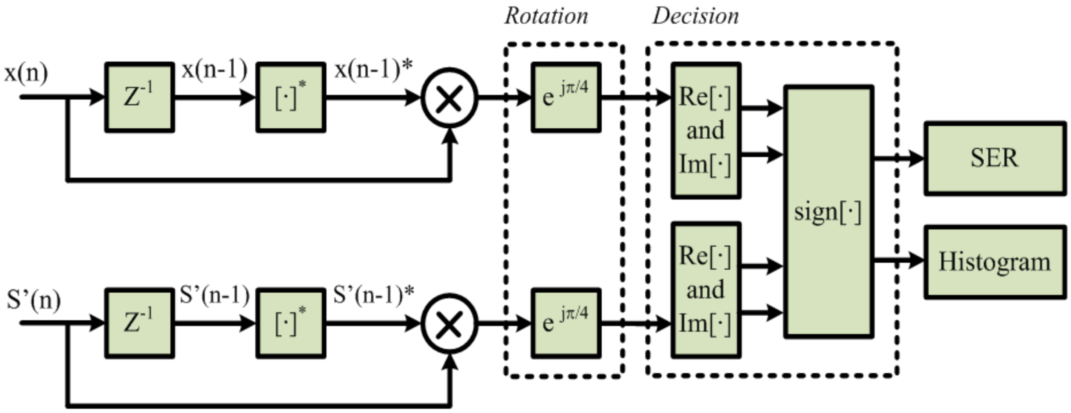

Fig. 3.6. DQPSK demodulation histogram and error visualization

3.5 Simulation results

The performance of the proposed architecture of true polarization diverse coherent receiver is assessed by numerical simulations for both constrained and unconstrained

MRC methods. A 100 Gbps coherent dual polarization DQPSK Transmission system with DSP is simulated. Linear dispersion effect is modeled using Eq. 3.9. Independent randomly-drifted states of polarization for reference and signal are modeled as a Brownian motion on the SU(2) manifold [104-107] which is isomorphic to the three-dimensional surface of the sphere in four dimensions S^3. The motion on S^3 is locally approximated by a random walk on its tangent plane $\mathbb{R}^3$. Random vectors in $\mathbb{R}^3$ with independent zero mean unit variance Gaussian distributed components are generated to construct via the Pauli matrix basis instances of 2×2 traceless anti-Hermitian matrices which represent the tangent vectors at a discrete point on a path in SU(2). The tangent vectors are transformed into an element of SU(2) via the exponential map with parameter δt that describes a step on the path on the manifold. This provides a good approximation to Brownian motion on the sphere when the step size is small compared to the inverse curvature of the sphere. Each point on the path is an element of SU(2) whose action on an initial Jones vector (i.e. $\boldsymbol{e}_1$ or $\boldsymbol{e}_2$) at the transmitter yields the corresponding drifting Jones vector at the receiver. The duration of drift (T) and Brownian motion deviation (δt) are set to be 10 and $\sqrt{T/_n}$, respectively, where the number of samples (n) is set to 10^6 to allow SOP variations over many 2π cycles. The drifting SOP is visualized as a motion on the Poincaré sphere. Considerations of memory size limit the total number of samples one may use in one simulation run. One sample per symbol of 25 million at a representative symbol rate of 25 GSs^{-1}, leads to a sample path with a total duration of 1 ms. Over that time period, the SOP at the end of a fiber-optic link is likely to be essentially static. This could be modeled by generating an instance of a SOP for both signal and LO and holding it throughout the duration of the simulation. However, to properly demonstrate the capability of the algorithms to adapt to a drifting polarization state, the SOP must be updated during the simulation. The consecutive states of polarization are computed after a block of AWGN channel samples with programmable length, rather than at every sample. In the simulations reported in this chapter, each state of polarization is updated after 25 samples. The SOP drift modeled is therefore far more aggressive that one might expect to encounter in practice. It is noteworthy that an algorithm that copes with an aggressive simulation will encounter no difficulty with the more benign reality. The electrical SNR is set to 20 dB for all channels. Random-drifting states of polarizations mapped onto the Poincaré sphere for the signal are shown in Figs. 3.7(a) and 3.7(b). Similar yet distinct traces are obtained for the polarization drift simulated for the LO.

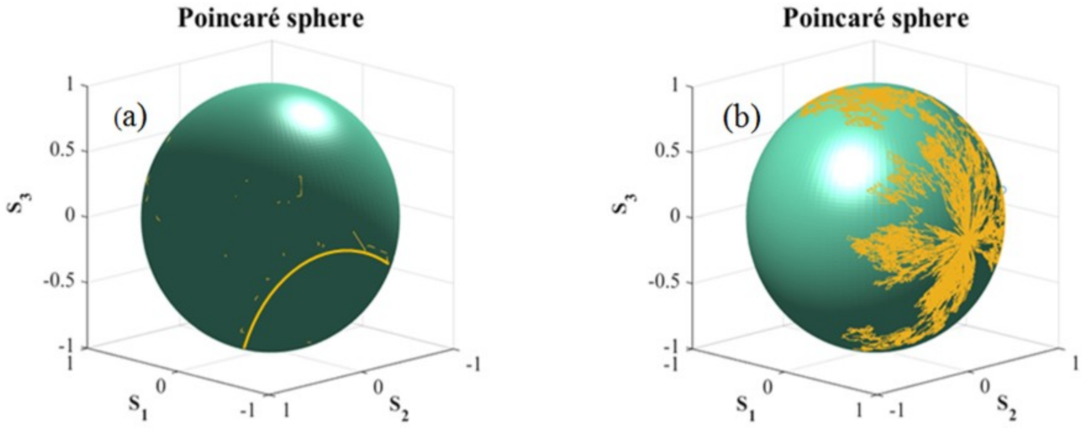

Fig. 3.7. Simulated states of polarization projected onto the Poincaré sphere. (a) Illustration of 1×10^3 samples and (b) 1×10^6 samples. The solid line in (a) shows the trajectory followed by consecutive simulated states of polarization.

The composite signal is then transmitted through a span of 300 km single-mode fiber with dispersion coefficient of 16.75 ps/nm.km and dispersion slope of 0.075 ps/nm^2.km. Both the channel wavelength and dispersion reference wavelength are set to 1550 nm.

Since the SOPs of both reference and signal are drifting and each has two independent orthogonal components, the output after photo-detection consists of four complex signals which are: $x_{11} = E_{rx}^{*}E_{sx} = I_{xx} + jQ_{xx}$, $x_{12} = E_{rx}^{*}E_{sy} = I_{xy} + jQ_{xy}$, $x_{21} = E_{ry}^{*}E_{sx} = I_{yx} + jQ_{yx}$ and $x_{22} = E_{ry}^{*}E_{sy} = I_{yy} + jQ_{yy}$. Subindices s and r denote signal and reference (LO), respectively, whereas x and y denote linear horizontal and linear vertical polarizations, respectively. The normalized magnitude of the complex signals x_{11} and x_{21} obtained before the diversity combiner are shown in Figs. 3.8(a) and 3.8(b) for samples 1 to 50×10^{3}.

In the case where both the signal and LO have linear horizontal polarizations, the output x_{11} of the proposed coherent receiver retrieves a normalized power magnitude around 0 dB, which turns to be larger than the detected power in any of the other outputs providing the polarization of the signal is maintained. Fig. 3.8(b) illustrates a drifting SOP of the LO that evolves from essentially linear horizontal to essentially linear vertical over the record. This drift would have caused a deep fade of the signal recovered by a single-port polarization diverse coherent optical receiver. A similar scenario is illustrated in Figs 3.8(c) and (d) for a LO states of polarization that evolves from essentially linear vertical to linear horizontal polarization between sample 5×10^{5} to sample 5.05×10^{5}. This amply demonstrates the capability of optical coherent receiver architecture proposed to recover the modulation successfully despite the use of both a signal and a LO with a drifting state of polarization. The observation is also valid for a signal in a vertical linear polarization state and a reference that drifts from horizontal (variable x_{12}) to vertical linear polarization (variable x_{22}). As explained in the preceding, the complex weights are found via an eigenvector–eigenvalue analysis of the covariance matrix performed by the

MRC algorithm. The product of the weights by the input signals shown in the traces of Figs. 8(e)–8(h) for samples 1 to 50×10^3 and 5×10^5 to 5.05×10^5. The plots illustrate how the MRC algorithm places greater weight on the signals with the greater SNR in order to generate a clean and steady combined output.

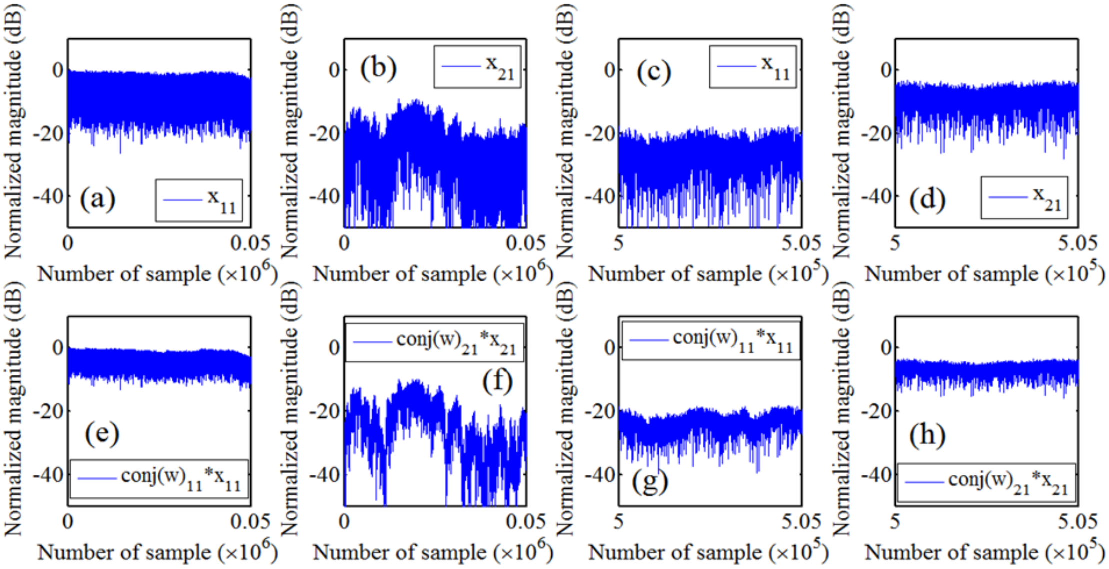

Fig. 3.8. (a)-(d) Normalized magnitude of the coherently detected signals $\boldsymbol{x_{11}}$ and $\boldsymbol{x_{21}}$ before the constrained MRC approach. (e)-(h) Normalized magnitude of the weighted signal.

The output of the diversity combiner for both constrained and unconstrained methods is shown in Figs. 3.9(a)–3.9(d) for 300 km fiber and the back-to-back system. As illustrated, the output signal fluctuates more when the fiber is used due to the impairments it causes. However, the output signal from the diversity combiner for constrained method is cleaner and steadier.

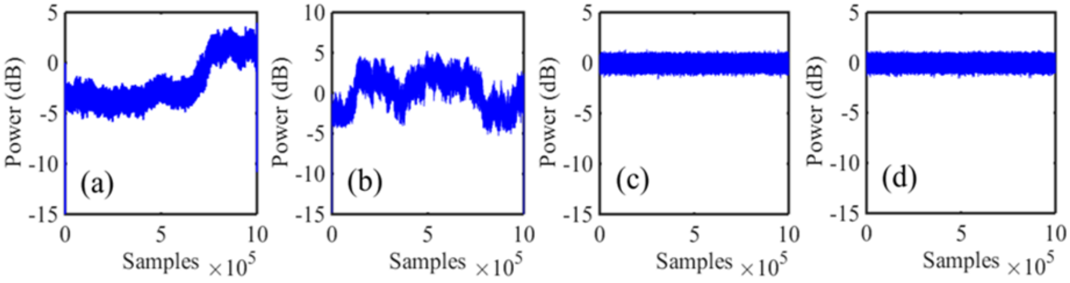

Fig. 3.9. Combined signal power from the MRC combiner without dispersion compensation using (a) constrained method and (b) unconstrained method for 300 km of dispersive single mode fiber. Signal powers in (c) and (d) are the counterparts of (a) and (b) for the back-to-back system.

In the demodulation subsystem, the combined signal vector is raised to the forth power to remove the DQPSK modulation, the unwrapped phase is found and divided by four to find the carrier phase. A first order autoregressive model is used to average the carrier phase over many samples to improve its estimation in the presence of noise. This estimated phase is equal to the expected carrier phase of the signal (modulation and noise are rejected) and is used to bring the signals into (carrier) phase synchrony. As DQPSK depends on the difference between two consecutive phases rather than the absolute phase value, it is the change of phase that encodes a symbol. Consequently, the output depends on the phase difference between the current and the previous symbol. Setting the phase rotation parameter to $\pi/4$ to simplify error detection, the constellation diagrams of the differentially detected demodulated signal after carrier phase drift elimination for 300 km fiber length are visualized in Figs. 3.10(a)–3.10(b) using both constrained and unconstrained methods. The performance of both algorithms is almost the same and an error-free demodulation constellation is obtained. However, the constrained method is slightly more robust especially when the fiber is longer, which means a received demodulated symbol has slightly larger probability to stand in the desired area of the constellation. On the other hand, the advantage of the constrained method is that the eigenvectors with largest eigenvalue of 2×2 matrices only need to be found which can be done analytically whereas in the unconstrained method the eigenvector with largest eigenvalue of a 4×4 matrix must be found which is best done numerically. Hence, the constrained method simplifies the process while the unconstrained method increases the complexity. As a reference, constellation diagrams found in the absence of chromatic dispersion and polarization mode dispersion are shown in Figs. 3.10(c) and 3.10(d). Comparing the traces in Figs. 3.10(a) and 3.10(b) with their counterparts in Figs. 3.10(c) and 3.10(d) illustrate that fiber dispersion causes a more scattered constellation diagram due to the dissimilar velocity of propagation of the spectral components associated with both signal and LO.

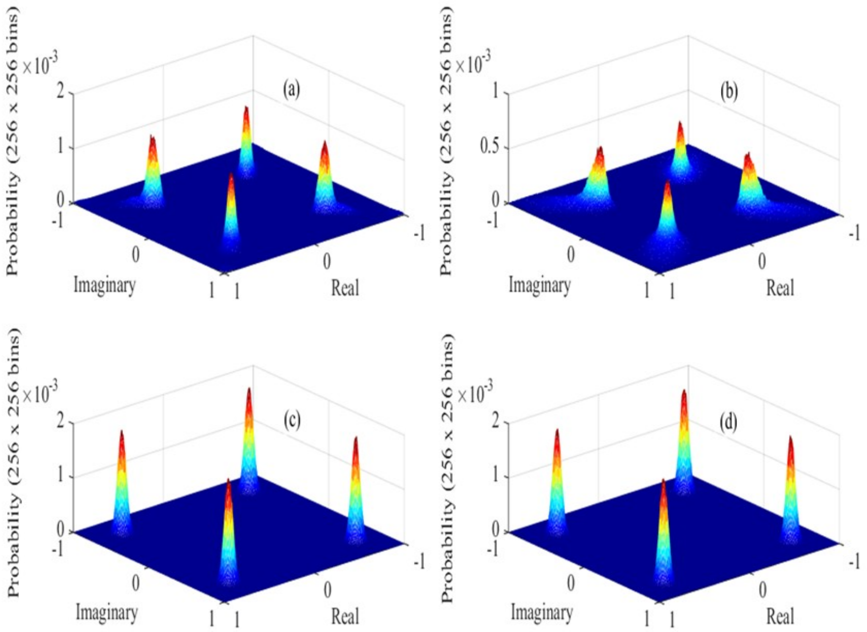

Fig. 3.10. Constellation of the demodulated signal using (a) constrained method and (b) unconstrained method without dispersion compensation for 300 km of dispersive single mode fiber. Constellations in (c) and (d) are the counterparts of (a) and (b) for the back-to-back system.

3.6 Discussions

The dual-port diversity approach in the proposed architecture opens up some opportunities for carrying modulation on both ports – this allows the multiplexing of three channels rather than the two polarization multiplexed channel of the single port diversity. Also, the polarization diversity of the reference permits a frequency standard distribution network to be used. The proposed architecture does increase the cost by about two times in terms of the optical front end and ADCs. However, there is an aggressive cost/price ‘learning curve’. Photonic integration means that there is little difference in the volume cost between the single and dual port circuits (packaging costs will dominate and be similar). The major cost is the DFB laser and the ADCs are currently integrated with the DSP in an ASIC. The DSP algorithms used these days are more sophisticated than the dual port polarization diversity – they effectively back propagate the received signal through the fiber undoing dispersion, evolution of polarization, and non-linearity to estimate the transmitted signal at the source. Therefore, the increased software complexity is marginal.

3.7 Conclusion

An improved yet original architecture of a coherent optical receiver based on two conventional coherent receiver front-ends in tandem has been proposed. It is demonstrated that the proposed architecture is effective at dealing with drifted states of polarization for both modulated signal and LO. An important subject in the proposed architecture is the polarization diversity approach, which is effectively implemented through the eigenvalue–eigenvector analysis of the covariance matrix. The concept is validated by numerical simulations considering two different methods of polarization diverse recovery with dispersion compensation, carrier phase estimation and elimination of sign ambiguity. As such, the simulations show the scheme when used at 100 Gbit/s is remarkably robust to extremely aggressive SOP changes. The results obtained are encouraging and motivate further research towards the actual design, fabrication, and testing of the proposed architecture which eventually may relax the polarization characteristics of laser sources operating as LOs in optical coherent receivers and brings new ideas for polarization multiplexing schemes in modern communication systems.

4 Chapter: Numerical analysis of a multi function photonic integrated circuit for coherent Radio-over-Fiber

4.1 Introduction

Resulting from the growing demand for high data rates in the wireless network, radio-over-fiber (RoF) systems integrated with optical coherent technologies are an emerging scheme for developing multi-Gbps wireless access [108-115]. Aided with digital signal processing techniques, combining microwave and fiber optic-based technologies also offers the possibility of mitigating system impairments, increasing transmission capacity, reducing energy consumption, and eventually reducing the cost of multi-Gb/s wireless access networks and operation [116-125]. Prior to its practical use, however, digital coherent RoF systems require optimized approaches to untangle some challenges. Considering the downlink, i.e. signal transport from the Central Office (CO) to the Remote Unit (RU), utilizing photonic means to generate mm-wave carriers (60 to 110 GHz) is a feasible approach to reduce the complexity of the RU. Laboratory demonstrations of RoF downlinks typically make use of the heterodyne mixing of a modulated laser source at λ_1 carrying the information signal and another uncorrelated-laser source at λ_2 [126]. Despite the relevant results reported therein, the number of laser sources used and their phase non-correlation are indicative of a promising improvement. Heterodyne mixing of two correlated wavelengths obtained by frequency multiplication in high-speed modulators for mm-wave carrier generation has also been reported [127-130]. The main drawback involves the requirement of filtering out one of the wavelengths to apply baseband modulation and the further combination of the two wavelengths for transport (the unmodulated and the modulated one, which hence requires optical amplification). Considering the uplink, i.e., signal transport from RU to CO, translating the (small power) intermediate-frequency electrical signal to the optical domain through an efficient single-sideband (SSB) modulator is a challenging issue. A common approach at the RU has been to down-convert the mm-wave to baseband using electrical mixers and low-pass filters. The baseband signal is then used to modulate the intensity of an optical carrier and sent to the CO [131]. Another approach utilizes an architecture comprising a customized 100 GHz traveling wave electro-absorption modulator (EAM) to modulate the amplitude of a distributed feedback (DFB) laser externally [126]. The electrical input to the up-conversion mixer is a 75-110 GHz carrier modulated with a 16 Gb/s quadrature phase shift keyed data signal. A combination of an optical circulator and a fiber-Bragg grating (FBG) is then used to extract the SSB; however, the low conversion efficiency reduces the receiver sensitivity. Moreover, the EAM, DFB laser, and FBG must be very closely matched in the frequency of operation, which entails temperature control of the up-converter; an undesirable feature in terms of energy consumption considerations. In addition to the advantages of SSB modulation in terms of dispersion-induced power fading, suppression of the optical carrier in the uplink SSB is essential to prevent dynamic range limitations of the coherent receiver sensitivity at the central office, especially if optical amplification is used to boost the weak sideband. Even though, the possibly remaining image sideband can be rejected by the coherent receiver, it could be a source of crosstalk in DWDM architectures.

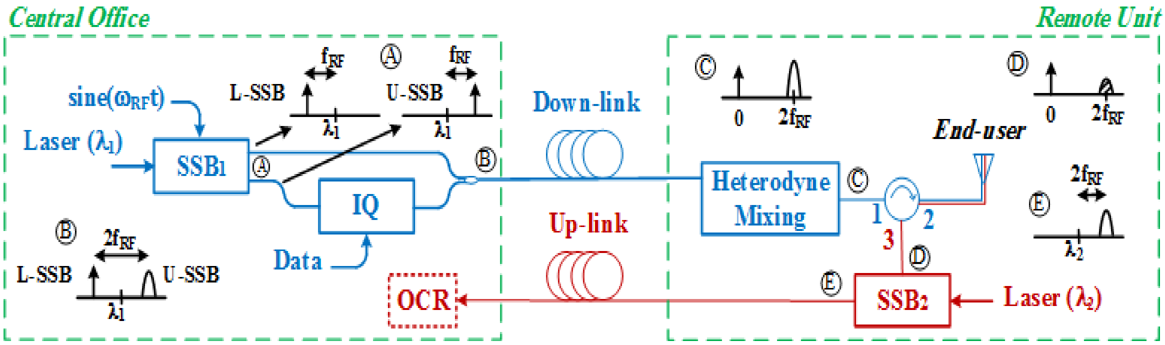

Fig. 4.1. diagram of a digital coherent RoF system comprising three main building blocks: SSB_1, IQ modulation at the downlink, and SSB_2 at the uplink. Insets A to E illustrate signals at relevant points of the system. Down and uplink are denoted in blue and red, respectively.

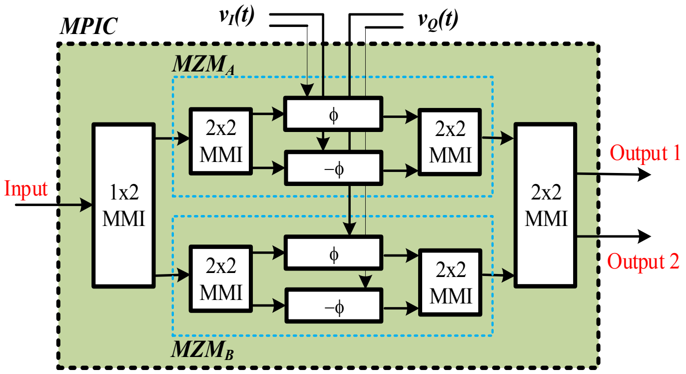

Fig. 4.2. Schematic diagram of the microwave photonic integrated circuit (unused ports of the 2×2 MMIs are not displayed).

Inspired by our former investigations on electro-optic up-conversion mixers [132], frequency 8-tupling and 24-tupling [133], as well as generalized architectures for frequency multiplication and translation for suppression of unwanted harmonics by design [134,135], the aim of the present work is to theoretically analyze the use of a microwave photonic integrated circuit (MPIC) in various building blocks of a digital coherent RoF system. The analyzed circuit offers the realization of in-phase and quadrature (IQ) modulation, as well as upper and lower-SSB at the downlink. In the latter function, the optical first-order harmonics (FOH) are spatially separated and available in distinct output ports of the MPIC, facilitating remote heterodyning. Moreover, the operation of the circuit is analyzed in the uplink as SSB modulator of mm-wave IQ-modulated carriers. The MPIC application in an RoF system is demonstrated by computer simulations using the Virtual Photonics Inc. software package. Simulation results show the analyzed circuit conveniently facilitates the generation of mm-wave IQ-modulated carriers at the remote unit by the heterodyne mixing of two correlated and spatially separated harmonics. In addition, the feasibility of the MPIC circuit to realize optical SSB at the uplink is shown provided that the electrical signal at the modulator input has a small power and is centered at the intermediate mm-wave frequency.

4.2 RoF system and MPIC architecture

A schematic diagram of the digital coherent RoF system analyzed here is shown in Fig. 4.1. Although conceptually similar to the typical architecture reported in [126], the downlink only requires a laser source at λ_1, which is frequency shifted by an electrical sinusoidal oscillator at the SSB_1 circuit (upper and lower sidebands in inset A). An identical replica of the MPIC is used afterwards as an IQ modulator for the baseband information signal. Both modulated and unmodulated single-sidebands are combined (inset B), transmitted through a fiber optic span, and heterodyne mixed at the remote unit. Comprised of a high-speed photo-detector, electrical amplifier, and band-pass filter, the heterodyne mixer delivers the IQ modulated signal centered at the mm-wave frequency of $2f_{RF}$ (inset C), which is eventually sent to the end user through a wireless link. The radio frequency (RF) signal transmitted from the RU to the CO is also centered at $2f_{RF}$ and, generally, reaches the SSB_2 with a significantly lower power (inset D) relative to the signal at the output of the heterodyne mixer (inset C). At the output of the SSB_2, the intermediate frequency signal is translated to a single-sideband at the frequency of $2f_{RF}$

from the emitting wavelength λ_2 of the laser source. After transmission through a fiber optic span, the optical SSB signal reaches the central office and is detected using an optical coherent receiver (OCR). The MPIC illustrated in Fig. 4.2 is comprised of four electro-optic phase modulators situated in the four arms between an interconnected 1×4 distribution tree and a complementary 4×2 combination tree [132]. Both the distribution and combination trees are formed by multi-mode interference (MMI) couplers. The circuit can be conceptually described as a pair of differential optical amplitude modulators within the arms of a Mach–Zehnder interferometer formed by the outer MMI splitter and coupler. The novelty of the MPIC lies in the use of the intrinsic phase relations between the MMI ports to realize a broadband and free of drift design requiring no static phase shift elements. For the MPIC to function as an IQ modulator, the upper and lower pair of phase modulators are driven differentially by the in-phase ($v_I(t)$) and quadrature ($v_Q(t)$) phase components of the modulating signal, respectively. For the SSB modulation, the RF electrical signal is applied to the I-channel and a $\pi/2$ phase-shifted replica of it to the Q channel.

4.3 Simulation results

The concept of the multi-function photonic integrated circuit is demonstrated by numerical simulations using the Virtual Photonics Inc. software package. Considering the MPIC circuit, the n×m MMIs are configured as splitters and couplers with 50% output power ratio and phase relations according to the self-imaging principle. Ideal phase modulators with unlimited frequency bandwidth are used. In all simulations, a resolution bandwidth of 19.5 MHz and span of 320 GHz are set to capture the optical and electrical spectra.

4.3.1 Downlink: single-sideband modulation

To analyze the MPIC operating as SSB at the downlink, a continuous wave DFB laser source set at a wavelength of 1553.59 nm with a linewidth of 200 kHz and power of 20 mW, is set as the optical input. A 30 GHz sinusoidal signal is deployed as the RF input to the SSB_1. The phase of the driving signal at the input of the phase modulators in MZM_A and MZM_B is 0, $+\pi$, $-\pi/2$, and $+\pi/2$, respectively. The amplitude of the driving RF signal is determined by the analysis of the first order harmonic (FOH) relative to the third-order (TOH) and higher-order harmonics at the output of the SSB_1. As shown in Fig. 3.3. (a), the FOH (i.e. the component of interest located 30 GHz above the optical carrier) increases linearly with the RF input signal from a low power level of around -50 dBm up to +20 dBm. Within the input power interval from +2 dBm to +19 dBm, the simulated harmonic suppression ratio (FOH/TOH) ranges from 56.5 dB to 22.8 dB. To maintain the FOH at a peak power of 1 mW while the TOH is kept minimal, a power of 7 dBm for a phase modulator load of 50 Ω is set to the driving RF input signal. The generated upper-SSB is shown in Fig. 4.3. (b).

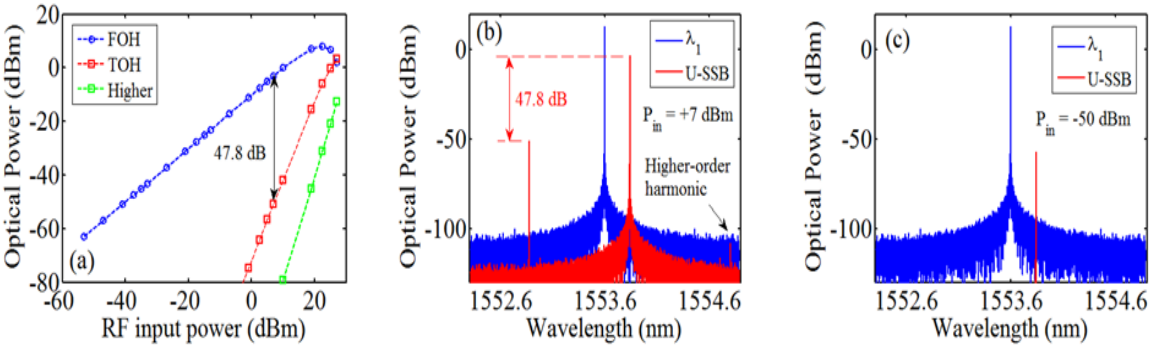

Fig. 4.3. (a) Optical power of the first-order component (30 GHz above laser source) and higher-order distortion (-90 GHz and +150 GHz off laser source) versus input signal power to the upper-SSB circuit. (b) Optical spectrum of the upper-SSB for an RF input power of +7 dBm, and (c) -50 dBm.

Although not illustrated, a lower-SSB harmonic with the same characteristics but located 30 GHz to the left of the optical carrier is generated in the other output port of the SSB$_1$ module. To further assess the performance of the single-sideband modulator, the upper and lower SSBs are combined and impinged onto a photo-detector whilst the continuous wave DFB laser source is set to different linewidths ranging from 1 kHz to 10 MHz. As shown in Fig. 4.4 (traces in blue), the spectral purity of the laser source has a negligible effect on the linewidth of the mm-wave carrier generated by heterodyne mixing, which is solely determined by the linewidth of the 30 GHz driving signal. In the counterpart, the heterodyne mixing of two distinct laser sources results in an RF carrier featuring a linewidth proportional to that of the two optical sources. Obtained output is shown in Fig. 4.4 with traces in red, green, purple and black, corresponding to separate lasers with linewidths of 1 kHz, 10 kHz, 100 kHz, 1 MHz and 10 MHz, respectively. Simulated results shown in Fig. 4.4 illustrate the advantage of the MPIC operating as SSB modulator at delivering two phase-correlated single-sidebands spatially separated in the two output ports of the analyzed photonic circuit.

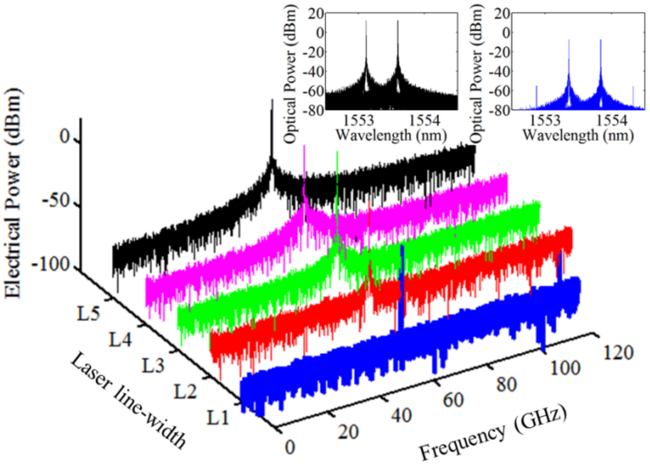

Fig. 4.4. The output of the photo-diode after impinging the two sidebands from the SSB circuit (blue trace) and two wavelengths from distinct lasers. L1 to L5 denote the case of laser linewidths of 10 MHz, 1MHz, 100kHz, 10 kHz, and, 1 kHz, respectively. Insets show the input to the photo-diode from distinct lasers (top left) and SSB circuit (top right) for laser sources set at a linewidth of 10 MHz.

4.3.2 Downlink: IQ-Modulation

To assess the performance of the MPIC operating as an IQ-modulator at the downlink, the FOH in Fig. 4.3. (b) is used as the optical input and is driven by a baseband 10 Gbps non-return-to-zero 2^{15}-1 pseudo random binary signal (PRBS). The input drive (V_{in} = $0.25V_{pp}$ = $0.5V_{\pi}$, with V_{π} being the half-way characteristic voltage of the differential modulator) is properly coded to comprise the I and Q channels. Placing a variable attenuator at the MPIC output, the symbol-error-ratio (SER) is simulated by an OCR for powers ranging from -30 dBm to -25 dBm and shown in Fig. 4.5. Simulation results illustrate that SER of 10^{-9} is achievable for the given optical and electrical inputs to the IQ-modulator providing a power above -27 dBm reaches the coherent receiver. The back-to-back quadrature phase-shift keying (QPKS) constellation diagrams obtained for received optical powers of -25 dBm and -30 dBm are shown in the insets of Fig. 4.5.

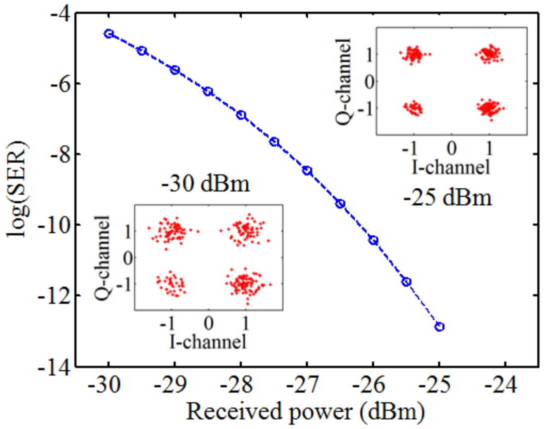

Fig. 4.5. Back-to-back SER simulated for the MPIC operating as an IQ-modulator.

4.3.3 Uplink: IQ-modulation

Once the upper-SSB is IQ-modulated and combined with the un-modulated lower-SSB, the composite signal shown in the inset of Fig. 4.6 is transmitted to the remote unit through a 5 km span of single-mode fiber. The attenuation, polarization mode dispersion coefficient, and non-linear refractive index of the fiber are set to 0.2 $\mathbf{dB/km}$, 0.158 $\mathbf{ps/\sqrt{m}}$ and 2.6×$\mathbf{10^{-20}}$ $\mathbf{m^2/W}$ respectively. The output of the heterodyne mixer comprises the source information signal frequency- shifted from its optical upper-SSB to the 60 GHz electrical carrier.

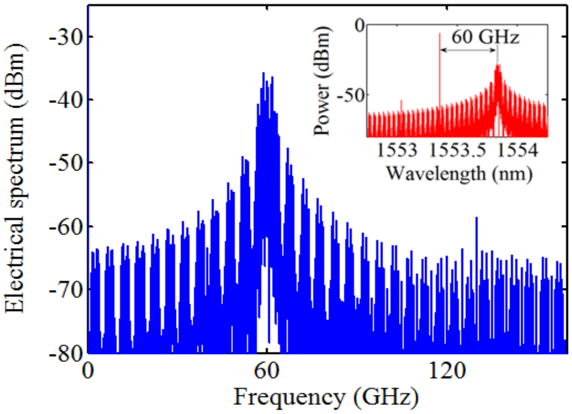

Fig. 4.6. Spectrum of the IQ-modulated information frequency-shifted to the mm-wave carrier at the output of the heterodyne mixer in the remote unit. Inset shows the incoming combined signal.

In principle, the mm-wave signal shown in Fig. 4.6 is amplified, band-pass filtered and transmitted to the end-user through a wireless link. Taking into account, the practical limitations imposed by the utilized software, an additive white Gaussian noise (AWGN) channel is used as a simple model of the wireless link. The QPSK-modulated carrier at 60 GHz and the AWGN channel are then connected to the RF input of the MPIC operating as an SSB_2 at the RoF uplink. A laser source with the same characteristics as used in the downlink centered at $\boldsymbol{\lambda_2}$ = 1545.6 nm is set as the optical carrier of this single-sideband modulator. Taking into account the mm-wave signal typically reaches the SSB_2 module at the RoF uplink with a low power prior to any electrical amplification [124,125,136], an attenuator is used to vary the input power whilst the SER is assessed by an OCR. As shown in Fig. 4.7, SER equal to $\mathbf{10^{-6}}$ is obtained in the simulations for RF input powers of -50 dBm, illustrating the feasibility of the proposed MPIC circuit as an IQ-modulator to an intermediate frequency signal (60 GHz in the analyzed scenario) with low average power. Optical spectrum at the output of the SSB_2 (i.e. the input of the optical coherent receiver used to assess the performance of the MPIC) and associated constellation is illustrated in the insets of Fig. 4.7. Moreover, considering the RF signal with a power of -50 dBm at the output of the heterodyne mixer, the error-vector magnitude (EVM) of the received signal at the central office is simulated and shown in Fig. 4.8 for SNR ranging from 8 to 18 dB (60 GHz modulated signal to AWGN level). Simulations of the entire coherent RoF system indicate that transmission compliant to the IEEE standard is achievable using single-mode fibers spanning up to 10 km [137].

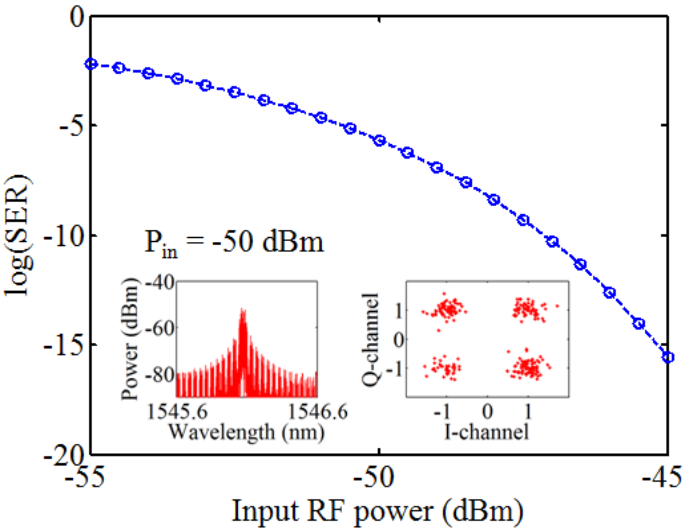

Fig. 4.7. Simulated SER for the MPIC operating as IQ-modulator at 60 GHz frequency-shifted signal in the optical coherent RoF uplink. Insets show the spectrum of the signal reaching the coherent receiver and the corresponding received constellation.

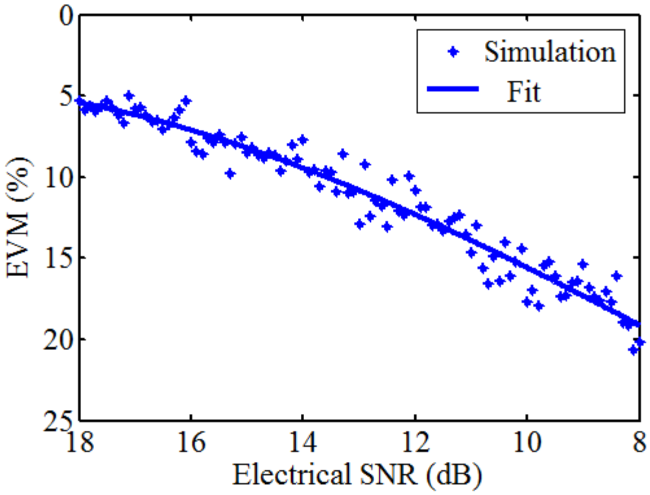

Fig. 4.8. Simulated EVM for the RoF system transmitting QPSK (single carrier) modulated data versus wireless channel SNR using 5 km single- mode fiber. Solid line denotes a fit to a logarithmic function of the EVM.

To further assess the performance of the proposed MPIC in an RoF system, orthogonal frequency division multiplexing (OFDM) technique has been used to generate the source data for the IQ modulator in the downlink. Indeed, OFDM has been employed in many wireless communication standards owing to its high spectral efficiency [138-141]. In the analyzed RoF system, the available spectrum is divided into N=128 sub-carriers, each one modulated using QPSK at 5 Gbaud. A schematic diagram of the OFDM modulator at the transmitter side and demodulator at the receiver side are shown in Fig. 4.9.

The serial-to-parallel converter takes the serial stream of 10 Gbps data and outputs 128 parallel streams. These parallel streams are independently converted into the QPSK digital modulation format and then superimposed onto the orthogonal subcarriers for transmission, which are represented by IFFT on the transmitter side. The outputs of the 128 parallel arms are summed up together to generate the OFDM signal. In addition to the IFFT block, some OFDM systems also incorporate a cyclic prefix allowing for simple implementation of an equalizer in the frequency domain to provide improved link performance in multipath environments (e.g. wireless communication).

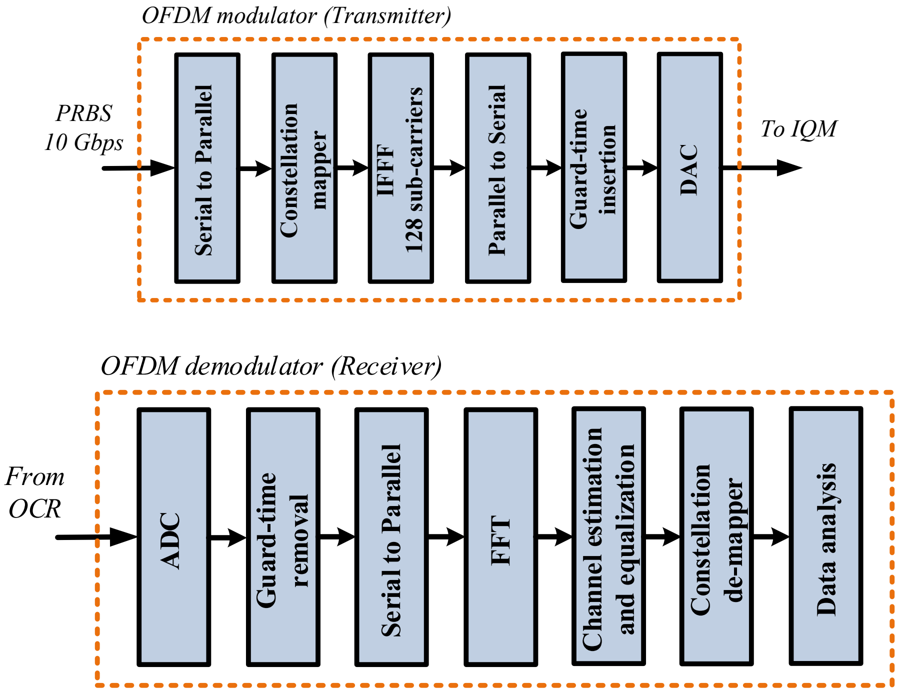

Fig. 4.9. Architecture of the OFDM system used to further assess the performance of the proposed MPIC in the RoF system. IFFT: inverse fast Fourier transform; DAC: digital to analog converter; ADC: analog to digital converter; IQM: IQ-modulator; FFT: fast Fourier transform.

Having used an AWGN channel, a frequency domain equalizer commonly utilized for a multipath fading channel is not required in the OFDM receiver. After the OFDM signal is generated and supplied to the MPIC operating as an IQ-modulator at the central office, the composite signal passes through 5 km of single-mode fiber and reaches the heterodyne mixer and the SSB_2 modulator. Maintaining the power of -50 dBm at the input of the MPIC functioning as an SSB in the uplink, the received signal is detected by OFDM demodulator. Here, the guard period is removed and the FFT of each OFDM symbol is computed to find the original transmitted spectrum. The phase angle of each subcarrier is then assessed and converted back to the data stream by demodulating the received phase. Delay compensation is applied to synchronize the received signal. In addition to the OFDM with QPSK carriers, an OFDM system for 16QAM modulation format is simulated. The QPSK-OFDM and 16QAM-OFDM system performance are evaluated by measuring the EVM of the received signal at the central office for SNR ranging from 8 to 18 dB (60 GHz modulated signal to AWGN level) using 5 km single-mode fiber. It should be noted that the results comply with the IEEE Standard [140], however, for deploying fiber length longer than 5 km, the SSB_1 input RF power needs to be increased in order to achieve the standard EVM. As illustrated in Fig. 4.10, higher-order modulation formats require a larger SNR to minimize the EVM.

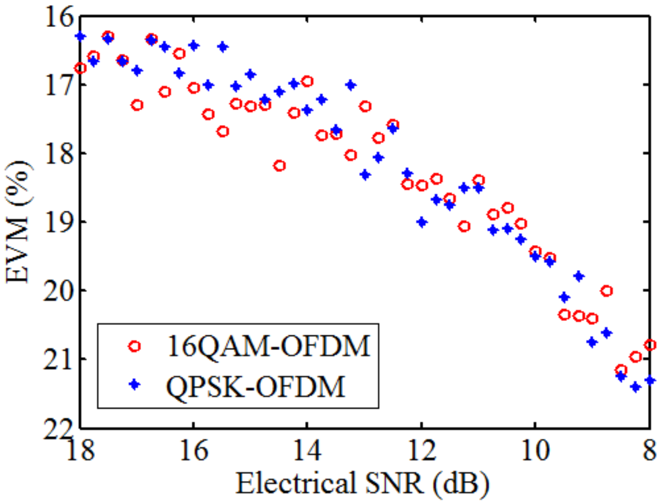

Fig. 4.10. Simulated EVM for the RoF system versus wireless channel SNR for OFDM signal transmission using 5 km single-mode fiber. Solid line denotes a fit to a logarithmic function of the EVM.

4.4 Conclusion

The performance of a microwave photonic integrated circuit has been analyzed as the main building block of an optical coherent RoF link. Results illustrate the benefits of using the MPIC as SSB modulator at the downlink due to the fact that the lower and upper sidebands are obtained physically in distinct ports of the circuit, facilitating the modulation of one output without the need of an optical filter. Simulation results also illustrate the use of the MPIC as an IQ modulator of either a baseband or an intermediate frequency (60 GHz) modulated signal. Simulation results of the latter, confirm the feasibility of the circuit used as an SSB modulator with low-power input signals, relaxing the requirements of high-power RF amplifiers to boost the 60 GHz modulating carrier upcoming from the wireless link. The performance of the analyzed circuit has been further assessed by simulating OFDM signals with the half-rate coding in the complete digital coherent RoF system. Finally, EVM estimations for a 128-subcarrier OFDM system using QPSK and 16QAM modulation formats have been presented.

5 Chapter: Tracking channel alignment in blind polarization demultiplexing

5.1 Introduction

Digital coherent optical receivers have enabled the practical implementation of advanced modulation formats such as quadrature phase shift keying (QPSK) and quadrature amplitude modulation (QAM) owing to their capability to measure the field amplitude and phase. Advanced modulation formats together with digital signal processing (DSP) enhanced coherent receivers is consequently an effective approach to the attainment of high spectral efficiency in modern high-capacity fiber-optic transmission systems. Polarization multiplexing can also be applied to further increase the spectral efficiency. Accurate demodulation of the signal can be achieved providing the coherent receiver tracks and compensates the drift of the relative state of polarization (SOP) and phase between signal and local oscillator fields [142,143]. Real-time DSP algorithms have been developed that enable the optical receiver to perform polarization de-multiplexing, carrier phase estimation, dispersion compensation, data recovery and more [144-150].

DSP techniques for de-multiplexing data from mixed polarizations can be categorized into two classes [151-156]. The first class comprises adaptive equalizers that require a training sequence to be transmitted, which consumes extra bandwidth [157], in order to adjust the equalizer weights. The second class operates blindly and comprises the constant modulus algorithm (CMA) and independent component analysis (ICA) [158,159]. The blind methods are preferable since they estimate the signals generated by the sources directly from the observed mixture and, more importantly, they do not compromise the spectral efficiency. The CMA algorithm changes its coefficients adaptively to minimize the fluctuation of the modulus of the separated signals. CMA has the virtue that it is simple to implement but its performance depends on its initial state and a step size parameter that should be accurately selected [160-162]. Moreover, CMA suffers poor convergence when two ports attempt to output the same source. This problem may be overcome in the special case of polarization de-multiplexing by enforcing the weight matrix found by CMA to be unitary [163].

ICA has been widely applied to instantaneous mixtures [164-168]. In comparison to CMA, an ICA-based method provides similar polarization tracking capability but can outperform CMA in convergence rate [169,170]. Successful de-multiplexing of both QPSK and 16-QAM has been demonstrated using a tensor-based ICA algorithm [171]. While a method may successfully de-multiplex a mixture of distinct sources, if the method is blind, there is no information to decide on the particular port which should be associated to each source. The blind methods therefore construct a recovery matrix that is unique only up to a product of a permutation matrix and a diagonal matrix of phase factors, i.e. there is an inherent ambiguity of which source signal emerges from a port and its phase relative to other ports. Some papers have proposed phase and permutation ambiguity elimination through semi-blind equalization [172,173]. For instance, the weight matrix may be found using an objective function that combines both training and higher order statistical information [167,174]. However, the use of training sequences inevitably compromises the spectral efficiency.

In order to address the inherent ambiguity of blind demultiplexing algorithms such as ICA/CMA, this chapter describes a method of maintaining the initial channel alignment and phase in the coherent optical receiver. The proposed method aims to enhance the performance of the digital coherent optical receiver by setting the diversity combiner weight matrix to a member of the equivalence class of the estimated recovery matrix that is the nearest to the previous weight matrix. To the best of the authors' knowledge, tracking channel alignment by a projection method has not been previously proposed in the context of blind source separation for the coherent optical receivers. The method is verified by simulation of the de-multiplexing by ICA and by an experiment involving the de-multiplexing by CMA of dual-polarization differential QPSK coherent optical sources mixed by propagation through an optical fiber subject to random perturbations in birefringence.

The chapter is organized as follows. The system model is explained in section 5.2. The proposed method including the mathematics of the equivalence class projection technique is addressed in section 5.3. Simulation results are reported in section 5.4 and experimental results are reported in section 5.5. The performance of the method under different conditions is discussed in section 5.6. The chapter closes with a summary and conclusions in section 5.7.

5.2 General formulation of the system

In a polarization diverse coherent receiver [175], as shown schematically in Fig. 5.1, the signal and reference must first be decomposed into orthogonal polarized components, for example, representing the transverse electric (TE) and transverse magnetic (TM) polarizations. Two 90° optical hybrids then combine the co-polarized signal and reference components. The in-phase and quadrature signals provided by the balanced photo-receivers at the outputs of the hybrids yield the two complex beat signal components. The signal model can be succinctly written as:

$$\boldsymbol{y} = \boldsymbol{U}\boldsymbol{x} \qquad \text{Equation 5.1}$$

where x is a complex vector with components representing the two signal sources, $\boldsymbol{y}$ a complex vector with components representing the two observed mixed signal components, and $\boldsymbol{U}$ is a unitary mixing matrix that satisfies:

$$\boldsymbol{U}^{\dagger}\boldsymbol{U} = \boldsymbol{I} \qquad \text{Equation 5.2}$$

This signal model motivates using ICA/CMA as a method of source estimation.

5.3 Concept of Independent Component Analysis (ICA) and the constant modulus algorithm (CMA)

Independent component analysis (ICA) is a method of blind source separation for separating complex signals mixed by an invertible operator or matrix in the linear case. The mixing matrix is unknown and no information on the sources is required other than their statistical independence and no more than one source being Gaussian distributed. The ICA method constructs a recovery matrix $\boldsymbol{V}$ that is an estimate of the inverse of the mixing matrix, merely from the mixed signal. This may be achieved by maximizing a contrast function that is a measure of the statistical independence of the estimated sources [176]. Note that subject to the validity of the central limit theorem, a mixture of independent signals generally approaches a normal distribution statistically irrespective of the distribution of each signal. The high-order cumulants of a perfect Gaussian signal are zero. This motivates the definition of the contrast function as the summation of the squares of the fourth-order marginal cumulants extended to complex random variables [177] and its application has met with considerable success [158]. In the case of polarization de-multiplexing, the problem simplifies considerably as there are only two sources. The recovery matrix is unitary and may be found analytically from the fourth order cumulants of the in-phase and quadrature signals provided by balanced photo-receivers at the outputs of the hybrid. The Constant Modulus Algorithm (CMA) [178] is another popular de-multiplexing scheme in two-dimensional data communication systems. CMA estimates an unknown system using the output signal via a stochastic gradient of the cost function with respect to the tap weights vector. Basically, the convergence and speed of the CMA algorithm depends on the choice of the initial matrix and the step size [160]. Nevertheless, it suffers from the convergence to the same source problem [179] as CMA adjusts the FIR filters in both channels independently. This problem may be overcome in the special case of polarization de-multiplexing by enforcing the weight matrix found by CMA to be unitary [163]. In the following, the proposed method to improve the performance of blind estimation algorithms in polarization de-multiplexing are discussed.

5.4 Tracking channel alignment

A recovery matrix $\boldsymbol{V}$ estimated by ICA/CMA is applied to the data $\boldsymbol{y}$ to recover the signals $\widetilde{\boldsymbol{x}}$ with minimal cross-talk:

$$\widetilde{\boldsymbol{x}} = \boldsymbol{V}\boldsymbol{y} = \boldsymbol{V}\boldsymbol{U}\boldsymbol{x} \approx \boldsymbol{x} \qquad \text{Equation 5.3}$$

Ideally, the recovery matrix is the inverse of the mixing matrix $\boldsymbol{V} = \boldsymbol{U}^{\dagger}$. However, necessarily any blind recovery cannot uniquely assign to a particular source a unique phase and output port. So, $\boldsymbol{V}$ is at best $\boldsymbol{V} = \boldsymbol{D}\boldsymbol{P}\boldsymbol{U}^{\dagger}$, where $\boldsymbol{D}$ is a diagonal phase factor matrix and $\boldsymbol{P}$ is a permutation.

The channel alignment method proposed is as follows: a matrix $\boldsymbol{W}$ is introduced that is set to the initial estimate $\boldsymbol{W} = \boldsymbol{V}_{\boldsymbol{0}}$ at the beginning of the tracking interval and updated according to the rule:

$$\boldsymbol{W} \longleftarrow \mathbb{P}(\boldsymbol{W};\boldsymbol{V}) \qquad \textit{Equation 5.4}$$

where $\boldsymbol{V}$ is the current estimated recovery matrix and $\mathbb{P}(\boldsymbol{W};\boldsymbol{V})$ is a projection (i.e. an idempotent operator) that finds the closest representative to the current weight matrix $\boldsymbol{W}$ in the ambiguity class $\{\boldsymbol{DPV} | \boldsymbol{D} \in \mathcal{D}; \boldsymbol{P} \in \mathcal{P}\}\}$ where $\mathcal{D}$ is the set of all diagonal phase factor matrices and $\mathcal{P}$ is the set of all permutation matrices. Thus, the updated $\boldsymbol{W}$ will not follow changes of $\boldsymbol{V}$ due to its motion within an ambiguity class but will track changes due to its motion across ambiguity classes. To construct this projection operator, it is necessary to give meaning to 'closest' by introducing an ambiguity invariant metric.

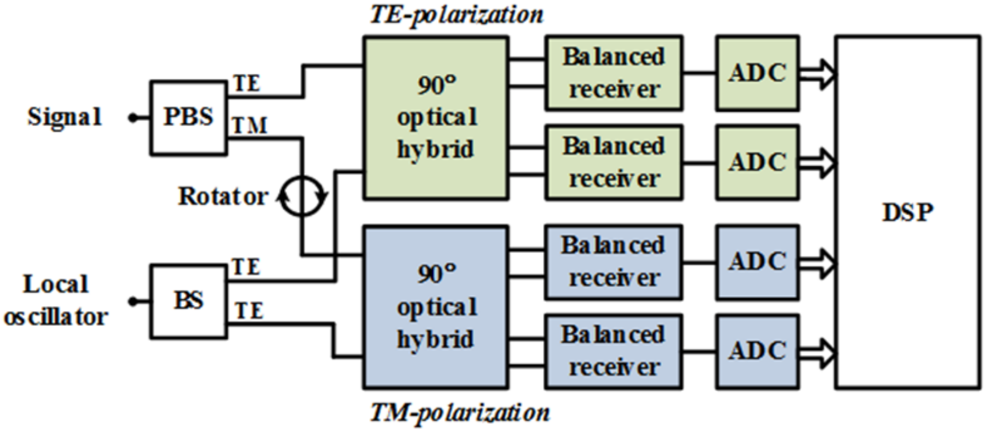

Fig. 5. 1. Schematic diagram of a polarization diverse coherent receiver. Polarization diversity refers to the input signal. TE (horizontal) and TM (vertical) polarization components are illustrated in green and blue, respectively [175].

5.4.1 Ambiguity invariant metric

The blind de-multiplexer constructs a unitary recovery matrix $\boldsymbol{V}$ up to a product of a diagonal phase factor matrix $\boldsymbol{D}$ and a permutation $\boldsymbol{P}$. If the overall phase of $\boldsymbol{V}$ is adjusted so that $\det(\boldsymbol{V}) = 1$ then $\boldsymbol{V} \in \mathrm{SU(n)}$. The problem of keeping track of the ambiguity may then be cast entirely within the setting of the special unitary group in n dimension $\mathrm{SU(n)}$.

Two matrices $\boldsymbol{A}, \boldsymbol{B} \in \mathrm{SU(n)}$ are related $\boldsymbol{A} \sim \boldsymbol{B}$ by this ambiguity if there exists a $\boldsymbol{D} \in \mathcal{D} \subset \mathrm{SU(n)}$ and $\boldsymbol{P} \in \mathcal{P} \subset \mathrm{SU(n)}$ such that $\boldsymbol{A} = \boldsymbol{DPB}$ where $\mathcal{D}$ is the sub-group of all diagonal special unitary matrices with uni-modular elements, and $\mathcal{P}$ is the real sub-group of all permutations. It follows from the fact that the result of conjugation of an element of $\mathcal{D}$ by an element of $\mathcal{P}$ is an element of $\mathcal{D}$ that this relation is an equivalence relation. This equivalence relation partitions the special unitary group into a collection of equivalence classes. Each equivalence class may be represented by any one of its members. It is therefore useful to define a metric that measures the distance between any pair of equivalence classes. Or, equivalently, a metric ρ which measures the distance between two representative matrices $\boldsymbol{A}$ and $\boldsymbol{B}$ that is invariant to the ambiguity:

$$\rho(\boldsymbol{D_1 P_1 A}, \boldsymbol{D_2 P_2 B}) = \rho(\boldsymbol{A}, \boldsymbol{B}) \ \forall \ \boldsymbol{D_1}, \boldsymbol{D_2} \in \mathcal{D} \ ; \ \boldsymbol{P_1}, \boldsymbol{P_2} \in \mathcal{P} \qquad \textit{Equation 5.5}$$

Consider the Frobenius inner product of two matrices $\boldsymbol{A}, \boldsymbol{B} \in \mathbb{C}^{n \times n}$:

$$(\boldsymbol{A}, \boldsymbol{B}) = \frac{1}{n} Tr(\boldsymbol{A}\boldsymbol{B}^{\dagger}) = \frac{1}{n} \sum_{j,k=1,n} a_{jk} b_{jk}^{*} \qquad \textit{Equation 5.6}$$

The induced norm $\|\boldsymbol{A}\| = \sqrt{(\boldsymbol{A}, \boldsymbol{A})}$ defines a metric ρ_F that measures the squared distance between two matrices:

$$\rho_F(\boldsymbol{A}, \boldsymbol{B}) = \|\boldsymbol{A} - \boldsymbol{B}\|^2 \qquad \textit{Equation 5.7}$$

Accordingly, a metric ρ_D invariant to the action of elements of $\mathcal{D}$ may be defined by:

$$\rho_D = \min_{\boldsymbol{D} \in \mathcal{D}} \rho_F(\boldsymbol{A}, \boldsymbol{DB}) \qquad \textit{Equation 5.8}$$

Every element $\mathrm{D} \in \mathcal{D}$ may be parameterized by:

$$\boldsymbol{D} = \mathrm{diag}\{\exp(i\theta_j)\} \qquad \textit{Equation 5.9}$$

The set of angles $\vartheta = \{\theta_j | \sum_j \theta_j = 0\}$ forms a co-ordinate system on $\mathcal{D}$ which thereby has the structure of a n-dimensional torus (i.e. the Cartesian product of n circles). Let a_m, b_m denote the mth row of $\boldsymbol{A}$, $\boldsymbol{B}$ respectively. Then:

$$\rho_F(\boldsymbol{A}, \boldsymbol{D}(\vartheta)\boldsymbol{B}) = (\boldsymbol{A} - \boldsymbol{D}(\vartheta)\boldsymbol{B}, \boldsymbol{A} - \boldsymbol{D}(\vartheta)\boldsymbol{B}\ ) = \sum_{m=1,n} \left(\boldsymbol{a}_m - e^{i\theta_m}\boldsymbol{b}_m, \boldsymbol{a}_m - e^{i\theta_m}\boldsymbol{b}_m,\right) \quad \textit{Equation 4.10}$$

Expanding the right hand side and substituting $(a_m, b_m) = |(a_m, b_m)| \exp\{i\, arg[(a_m, b_m)]\}$ yields:

$$\rho_F(\boldsymbol{A}, \boldsymbol{D}(\vartheta)\boldsymbol{B}) = (\boldsymbol{A}, \boldsymbol{A}) + (\boldsymbol{B}, \boldsymbol{B}) - 2 \sum_{j=1,n} \left|(\boldsymbol{a}_j, \boldsymbol{b}_j)\right| \cos\left(\theta_j - \arg\left((\boldsymbol{a}_m, \boldsymbol{b}_m)\right)\right) \qquad \textit{Equation 5.11}$$

This expression is minimized by the choice $\theta_m = \arg[(a_m, b_m)]$ or, equivalently $D = \mathrm{diag}\left\{\frac{(a_m, b_m)}{|(a_m, b_m)|}\right\}$. So:

$$\rho_D(\boldsymbol{A},\boldsymbol{B}) = (\boldsymbol{A},\boldsymbol{A}) + (\boldsymbol{B},\boldsymbol{B}) - 2\sum_{m=1,n} |(\boldsymbol{a}_m, \boldsymbol{b}_m)| \qquad \text{Equation 5.12}$$

Following a similar prescription, a metric ρ invariant to the action of both elements of $\mathcal{D}$ and $\mathcal{P}$ may be defined by:

$$\rho(\boldsymbol{A},\boldsymbol{B}) = \min_{P\in\mathcal{P}} \rho_D(\boldsymbol{A},\boldsymbol{PB}). \qquad \text{Equation 5.13}$$

Regrettably, the permutations form a discrete subgroup of `SU(n)` and there is no alternative but to evaluate the right hand side for every possible permutation. Fortunately for the case at hand of two dimensions only the identity and the exchange permutations need to be considered.

5.4.2 Projection onto the nearest equivalent of a representative of the equivalence class

A closely related problem is: given a target matrix $\boldsymbol{A}$ and a representative matrix $\boldsymbol{B}$ of the equivalence class $\mathcal{B} = \{\boldsymbol{QB} |\ \boldsymbol{Q} = \boldsymbol{DP} \in \mathcal{Q}\}$ find the element $\boldsymbol{B}_* \in \mathcal{B}$ nearest to $\boldsymbol{A}$. That is:

$$\boldsymbol{B}_* = \arg\{\min_{Q\in\mathcal{Q}} \rho_F\ (\boldsymbol{A},\boldsymbol{QB})\}\boldsymbol{B} \qquad \text{Equation 5.14}$$

Since $\mathcal{P}$ is discrete, it is necessary to first find $\mathbb{D}(\boldsymbol{P}) = \arg\{\min_{D\in\mathcal{D}} \rho_F(\boldsymbol{A},\boldsymbol{DPB})\}$ for every $\boldsymbol{P} \in \mathcal{P}$ and then perform the search:

$$\boldsymbol{P}_* = \arg\{\min_{\boldsymbol{P}\in\mathcal{P}} \rho_F(\boldsymbol{A},\mathbb{D}(\boldsymbol{P})\boldsymbol{PB})\} \qquad \text{Equation 5.15}$$

and finally set:

$$\boldsymbol{B}_* = \mathbb{D}(\boldsymbol{P}_*)\boldsymbol{P}_*\boldsymbol{B} \qquad \text{Equation 5.16}$$

From the preceding section $\rho_D(\boldsymbol{A},\boldsymbol{C}) = (\boldsymbol{A},\boldsymbol{A}) + (\boldsymbol{B},\boldsymbol{B}) - 2\sum_{m=1,n} |(a_m, c_m)|$ and $\mathbb{D}(\boldsymbol{P}) = \mathrm{diag}\left\{\frac{(a_m,c_m)}{|(a_m,c_m)|}\right\}$, where c_m is the mth row of $\boldsymbol{C} = \boldsymbol{PB}$. Hence,

$$\boldsymbol{P}_* = \arg\{\max_{\boldsymbol{P}\in\mathcal{P}}[\sum_{m=1,n} |(a_m, c_m)|]\} \qquad \text{Equation 5.17}$$

The assignment:

$$\mathbb{P}(\boldsymbol{A};\boldsymbol{B}) = \mathbb{D}(\boldsymbol{P}_*)\boldsymbol{P}_*\boldsymbol{B} \qquad \text{Equation 5.18}$$

projects matrix $\boldsymbol{B}$ to the nearest member of its equivalence class to a target matrix $\boldsymbol{A}$.projection is nonlinear due to the implicit dependence of $\boldsymbol{P}_*$ on both $\boldsymbol{A}$ and $\boldsymbol{B}$.

The distance has been measured using a metric appropriate to the ‘flat’ space $\mathbb{C}^{\mathrm{n}\times\mathrm{n}}$. However, $\boldsymbol{A},\boldsymbol{B}$ belong to $\mathrm{SU(n)}$ which is a curved space. The distance between two points on the group manifold is then be better defined in terms of the length of the geodesic that joins them [127,180]. In the application herein the chord distance serves equally well.

5.4.3 Special case of SU(2)

In the case of polarization de-multiplexing, there are only two sources. The lower dimensional setting of $\mathrm{SU}(2)$ simplifies the visualisation of the ambiguity tracking algorithm which aids intuition. Let $\{\sigma_q \in \mathbb{C}^{2\times 2} | q = 1,2,3,4\}$ be a basis that is orthonormal with respect to the Frobenius inner product:

$$(\boldsymbol{\sigma}_q, \boldsymbol{\sigma}_k) = \delta_{qk}$$

Equation 5.19

where $\boldsymbol{\delta}_{qk}$ is the Kronecker delta. Denoting j as the complex number $\sqrt{-1}$, it is convenient to choose the Pauli spin matrices:

$$\boldsymbol{\sigma}_0 = \begin{bmatrix} 1 & 0 \\ 0 & 1 \end{bmatrix} \quad \boldsymbol{\sigma}_1 = \begin{bmatrix} 0 & 1 \\ 1 & 0 \end{bmatrix}$$
$$\boldsymbol{\sigma}_2 = \begin{bmatrix} 0 & -\mathrm{j} \\ \mathrm{j} & 0 \end{bmatrix} \quad \boldsymbol{\sigma}_3 = \begin{bmatrix} 1 & 0 \\ 0 & -1 \end{bmatrix}$$

Equation 5.20

Since every member of $\mathrm{SU}(2)$ is of the form of $\boldsymbol{U} = \begin{bmatrix} a & b \\ -b^* & a^* \end{bmatrix}$ and $|a|^2 + |b|^2 = 1$, then:

$$\boldsymbol{U} = c_0\boldsymbol{\sigma}_0 + jc_1\boldsymbol{\sigma}_1 + jc_2\boldsymbol{\sigma}_2 + jc_3\boldsymbol{\sigma}_3$$

Equation 5.21

where the co-ordinates c_q are real and satisfy $\sum_{q=1,4} c_q^2 = 1$ evincing the homeomorphism between the $\mathrm{SU}(2)$ manifold and S^3. Consider the path on $\mathrm{SU}(2)$ defined by:

$$\begin{matrix} \boldsymbol{U}(t) = exp(jt\boldsymbol{H})\,\boldsymbol{B} \\ \boldsymbol{H} = -j\,ln(\boldsymbol{A}\boldsymbol{B}^{\dagger}) \end{matrix} \quad t \in [0,1]$$

Equation 5.22

where $\boldsymbol{H} \in \mathrm{su}(2)$ the Lie algebra of traceless Hermitian matrices in two dimensions. By construction $\boldsymbol{U}(0) = \boldsymbol{B}$, and $\boldsymbol{U}(1) = \boldsymbol{A}$, and the tangent vector at every point on the path is the constant matrix $\boldsymbol{H}$. Exceptionally, for $\mathrm{SU}(2)$ one may write:

$$\begin{aligned} \exp(j\boldsymbol{H}) &= \cos(h)\,\boldsymbol{\sigma}_0 + j\sin(h)\,\frac{1}{h}\boldsymbol{H} \\ h &= -\,det(\boldsymbol{H}) \end{aligned} \qquad \textit{Equation 5.23}$$

and hence the geodesic distance on $\mathrm{SU}(2)$ between any two elements $\boldsymbol{A}, \boldsymbol{B}$ may be taken as:

$$\rho_G(\boldsymbol{A}, \boldsymbol{B}) = h = -\,det(\boldsymbol{H}) = det(ln(\boldsymbol{B}\boldsymbol{A}^{\dagger})) \qquad \textit{Equation 5.24}$$

Note that h has an ambiguity corresponding to the addition of a multiple of 2π corresponding to multiple cycles in either direction around the geodesic. The squared Frobenius distance is:

$$\rho_F(\boldsymbol{A}, \boldsymbol{B}) = \left[2\sin\left(\frac{1}{2}h\right)\right]^2 \qquad \textit{Equation 5.25}$$

which may therefore be identified as the chord length corresponding to the arc length h as illustrated in Fig. 5.2. (a). The Frobenius metric is therefore an adequate measure of 'closeness' on $\mathrm{SU}(2)$ and moreover resolves the ambiguity of the geodesic measure.

In the two dimensional case there are only two permutations:

$$\boldsymbol{P} = \begin{cases} \boldsymbol{\sigma}_0 \\ \boldsymbol{\sigma}_1 \end{cases} \qquad \textit{Equation 5.26}$$

and for $\mathrm{SU}(2)$ recovery matrices the relative phase ambiguity is a continuous one parameter sub-group:

$$\begin{aligned} \boldsymbol{D}(\theta) &= \begin{bmatrix} \exp(j\theta) & 0 \\ 0 & \exp(-j\theta) \end{bmatrix} \\ &= \cos(\theta)\,\boldsymbol{\sigma}_0 + j\sin(\theta)\,\boldsymbol{\sigma}_3 \end{aligned} \qquad \textit{Equation 5.27}$$

Hence, the ambiguity is described by two disjoint continuous one-parameter sub-groups:

$$\begin{aligned}\boldsymbol{\sigma}_{I}(\theta) &= \cos(\theta)\,\boldsymbol{\sigma}_0 + j\sin(\theta)\,\boldsymbol{\sigma}_3\\ \boldsymbol{\sigma}_{II}(\varphi) &= \cos(\varphi)\,\boldsymbol{\sigma}_1 + \sin(\varphi)\,\boldsymbol{\sigma}_2\end{aligned} \qquad \textit{Equation 5.28}$$

As the parameters $\boldsymbol{\theta}$ and $\boldsymbol{\varphi}$ are varied, $\boldsymbol{\sigma}_{\boldsymbol{I}}$ and $\boldsymbol{\sigma}_{\boldsymbol{II}}$ trace out two orthogonal non-intersecting geodesics I & II on the $\mathbf{SU(2)}$ manifold as illustrated schematically in Fig. 5.2(b). The projection of matrix $\boldsymbol{W}$ to the nearest member $\boldsymbol{W}_*$ of its equivalence class to a target matrix $\boldsymbol{V}$ is visualized in Fig. 5.2(c) as the problem of finding $\boldsymbol{B} = \boldsymbol{W}_*\boldsymbol{W}^\dagger$ the nearer of the nearest element of geodesic I or II to $\boldsymbol{A} = \boldsymbol{V}\boldsymbol{W}^\dagger$. It is clear that the tangent vector to the geodesic through $\boldsymbol{A}$ and $\boldsymbol{B}$ must be orthogonal to the tangent vector to geodesic I or II at $\boldsymbol{B}$.

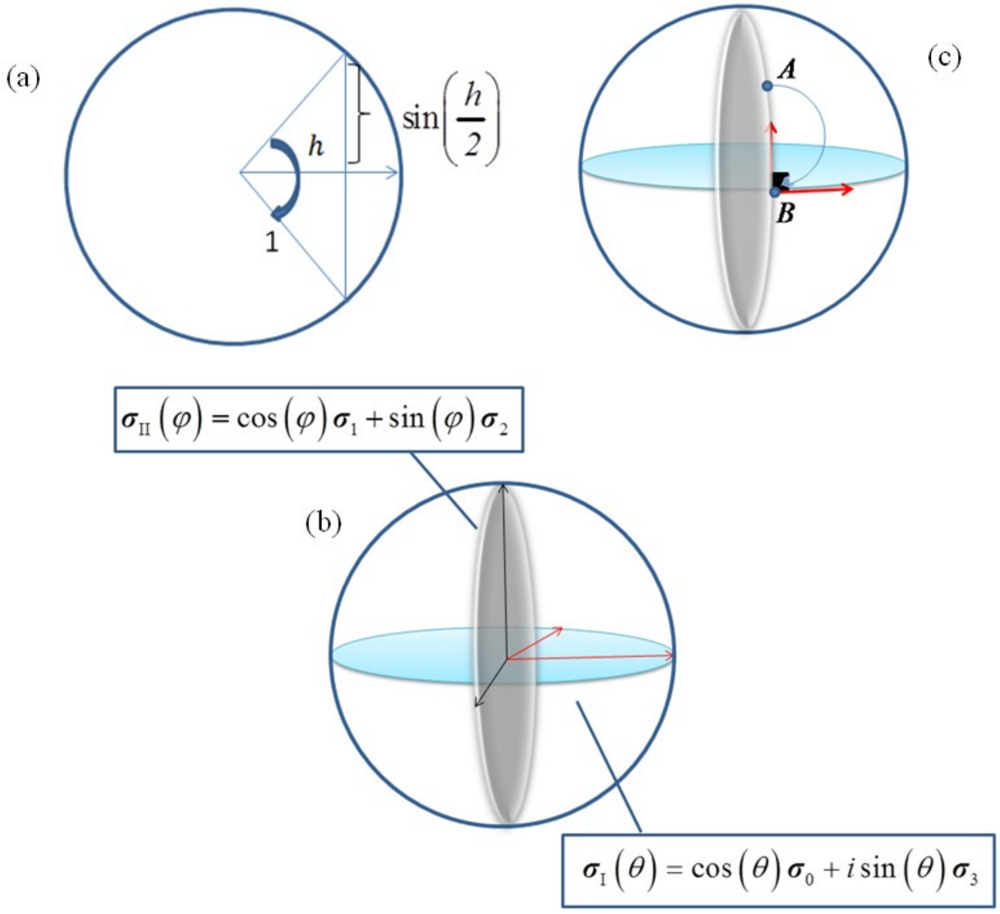

Figure 5.2. (a) Chord length corresponding to the arc length, (b) two orthogonal non-intersecting geodesics $\boldsymbol{\sigma}_{\mathbf{I}}$ and $\boldsymbol{\sigma}_{\mathbf{II}}$ on the manifold, (c) tangent vectors orthogonal to the geodesic I or II.

5.4.4 Complexity of the algorithm

The channel alignment algorithm involves: multiplications and additions associated with the Frobenius inner product and matrix multiples – these are of complexity at most N^2, and an exhaustive search through N! eligible permutations. The latter limits the algorithm to modest values of N for which it is feasible to parallelize the search and matrix multiplies thereby achieving O(1) computation time. Fortunately for SOP tracking $\mathrm{N} = 2$ which is small. As far as the authors are aware there is no comparable 'conventional' technique – channel alignment is conventionally corrected at higher levels in the communications protocol stack via header inspection and mechanisms for the discard of corrupted packets and packet retransmission. The algorithm described in the chapter substantially reduces the burden on these mechanisms and hence the latency / jitter they otherwise contribute. However, while the permutation alignment method intends to preserve continuity in the order of extracted sources, the initial order can be any permutation of the sources amongst the output ports. It is therefore necessary that the sources can be identified and correctly sorted. This must occur at a higher level in the protocol stack via a packet inspection to identify the source (e.g. the source address in a data link frame (Ethernet MAC address) and/or IP source address and/or TCP port etc.)

5.5 Simulation results and discussion

First, this tracking method is evaluated by simulation. N samples of two independent DQPSK signals with pseudo-random binary real and imaginary parts are generated to represent the initial orthogonally polarized signals. The DQPSK modulation format is used to overcome the ambiguity due to the unknown orientation of the constellation. These are then mixed using a Jones matrix $\boldsymbol{U}$ that changes during the course of the simulation. Random environmentally induced perturbations of a fiber cause the Jones matrix to follow, as function of propagation distance, a Brownian motion [181-183] on the $\mathrm{SU}(2)$ manifold. The state of polarization of the light exiting a sufficient length of fiber in an ensemble will be uniformly distributed over the Poincaré sphere and uncorrelated with the initial state of polarization. Over a sufficient length of time similar behavior may be expected in time of the exit state of polarization of a single strand of fiber. Accordingly, in the simulation, random vectors in $\mathbb{R}^3$ with normally-distributed independent zero-mean unit-variance elements are generated to construct, via the Pauli matrix basis for the Lie algebra $\mathrm{su}(2)$ of two-dimensional traceless Hermitian matrices, a tangent vector to the Lie group $\mathrm{SU}(2)$. This tangent vector is used to generate a short path segment on $\mathrm{SU}(2)$ via the exponential map with parameter δt that links the previous Jones matrix to the next Jones matrix thereby generating N samples of a discrete approximation to Brownian motion on $\mathrm{SU}(2)$.

The record length is limited to $\mathrm{N} = 10^5$ in consideration of computing resources. To ensure the state of polarization follows a path that covers a good proportion of the Poincaré sphere over the record, a step parameter $\delta t = 0.01$ is used. Visualizations of the Brownian motion of the state of polarization on the Poincaré sphere are shown in Figs. 5.3(a)-5.3(d). For a bit rate of 100 Gbit/s, the number of samples N corresponds to a record length of $1\,\mu s$ over which time in most applications the state of polarization would be essentially static. The simulated polarization drift is therefore an aggressive test of the robustness of the algorithm.

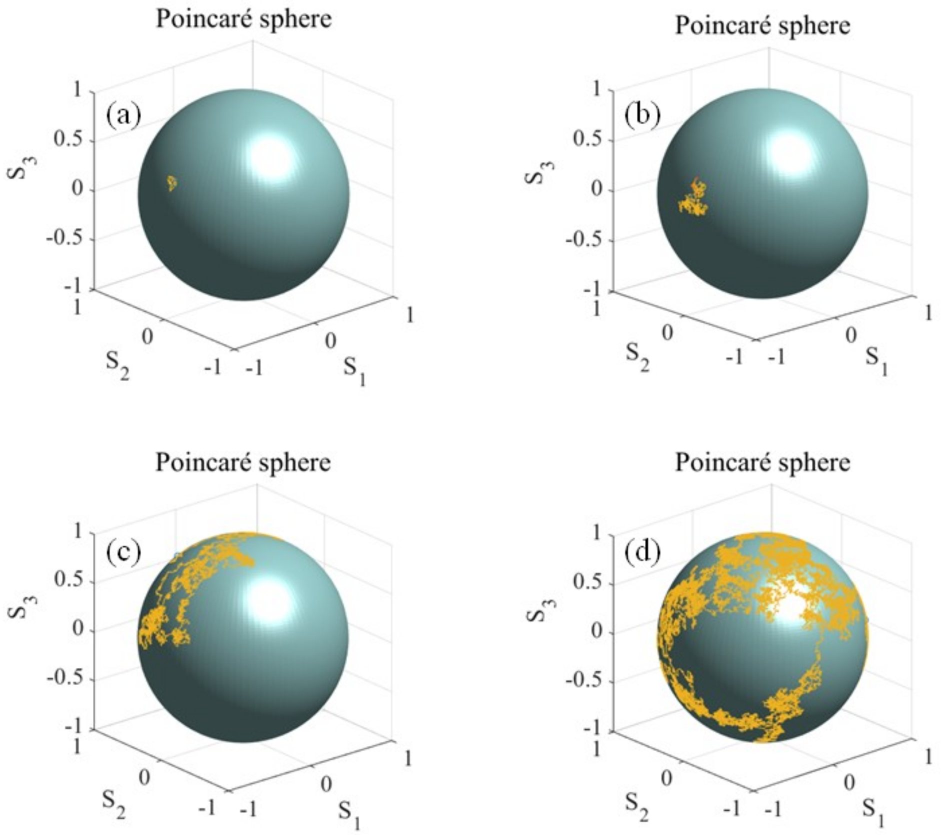

Fig. 5.3. Evolution of simulated states of polarization (SOP) on the Poincaré sphere for (a) 100, (b) 1000, (c) 10000, and (d) 100000 samples

White Gaussian noise is added to the mixed signals to simulate the two components, TE & TM, of polarization detected at the receiver. The signal power to total noise power ratio is set to 14.77 dB for each channels. The ICA code, which searches for a recovery matrix $\boldsymbol{V}$, for separating 2 sources in presence of unknown noise [184], is then applied to obtain the recovery matrix from a moving window of TE and TM signal samples. These data are used internally to the ICA code to estimate the higher order statistics. The choice of window length is a compromise. The window used must be short enough that the signal is essentially stationary and the estimates are not rendered inaccurate due to changes in polarization state within the window. Yet the window should be long enough that the estimates have small variance. The fluctuations of the state of polarizations in the simulation are aggressive, and an optimum window length was found to be 100 samples. In most applications the changes in polarization state are much more benign and larger windows of uncritical length may be used. The ICA module is then followed by the ambiguity tracking method as described in the preceding.

In Figs. 5.4(a) and 5.4(b), the output signal power of the TE and TM channels at the receiver before polarization de-multiplexing are shown and illustrate the fading that is caused by the fluctuating polarization state. Figs 5.4(c) and 5.4(d) show the polarization de-multiplexed signal power after the diversity combiner with and without the channel alignment algorithm and illustrate that the deep fading is successfully eliminated and, as expected, the algorithm is insensitive to additive white Gaussian noise. Errors in the recovery matrix due to the variance in the estimates of the high order signal statistics are responsible for the fluctuations in the combined signal power. The tracking algorithm can be seen to reduce somewhat the larger deviations in the combined power fluctuation.

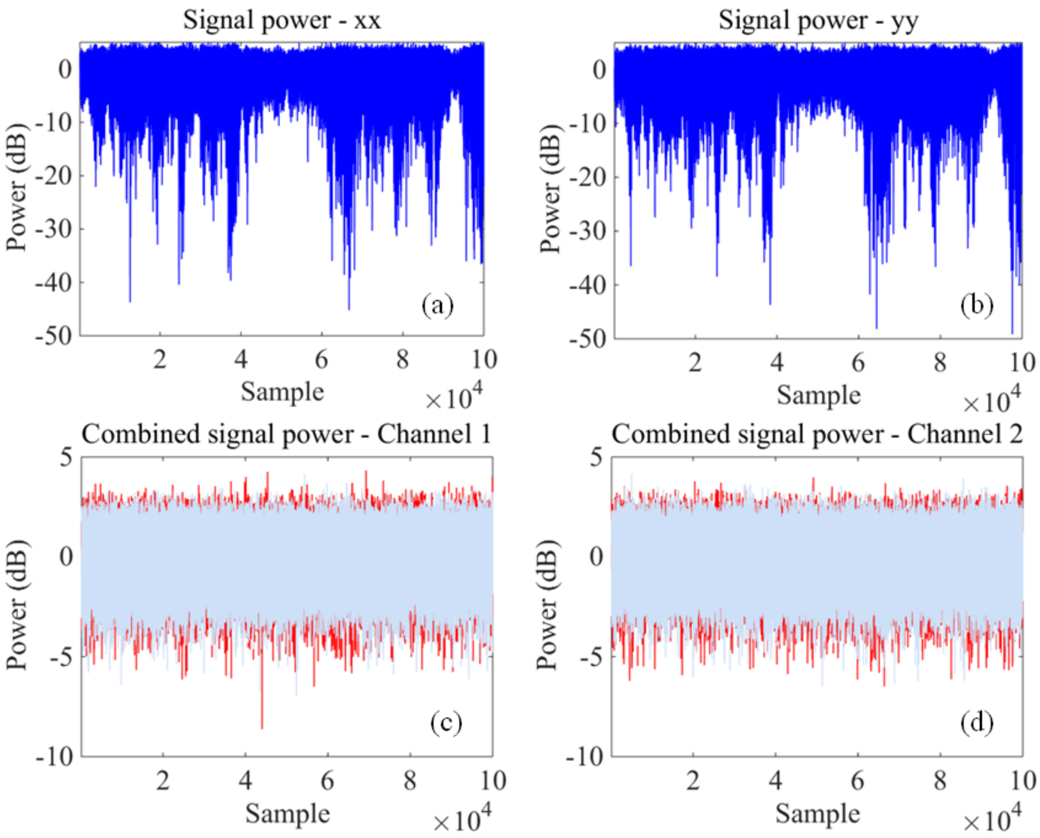

Fig. 5.4. Signal power of (a) channel 1 and (b) channel 2 before diversity combining. Combined signal power after applying ICA algorithm with and without proposed projection method are shown in gray and red respectively in (c) and (d).

To appreciate the major benefit of the tracking algorithm, the alignment of the de-multiplexed channels is detected by comparing the recovery matrix to the known mixing matrix by evaluating the invariant metric $\rho_D(\boldsymbol{W}, \boldsymbol{\sigma U})$ to determine if it is minimized by the choice $\boldsymbol{\sigma} = \boldsymbol{\sigma}_0$ (orientation +1) or $\boldsymbol{\sigma} = \boldsymbol{\sigma}_1$ (orientation -1). Figure. 5.5 demonstrates that frequent changes in channel alignment are eliminated with the application of the proposed method and perfect alignment tracking is achieved.

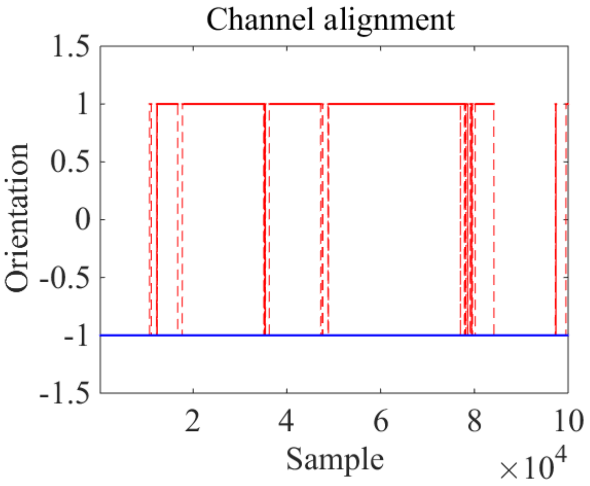

Fig. 5.5. Channel alignment using ICA method before and after applying the proposed projection algorithm are shown in red and blue respectively.

The signal can be demodulated as perfect channel alignment is established. Carrier phase tracking is necessary to demodulate QPSK but it is not necessary to demodulate DQPSK. Nevertheless it is applied in the simulation in order to visualize a static constellation and is carried out for each channel by applying the Viterbi and Viterbi phase estimation algorithm [185,186] to each output signal s, from the diversity combiner:

$$\bar{s} = s\,exp\left[-j\frac{1}{4}arg(s^4)\right] \qquad \textit{Equation 5.29}$$

This is followed by the decision on the demodulated symbol. Error free data recovery for the DQPSK modulation format is achieved. The constellations are shown in Figs. 5.6 (a) and 5.6(b) for channel 1 and channel 2.

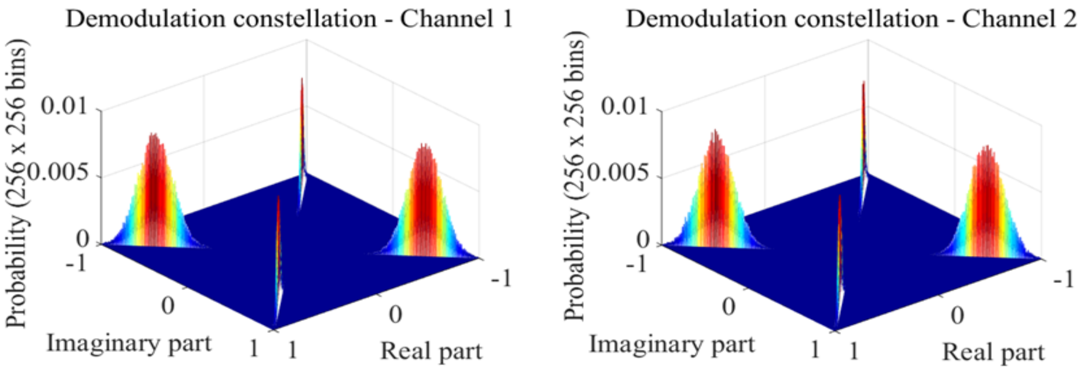

Fig. 5.6.Constellation of the demodulated signal using ICA algorithm with proposed projection method for (a) channel 1 and (b) channel 2 for SNR of 14.77 dB.

5.6 Experimental results

To test the proposed tracking channel alignment algorithm, a 40 Gb/s dual-polarization multiplexed communication system has been setup. The data are transmitted on two orthogonal polarizations of a standard single-mode fiber (SMF) simultaneously, using two independent pseudo-random binary sequences (PRBS). Two independent QPSK signals generated by two independent $2^7 - 1$ PRBS patterns with a symbol rate of 10 GBd are transmitted, where the signals are amplified, filtered and coherently detected using a commercial optical modulation analyser (OMA, Agilent N4391A). The experimental setup for data transmission and coherent detection are depicted in Fig. 5.7. The internal local oscillator (LO) laser is used in the OMA for best long term test results. For each point on the in-phase and quadrature (IQ) trace to represent a single symbol, the digital demodulator has been setup for 1 point/symbol. As a quantitative measure of the signal quality, the error vector magnitude (EVM), which defines how far a received symbol is from its desired position in the constellation diagram, is employed. As the OMA software can also perform a BER measurement, performing a BER measurement on the OMA, allows us to verify that the known generated pattern is being properly detected by the OMA. The reference pattern has been defined to check that the Optical OMA software accurately recognizes the input pattern. Once the pattern is defined and the BER measurement activated, the low-error measurement that recognizes the transmitted pattern is obtained. Measuring the signal directly at the output of the transmitter verifies the coherent receiver performance. The coherent receiver detects four electrical signals named I_x, Q_x, I_y, and Q_y which are the in-phase and quadrature components of the two polarization components of the electrical field as shown in Fig.5.8.

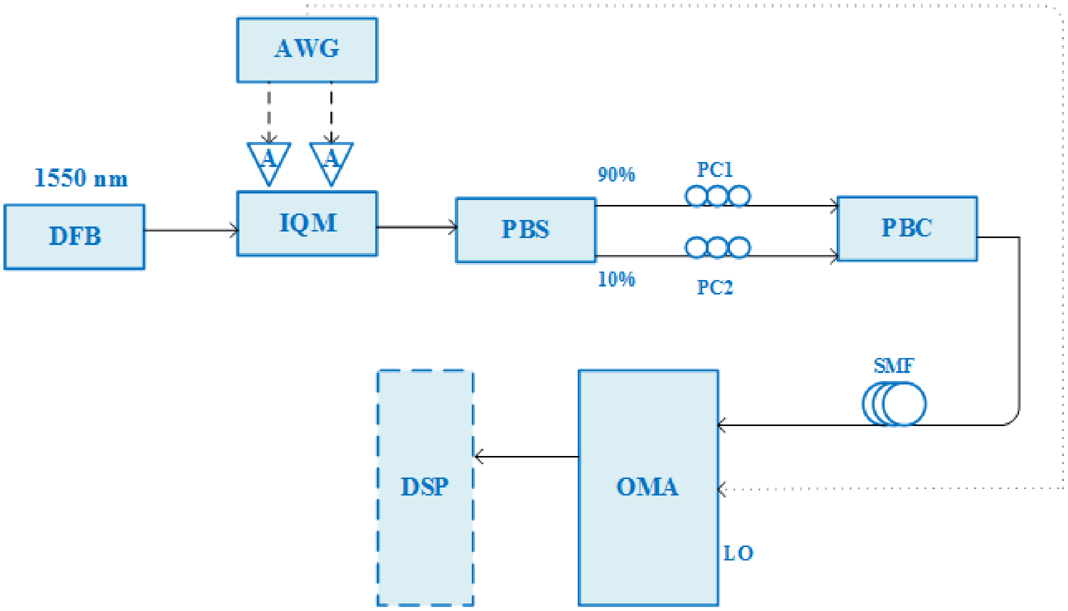

Fig. 5.7. Experimental setup for testing the tracking channel alignment algorithm. (DFB – distributed feedback laser, AWG – arbitrary waveform generator, A– amplifier, IQM – in-phase quadrature modulator, PBS – polarization beam splitter, PC– polarization controller, SMF– Single Mode Fiber, LO – local oscillator, OMA– optical modulation analyzer, DSP – digital signal processing).

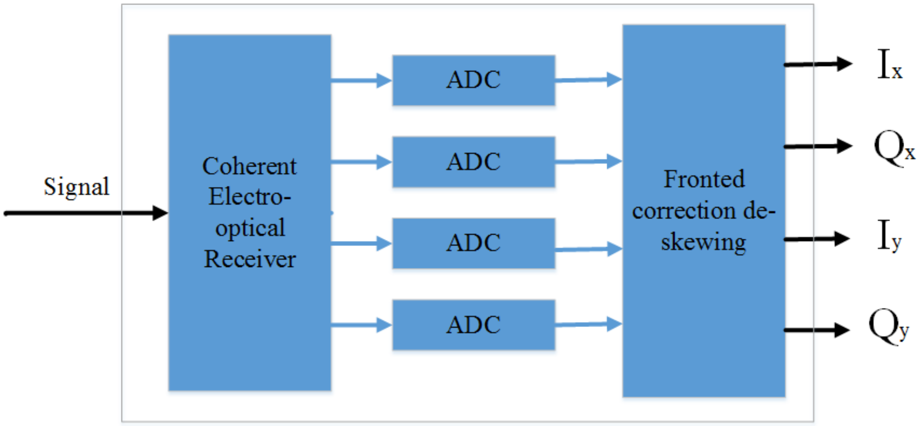

Fig. 5.8. Principle of signal flow of the N4391A

Through offline DSP, the CMA algorithm is used for generating the polarization de-multiplexed data which are then input to the module for testing the proposed channel alignment algorithm. In order to test the proposed algorithm, in addition to the back-to-back configuration, the signal is transmitted over a span of 5 km single mode fiber (SMF). Figure. 5.9 presents the different stages of DSP applied to the detected signal. For a QPSK signal, to obtain acceptable equalization through CMA algorithm the symbols should all lie on a ring. Applying the channel alignment method which is described in the preceding, yields in perfect channel alignment with attainment of low-error recovered constellation diagrams for both polarizations. The results show that the proposed algorithm is able to decrease the error vector magnitude (EVM) in recovery of constellation by 5% for channel 1 and 10% for channel 2 in the B2B scheme. Using a 5 km SMF, 16% and 18% reduction in EVM are obtained in demodulating constellation of channel 1 and channel 2 respectively using the proposed algorithm.

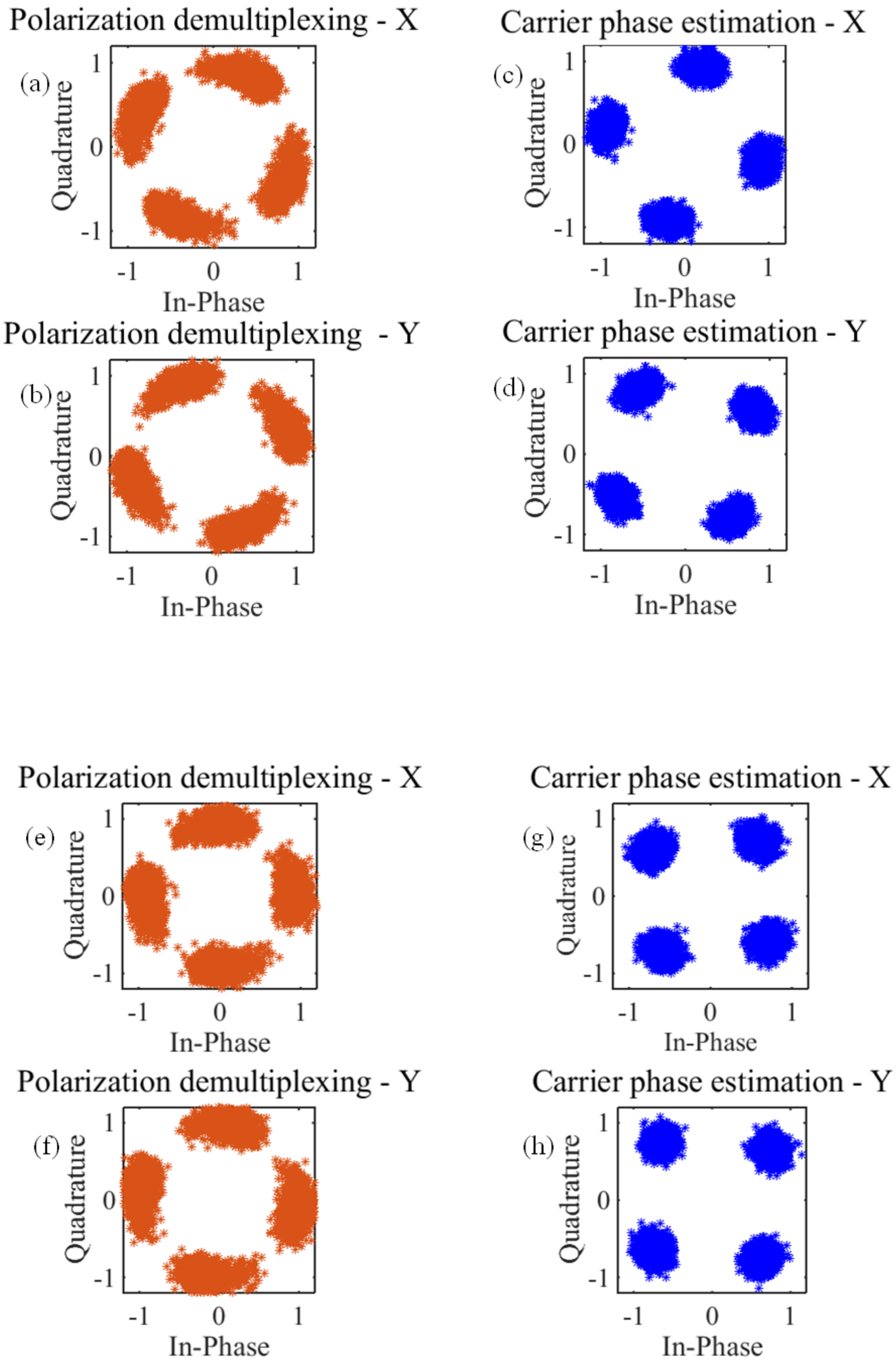

Fig. 5.9. Constellation of the demodulated signal using CMA algorithm for (a) polarization X , (b) polarization Y. (e) and (f) are the counterparts of (a) and (b) using CMA-modified algorithm. Constellation of the demodulated signal after carrier phase estimation of polarization de-multiplexed signals using CMA for (c) polarization X and (d) polarization Y. (g) and (h) are the counterparts of (c) and (d) after carrier phase estimation of de-multiplexed signals using modified CMA. Projection method shows improvement in recovery of the constellation diagram of the received signals for both channels. The SNR of channel 1 and channel 2 are measured as 12.6 dB and 10.8 dB respectively.

5.7 Discussion

This manuscript presents a proposed modification of the ICA/CMA algorithm for equalizers that overcomes ambiguities in the output state, in order to provide accurate polarization demultiplexing. Polarization dependent loss (PDL) and polarization dependent gain (PDG) are an issue only for the demultiplexing algorithm, if that algorithm succeeds, the algorithm described in the chapter will successfully track the channel alignment. The effect of PDL/PDG encountered in practice is negligible for ICA as it demultiplexes mixed signals on the basis of their independence and not according to their strength. CMA requires that the demultiplexed signals have constant modulus and may be more sensitive to PDL/PDG. It is however the most favorite commonly deployed algorithm. Rather large PDL was introduced in our experiments by the use of 90:10 splitters. The SOP evolution in our simulations is far more aggressive than encountered in practice. If an algorithm works in the presence of aggressive perturbations, for sure, it will work in a benign reality. The performance of the projection algorithm does not change with OSNR. But the constellation diagram of the recovered signal will be affected by the OSNR. To present an error free constellation diagram the SNR is set to 14.77 dB. For SNR of 12 dB and even lower, there was absolutely no effect on the performance of projection algorithm except the error in the recovered constellation.

The SU(2) mixing matrix is parameterized by three angles which may vary in practice at speeds of the order 10 krad/s The simulations employ one sample per symbol, if the bit rate is 25 Gbits/sec then each sample occurs every 40 ps. Hence, the polarization variation speed corresponds to 0.4×10^{-6} radians per sample. Over 10,000 samples the accumulated polarization parameter change will be less than 0.004 radians – i.e. an essentially static SOP over the record. Even increasing the suggested rate by two orders of magnitude leads to a lower variation of SOP than employed in the simulations. Therefore the variation of SOP in the simulation is far more aggressive than benign reality.

5.8 Conclusion

Due to the random birefringence of optical fiber, two input polarizations will be mixed at the receiver. To successfully recover the transmitted data, polarization de-multiplexing is necessary. In digital coherent optical receivers at the diversity combiner, any blind de-multiplexing method enables the system to recover input polarizations up to an inherent permutation ambiguity. The elimination of this drawback is possible through the projection onto the equivalent class method presented in this chapter. This technique enables accurate tracking of polarization channel alignment in dual polarized coherent optical transmission systems. Perfect maintenance of channel alignment and accurate recovery of the constellations is attained even with changes in SOP far more aggressive than is expected in practice. Experimental results show a great improvement in channel alignment using the proposed algorithm.

6 Chapter: Conclusions

6.1 Summary

The model of the channel is fundamental for understanding phase and polarization drift, chromatic dispersion, polarization mode dispersion and other drawbacks of the fiber optic systems in order for the signal processing algorithm to compensate these effects. Generally, signal processing is concerned with an inverse problem – from a set of noisy measurements inferring the source that gave rise to the measurements. The solution of an inverse problem requires an understanding of the direct problem-given a source what would be measured - and a priori knowledge that enables the class of all possible sources and noise processes to be restricted, e.g. to the most probable. Therefore, in chapter 2, the evaluation of the optical channel model that accurately describes the single mode fiber as a coherent transmission medium is reviewed through analytical, numerical and experimental analysis. We used the numerical modeling of the optical transmission medium and experimental measurements to determine the polarization drift as a function of time for a fixed length of fiber. The probability distribution of the birefringence vector was derived, which is associated to the "Poole" equation. The theory and experimental evidence that has been disclosed in the literature in the context of polarization mode dispersion – Stokes & Jones formulations and solutions for key statistics by integration of stochastic differential equations has been investigated. Besides in-depth definition of the single-mode fiber-optic channel, we reported a few alternative models and discussed their suitability for system design and performance evaluation. The modeling which concerns an ensemble of fibers each with a different instance of environmental perturbation has been analyzed. In chapter 3 an improved coherent optical receiver architecture that compensates for a random drift in the state of polarization (SOP) of both the signal and the local oscillator (LO) is presented for the first time. The proposed architecture comprises two conventional coherent optical receiver front-ends in tandem, where the SOP of the LO is first divided into its two orthogonal components and then distributed to each coherent optical receiver front-end module. Two distinct methods of polarization diversity recovery of the modulation based on the MRC technique and an eigenvalue–eigenvector decomposition of the covariance matrix have been used to effectively recover the transmitted signal. The concept is validated by numerical simulations, where a differential quadrature phase-shift keyed (DQPSK) modulated signal with a random time-varying SOP is first generated. After its mixing with a LO also possessing a random time-varying SOP, the algorithms that have been developed are provided with eight input variables to be digitally processed. The constellation diagrams corresponding to the recovered DQPSK modulation obtained using the two polarization diversity methods are presented.

In order to design, analyze and evaluate new architectures for the digital coherent receiver within the RF-Cité, chapter 4 presents a digital coherent radio-over-fiber (RoF) system comprising a microwave photonic integrated circuit (MPIC) as the main building block is proposed. The multi-function MPIC circuit is analyzed to operate as a single-sideband (SSB) modulator and as an in-phase and quadrature modulator (IQM) of a baseband signal in the RoF downlink. The circuit is also analyzed in the uplink as an SSB of a 60 GHz frequency-shifted input. The performance of the MPIC is assessed through numerical simulations, computing the harmonic distortions in the SSB, as well as the error vector magnitude in the IQM and coherent RoF system. Obtained results illustrate the advantage of the proposed MPIC for heterodyne mixing by providing the upper and lower sidebands spatially located in distinct ports. Moreover, simulation results yield insights into the feasibility of the circuit as an IQM of both baseband and low-power intermediate frequency signals. A comparison of an OFDM system and a single carrier system employing the proposed circuit in the end-to-end transport of high data rate is presented through error vector magnitude calculations.

In chapter 5, blind de-multiplexing methods such as the constant modulus algorithm (CMA) or independent component analysis (ICA) are found to be an effective means of de-multiplexing dual polarization modulated optical signals mixed by the evolution of the polarization state on propagation through the transmission medium. However, the recovery matrix estimated by these methods has an inherent permutation ambiguity in the assignment of polarization channels to ports. As a consequence, frequent instances of channel alignment permutation can occur resulting in loss of data during system recovery. This chapter describes a method of maintaining the initial alignment by setting the diversity combiner weight matrix to a member of the equivalence class of the estimated recovery matrix that is the nearest to the previous weight matrix. The method is verified by computer simulation of de-multiplexing by ICA of dual polarization differential quadrature phase shift keyed coherent optical transmission subject to aggressive changes in polarization state as well as experimental investigation of de-multiplexed QPSK modulation by CMA. Perfect maintenance of channel alignment and accurate recovery of the constellations is achieved.

6.2 Future work

The methods and approaches discussed in this thesis have proved encouraging for future work. Some possible directions of where the continuation of this research might involve are as follows:

1. The results obtained in chapter 2 for the single mode fiber can be simply generalized to the multimode case. In the multimode case, the relevant group becomes SU(2n). The algebra is su(2n) for which the Gell-Mann matrices form a basis.
2. The channel alignment algorithm which is presented in chapter 5 can be generalized to the symmetric coherent optical receiver proposed in chapter 3 Hence, having both reference and signal SOP unknown and drifting, the symmetric coherent optical receiver can be extended to de-multiplex three sources over a four-mode coherent channel (two spatial modes –'reference' & 'signal' – each supporting two polarization modes).
3. For on-chip architecture that is proposed in chapter 4, the monitoring methods for fine adjustment of the chip can be investigated for frequency multiplication and translation of harmonics by design. Digital signal processing (DSP) algorithms can be utilized to create an optimized microwave photonic integrated circuit (MPIC) functionality toward automated frequency multiplication. These DSP algorithms can be formed on Discrete Fourier Transform (DFT) and optimization based algorithms (Greedy and gradient-based algorithms), which may be analytically derived and numerically compared based on the accuracy and speed of convergence criteria. Also, the utilization of a microwave photonic integrated

circuit (MPIC) as the core building block of the optical coherent RoF link both in downlink and uplink, combined with digital signal processing (DSP) may be lead to a new RoF scheme which demonstrated the feasibility to operate at the lower input RF power for longer length of fiber. Additionally, transmission capacity of the proposed RoF architecture may be improved by spatial multiplexing through multi-input and multi-output (MIMO) technologies and polarization multiplexing which offers the seamless conversion of 2 × 2 MIMO transmissions in the fiber section and the wireless section.

References

1. R. P. Dameri, "Defining an evaluation framework for digital cities implementation," International Conference on Information Society (i-Society 2012), pp. 466–470.
2. G. S. Yovanof, G. N. Hazapis, “An Architectural Framework and Enabling Wireless Technologies for Digital Cities & Intelligent Urban Environments,” wireless personal communications, **49**(3), 445–463, (2009)
3. T. J. Hall, R. Maldonado-Basilio, S. Abdul-Majid, J. Seregelyi, R. Li, I. Antolín-Pérez, H. Nikkhah, F. Lucarz, J. L. de B. de L. Tocnaye, B. Francasso, P. Pajusco, C. Kärnfelt, D. Bourreau, M. Ney, R. Gumeri, Y. Josse, and H. Liu, “Radio-over-Fiber access for sustainable Digital Cities,” Ann. Telecommun. - Ann. Télécommun. **68**(1–2), 3–21 (2013).
4. International Energy Authority, “World Energy Statistics” (2017)—Available at link: http://www.iea.org/statistics/.
5. S.G. Anders Andrae and T. Edler, “On Global Electricity Usage of Communication Technology: Trends to 2030,” Challenges **6**, pp. 117–157 (2015).
6. Y. Josse, B. Fracasso, G. Castignani and N. Montavont, "Energy-efficient deployment of distributed antenna systems with radio-over-fiber links," 2012 IEEE Online Conference on Green Communications (GreenCom 2012), pp. 7–13.
7. F. Idachaba, D. U. Ike, and O. Hope, “Future Trends in Fiber Optics Communication,” in Proceedings of the World Congress on Engineering (2014), Vol I.
8. M. Noshada, A. Rostami, “FWM minimization in WDM optical communication systems using the asymmetrical dispersion managed fibers”, Int. J. Light Elec. Opt. **123**(9), 758–760 (2012).
9. A. Flores, B. Tek and L Le Van-Etter, “How fiber can help make your network "greener",”, Cabling Installation & Maintenance Magazine, **21**(4) 2013.
10. J. P. McClymer, “Comparison of multimode and single-mode optical fibers for quasi-elastic light scattering,” Rev. Sci. Instrum. **61**(7), 2001-2002 (1990).
11. Cisco white paper, “Limitations of Transmission Distances over Multimode Fiber”, 2008 cisco system.
12. H. Kogelnik, “Theory of dielectric waveguides,” in *Integrated Optics*, T. Tamir, ed. (Springer, 1975), Ch. 2, pp. 13–81.
13. C.R. Menyuk, P.K.A. Wai, “Polarization evolution and dispersion in fibers with spatially varying birefringence,” J. Opt. Soc. Am. B **11**, 1288–1296 (1994).
14. K. Ho and J. Kahn,“Mode coupling and its impact on spatially multiplexed systems,” in *Optical Fiber Telecommunications* VI, (Elsevier, 2013), pp. 491–568.
15. H. A. Haus, B. E. Little, M. A. Popović, S. T. Chu, M. R. Watts, and C. Manolatou, “Optical resonators and filters,” in *Optical Microcavities*, ser. *Advanced Series in Applied Physics*, K. Vahala, ed. (Singapore: World Scientific, 2004).
16. S. G. Johnson, M. Ibanescu, M. Skorobogatiy, O. Weisberg, T. D. Engeness, M. Soljačić, S. A. Jacobs, J. D. Joannopoulos, and Y. Fink, "Low-loss asymptotically single-mode propagation in large-core OmniGuide fibers," Opt. Express **9**, 748–779 (2001).
17. J. P. Gordon and H. Kogelnik, “PMD fundamentals: Polarization mode dispersion in optical fibers,” Proc. Natl. Acad. Sci. U. S. A. **97**(9), 4541–4550 (2000).

18. C. D. Poole and R. E. Wagner, "Phenomenological approach to polarisation dispersion in long single-mode fibers," Electron. Lett. **22**(19), 1029–1030 (1986).
19. G. J. Foschini and C. D. Poole, "Statistical theory of polarization dispersion in single mode fibers," J. Lightw. Technol. **9**(11), 1439–1456 (1991).
20. D. Marcuse and C. Lin, "Low dispersion single-mode fiber transmission- the question of practical versus theoretical maximum transmission bandwidth," IEEE J. Quantum Electron. QE-**17**(6), 869–878 (1981).
21. I. Kaminow, "Polarization in optical fibers," IEEE J. Quantum Electron. **17**(1), 15–22 (1981).
22. S. J. Savory, G. Gavioli, R. I. Killey, and P. Bayvel, "Electronic compensation of chromatic dispersion using a digital coherent receiver," Opt. Express **15**, 2120–2126 (2007).
23. D. S. Ly-Gagnon, S. Tsukarnoto, K. Katoh, and K. Kikuchi, "Coherent detection of optical quadrature phase-shift keying signals with carrier phase estimation," J. Lightw. Technol. **24**(1), 12–21 (2006).
24. C. Laperle, B. Villeneuve, Z. Zhang, D. McGhan, H. Sun, and M. O'Sullivan, "Wavelength division multiplexing (WDM) and polarization mode dispersion (PMD) performance of a coherent 40Gbit/s dual-polarization quadrature phase shift keying (DP-QPSK) transceiver," in *Optical Fiber Communication Conference and Exposition and The National Fiber Optic Engineers Conference*, OSA Technical Digest Series (CD) (Optical Society of America, 2007), paper PDP16.
25. G. Charlet, J. Renaudier, M. Mardoyan, H. Tran, P. Bigo, and S. Salsi, "Efficient mitigation of fiber impairments in an ultra-long haul transmission of 40Gbit/s polarization-multiplexed data, by digital processing in a coherent receiver," in *Optical Fiber Communication Conference and Exposition and The National Fiber Optic Engineers Conference*, OSA Technical Digest Series (CD) (Optical Society of America, 2007), paper PDP17.
26. W. Shieh, W. Chen, and R. S. Tucker, "Polarisation mode dispersion mitigation in coherent optical orthogonal frequency division multiplexed systems," Electron. Lett. **42**(17), 996–997 (2006).
27. . S. Jansen, I. Morita, T. Schenk, and H. Tanaka, "Long-haul transmission of 16 x 52.5 Gbits/s polarization-division-multiplexed OFDM enabled by MIMO processing (Invited)," J. Opt. Netw. **7**(2), 173–182 (2008).
28. W. Shieh, "PMD-supported coherent optical OFDM systems," IEEE Photonics Technol. Lett. vol. **19**(3), 134–136 (2007).
29. W. Shieh, X. Yi, Y. Ma, and Y. Tang, "Theoretical and experimental study on PMD-supported transmission using polarization diversity in coherent optical OFDM systems," Opt. Express **15**(16), 9936–9947 (2007).
30. N. Cvijetic, L. Xu, and T. Wang, "Adaptive PMD Compensation using OFDM in Long-Haul 10Gb/s DWDM Systems," in *Conference on Optical Fiber Communication and the National Fiber Optic Engineers Conference* (2007), pp. 1–3.
31. I. B. Djordjevic, "PMD compensation in fiber-optic communication systems with direct detection using LDPC-coded OFDM," Opt. Express **15**(7), 3692–3701 (2007).
32. M. Mayrock and H. Haunstein, "PMD Tolerant Direct-Detection Optical OFDM System," in *33rd European Conference and Exhibition of Optical Communication* (2007), pp. 1–2.

33. S. J. Savory, “Digital Coherent Optical Receivers: Algorithms and Subsystems,” IEEE J. Sel. Top. Quantum Electron. **16**(5), 1164–1179 (2010).
34. J. E. Simsarian, J. Gripp, A. H. Gnauck, G. Raybon, and P. J. Winzer, “Fast-tuning 224-Gb/s intradyne receiver for optical packet networks.” *in* Optical Fiber Communication Conference*,* OSA Technical Digest (CD) (Optical Society of America, 2010), paper PDPB5.
35. S. J. Savory, “Digital filters for coherent optical receiver,” Optics Express **16**(2), 804–817 (2008).
36. I. Roudas, A. Vgenis, C. S. Petrou, D. Toumpakaris, J. Hurley, M. Sauer, J. Downie, J. C. Mauro, and S. Raghavan, “Optimal Polarization Demultiplexing for Coherent Optical Communications Systems,” J. Lightw. Technol. **28**(7), 1121–1134 (2010).
37. F.P.Guiomar,S.B.Amado,A.Carena,G.Bosco,A.Nespola, A. L. Teixeira, and A. N. Pinto, “Fully blind linear and nonlinear equalization for 100G PM-64QAM optical systems,” J. Lightw. Technol. **33**(7), 1265–1274 (2015).
38. S. Ziaie, N. J. Muga, F. P. Guiomar, G. M. Fernandes, R. M. Ferreira, A. Shahpari, , A. L. Teixeira, A. N. Pinto,, "Experimental Assessment of the Adaptive Stokes Space-Based Polarization Demultiplexing for Optical Metro and Access Networks," in J. Lightw. Technol. **33**(23), 4968–4974 (2015).
39. L. Liu, Z. Tao, W. Yan, S. Oda, T. Hoshida, and J. C. Rasmussen, “Initial tap setup of constant modulus algorithm for polarization de-multiplexing in optical coherent receivers,” in *Conference on Optical Fiber Communication* - includes post deadline papers (2009), pp. 1–3.
40. R. Maher, D. S. Millar, S. J. Savory, and B. C. Thomsen, “Widely Tunable Burst Mode Digital Coherent Receiver With Fast Reconfiguration Time for 112 Gb/s DP-QPSK WDM Networks,” J. Lightw. Technol. **30**(24), 3924–3930 (2012).
41. F. Vacondio, O. Rival, Y. Pointurier, C. Simonneau, L. Lorcy, J.-C. Antona, and S. Bigo, “Coherent receiver enabling data rate adaptive optical packet networks.” in *37th European Conference and Exposition on Optical Communications*, OSA Technical Digest (CD) (Optical Society of America, 2011), paper Mo.2.A.4.
42. Z. Yu, X. Yi, J. Zhang, M. Deng, H. Zhang, and K. Qiu, “Modified constant modulus algorithm with polarization demultiplexing in stokes space in optical coherent receiver,” J. Light. Technol. **31**(19), 3203–3209 (2013).
43. K. Kikuchi, “Performance analyses of polarization demultiplexing based on constant-modulus algorithm in digital coherent optical receivers,” Opt. Express **19**(10), 9868–9880 (2011).
44. X. Xie, F. Yaman, X. Zhou, and G. Li, “Polarization demultiplexing by independent component analysis,” IEEE Photon. Technol. Lett. **22**(11), 1041–1135 (2010).
45. C. D. Poole, J. H. Winters, and J. A. Nagel, “Dynamical equation for polarization dispersion,” Opt. Lett. **16**(6), 372–374 (1991).
46. W. T. Ireeta, V. Musara, L. Wu, and A. W. R. Leitch, “Statistical characterization of the output state of polarization in deployed single-mode fibers,” Opt. Lett. **35**(12), 2049–2051 (2010).
47. A. Bononi and A. Vannucci, “Statistics of the Jones matrix of fibers affected by polarization mode dispersion,” Opt. Lett. **26**(10), 675–677 (2001).

48. S. Betti, F. Curti, B. Daino, G. Demarchis, E. Iannone, and F. Matera, “Evolution of the bandwidth of the principal states of polarization in single-mode fibers,” Opt. Lett. **16**(7), 467–469 (1991).
49. F. Bruyère, “Impact of first-and second-order PMD in optical digital transmission systems,” Opt. Fiber Technol. **2**(3), 269–280 (1996).
50. O. Aso, “Measurement of a parameter limiting the analysis of the first-order polarization-mode dispersion effect,” Opt. Lett. **23**(14), 1102–1104 (1998).
51. M. Karlsson and J. Brentel, “Autocorrelation function of the polarization-mode dispersion vector,” Opt. Lett. **24**(14), 939–941 (1999).
52. P. K. A. Wai and C. R. Menyuk, “Polarization decorrelation in optical fibers with randomly varying birefringence,” Opt. Lett. **19**(19), 1517–1519 (1994).
53. Q. Hu and W. Shieh, “Autocorrelation function of channel matrix in few-mode fibers with strong mode coupling,” Opt. Express **21**(19), 22153–22165 (2013).
54. N. Gisin and B. Huttner, “Combined effects of polarization mode dispersion and polarization dependent losses in optical fibers,” Opt. Commun. **142**(1–3), 119–125 (1997).
55. M. Kavehrad and J. Salz, "Cross-polarization cancellation and equalization in digital transmission over dually polarized multipath fading channels," in AT&T Technical Journal, **64**(10), 2211-2245 (1985).
56. K. Kikuchi, "Fundamentals of Coherent Optical Fiber Communications," in J. Lightwave Technol. **34**(1), 157–179 (2016).
57. N. A. Gromov and V. I. Man’ko, “The Jordan–Schwinger representations of Cayley–Klein groups. II. The unitary groups,” J. Math. Phys. **31**(5), 1054–1059 (1990).
58. G. Arfken. “Mathematical Methods for Physicists,” 3rd ed. Orlando, FL: Academic Press, pp. 211-212, 1985.
59. C. D. Poole, J. A. Nagel, in *Optical Fiber Telecommunications*, I. P. Kaminow, T. L. Koch, eds. (Academic, San Diego, 1997), IIIA, pp 114–161.
60. A. Dobrogowska, “R-matrix, Lax pair, and multiparameter decompositions of Lie algebras,” J. Math. Phys. **56**(11), 113508 (2015).
61. M. Loeve. Probability Theory. (D. Van Nostrand Co., London. 3rd ed., 1963).
62. R. L. Stratonovich, “A new representation for stochastic integrals and equations,” SIAM J. Control, 4(2), 362–71 (1966).
63. H. Risken.”The Fokker-Planck Equation,” (Springer-Verlag, 1989).
64. K. Binmore, J. Davies, “Calculus Concepts and Methods,”.(Cambridge University Press, 200). p.190.
65. H. Georgi, “Lie Algebras in Particle Physics,” 2nd ed. (Westview Press, 1999).
66. A. P. T. Lau, Y. Gao, Q. Sui, D. Wang, Q. Zhuge, M. H. Morsy-Osman, M. Chagnon, X. Xu, C. Lu, and D. V. Plant, “Advanced DSP techniques enabling high spectral efficiency and flexible transmissions: toward elastic optical networks,” IEEE Signal Processing Magazine **31**(2), 82–92 (2014).
67. G. Goldfarb, and G. Li, “Chromatic Dispersion Compensation Using Digital IIR Filtering With Coherent Detection,” IEEE Photonics Technol. Lett. **19**(13), 969–971 (2007).
68. S. Tsukamoto, K. Katoh, and K. Kikuchi, “Unrepeated 20-Gbit/s QPSK transmission over standard single-mode fiber using homodyne detection and digital signal processing for dispersion compensation,” in *Optical Fiber Communication Conference/National Fiber Optic Engineers Conference*, (Optical Society of America, 2006), paper OWB4.

69. S. J. Savory, G. Gavioli, R. I. Killey, and P. Bayvel, “Electronic compensation of chromatic dispersion using a digital coherent receiver,” Opt. Express **15**, 2120–2126 (2007).
70. T. Xu, G. Jacobsen, S. Popov, J. Li, E. Vanin, K. Wang, A. T. Friberg, and Y. Zhang, “Chromatic dispersion compensation in coherent transmission system using digital filters,” Opt. Express **18**(15), 16243–16257 (2010).
71. M. Birk, P. Gerard, R. Curto, L. E. Nelson, X. Zhou, P. Magill, T. J. Schmidt, C. Malouin, B. Zhang, E. Ibragimov, S. Khatana, M. Glavanovic, R. Lofland, R. Marcoccia, R. Saunders, G. Nicholl, M. Nowell, and F. Forghieri, “Real-time single-carrier coherent 100 Gb/s PM-QPSK field trial,”. J. Light. Technol. **29**(4), 417–425 (2011).
72. J. C. Rasmussen, T. Hoshida, and H. Nakashima, “Digital coherent receiver technology for 100-Gb/s optical transport systems,” Fujitsu Sci. Tech. J. **46**(1), 63–71 (2010).
73. R. Borkowski, P. Johannisson, H. Wymeersch, V. Arlunno, A. Caballero, D. Zibar, and I. T. Monroy, “Experimental demonstration of the maximum likelihood-based chromatic dispersion estimator for coherent receivers,” .J. Opt. Fiber Tech. **20**, 158–162 (2014).
74. P. J. Winzer, G. Raybon, H. Song, A. Adamiecki, S. Corteselli, A. H. Gnauck, D. A. Fishman, C. R. Doerr, S. Chandrasekhar, L. L. Buhl, T. J. Xia, G. Wellbrock, W. Lee, B. Basch, T. Kawanishi, K. Higuma, and Y. Painchaud, “100-Gb/s DQPSK transmission: From laboratory experiments to field trials,” J. Light. Technol. **26**(20), 3388–3402 (2008).
75. R. Elschner, F. Frey, C. Meuer, J. K. Fischer, S. Alreesh, C. Schmidt-Langhorst, L. Molle, T. Tanimura, and C. Schubert, “Experimental demonstration of a format-flexible single-carrier coherent receiver using data-aided digital signal processing,” Opt. Express **20**(27), 28786–91 (2012).
76. T. Xu, J. Li, G. Jacobsenc, S. Popov, A. Djupsjöbacka, R. Schatz, Y. Zhang, and Polina Bayvel, “Field trial over 820 km installed SSMF and its potential Terabit/s superchannel application with up to 57.5-Gbaud DP-QPSK transmission,” Opt. Commun. **353**, 133–138 (2015).
77. H. Bulow, “Experimental Demonstration of Optical Signal Detection Using Nonlinear Fourier Transform,” J. Light. Technol. **33**(7), 1433–1439 (2015).
78. A. Leven, N. Kaneda, and S. Corteselli, “Real-time implementation of digital signal processing for coherent optical digital communication systems,” IEEE J. Sel. Top. Quantum Electron. **16**(5), 1227–1234 (2010).
79. J.-X. Cai, H. G. Batshon, H. Zhang, C. R. Davidson, Y. Sun, M. Mazurczyk, D. G. Foursa, O. Sinkin, A. Pilipetskii, G. Mohs, and Neal S. Bergano, “25 Tb/s transmission over 5,530 km using 16QAM at 5.2 b/s/Hz spectral efficiency,” Opt. Express **21**, 1555–1560 (2013).
80. Y-K. Huang, E. Ip, Z. Wang, M-F. Huang, Y.Shao, and T.Wang, “Transmission of Spectral Efficient Super-Channels Using All-Optical OFDM and Digital Coherent Receiver Technologies,” J. Lightw. Technol. **29**(24), 3838–3844 (2011).
81. Y. Ma, Q. Yang, Y. Tang, S. Chen, and W. Shieh, “1-Tb/s per channel coherent optical OFDM transmission with subwavelength bandwidth access,” in *Optical Fiber Communication Conference*, (Optical Society of America, 2009), paper PDPC1.
82. C. Liu, J. Pan, T. Detwiler, A. Stark, Y-T. Hsueh, G-K. Chang, and S. E. Ralph, "Joint digital signal processing for superchannel coherent optical communication systems," Opt. Express **21**(7), 8342–8356 (2013).

83. I. Roudas, A. Vgenis, C. S. Petrou, D. Toumpakaris, J. Hurley, M. Sauer, J. Downie, J. C. Mauro, and S. Raghavan, “Optimal Polarisation Demultiplexing for Coherent Optical Communications Systems,” J. Lightw. Technol. **28**(7), 1121–1134 (2010).
84. K. Kikuchi, “Optical Homodyne Receiver Comprising Phase and Polarisation Diversities with Digital Signal Processing,” in *IEEE/LEOS Summer Topical Meetings*, (2007), pp. 55–56.
85. Y. H. Cheng, T. Okoshi, and O. Ishida, “Performance analysis and experiment of a homodyne receiver insensitive to both polarisation and phase fluctuations,” J. Lightw. Technol. **7**(2), 368–374 (1989).
86. K. Kikuchi and S. Tsukamoto, “Evaluation of Sensitivity of the Digital Coherent Receiver,” J. Lightw. Technol. **26**(13), 1817–1822 (2008).
87. K. Kikuchi, “Coherent optical communications: historical perspectives and future directions,” in *High Spectral Density Optical Communication Technology*, M. Nakazawa, K. Kikuchi, and T. Miyazaki, eds. (Springer, 2010), Ch. 2.
88. S. J. Savory, “Digital filters for coherent optical receivers,” Opt. Express **16**(2), 804–817 (2008).
89. N. Nabavi, and T. J. Hall, “Recovering symmetry in optical digital coherent polarization diversity receiver,” in *Proceedings of Photonics Conference* (IEEE, 2015), pp. 289–290.
90. N. Nabavi, S. Abdul-Majid, and T. J. Hall, "Symmetric dual polarization diverse digital optical coherent receiver," in *Proceedings of Photonics North 2015* (IEEE, 2015), in press.
91. Y. Painchaud, M. Poulin, M. Morin, and M. Têtu, “Performance of balanced detection in a coherent receiver,” Opt. Express **17** (5), 3659–3672 (2009).
92. A. Meiyappan, P. -Y. Kam, and H. Kim, “A complex-weighted, decision-aided, maximum-likelihood carrier phase and frequency-offset estimation algorithm for coherent optical detection,” Opt. Express **20**(18), 20102–20114 (2012).
93. C. Xie, “WDM coherent PDM-QPSK systems with and without inline optical dispersion compensation,” Opt. Express **17**(6), 4815–4823 (2009).
94. A. J. Stark, P. Isautier, J. Pan, S. K. Pavan, M. Filer, S. Tibuleac, R. Lingle, R. de Salvo, and S. E. Ralph, “Advanced signaling technologies for high-speed digital fiber-optic links,” Appl. Opt. **53**(25), 5824-5840 (2014).
95. D. M. Pataca, L. H. H. de Carvalho, C. B. F. Adami, F. D. Simões, M. de. -L. Rocha, J. C. R. F. Oliveira, “Transmission of a 1.12Tb/s superchannel over 452 km fiber,” J. Microw. Optoelectron. Electromagn. Appl. **12**(2), 524–532 (2013).
96. H. Sun, K. -T. Wu, and K. Roberts, “Real-time measurements of a 40 Gb/s coherent System,” Opt. Express **16**(2), 873–879 (2008).
97. J. Dieudonné , “Foundations of modern analysis,” (Academic Press, 1969).
98. C. D. Poole and R. E. Wagner, “Phenomenological approach to polarisation dispersion in long single-mode fibers,” Electron. Lett. **22**(19), 1029–1030 (1986).
99. J. P. Gordon and H. Kogelnik, “PMD fundamentals: Polarization mode dispersion in optical fibers,” Proc. Natl. Acad. Sci. U. S. A. **97**(9), 4541–4550 (2000).
100. G. Li, “Recent advances in coherent optical communication,” Adv. Opt. Photonics **1**(2), 279–307 (2009).
101. R. Hui, B. Zhu, R. Huang, C. T. Allen, K. Demarest, and D. Richards, “Subcarrier multiplexing for high-speed optical transmission,” J. Lightw. Technol. **20**(3), 417–427 (2002).

102. S. J. Savory, “Digital filters for coherent optical receivers,” Opt. Express **16**(2), 804–817 (2008).

103. A. J. Viterbi and A. N. Viterbi, “Nonlinear estimation of PSK-modulated carrier phase with application to burst digital transmission,” IEEE Trans. Inf. Theory **29**(4), 543–551 (1983).

104. M. M. G. Krishna, J. Samuel, and S. Sinha, “Brownian Motion on a Sphere: Distribution of Solid Angles,” J. Phys. Math. Gen. **33**(34), 5965–5971 (2000).

105. J. Nissfolk, T. Ekholm, and C. Elvingson, “Brownian dynamics simulations on a hypersphere in 4-space,” J. Chem. Phys. **119**(13), 6423–6432 (2003).

106. T. Carlsson, T. Ekholm, and C. Elvingson, “Algorithm for generating a Brownian motion on a sphere,” J. Phys. A: Math. Theor. **43**, 505001 (2010).

107. A. Ghosh, J. Samuel, and S. Sinha, “A ‘Gaussian’ for diffusion on the sphere,” Europhys. Lett. **98**, 30003 (2012)

108. Y. Luo, T. Wang, S. Weinstein, M. Cvijetic and S. Nakamura, “Integrating optical and wireless services in the access network”, in *Optical Fiber Communication Conference/National Fiber Optic Engineers Conference*, (Optical Society of America, 2006), paper NThG1.

109. D. Novak and R. Waterhouse, “Advanced radio over fiber network technologies,” Opt. Express **21**(19), 23001–23006 (2013).

110. A. Nirmalathas, P. A. Gamage, C. Lim, D. Novak and R. Waterhouse, “Digitized radio-over-fiber technologies for converged optical wireless access network,” J. Lightw. Technol. **28**(16), 2366–2375 (2010).

111. X. N. Fernando, “Radio over Fiber for Wireless Communications: From Fundamentals to Advanced Topics,” (John Weiley & Sons, 2014), Ch. 1.

112. V. Sarup and A. Gupta, “A Study of various Trends and Enabling Technologies in Radio over Fiber (RoF) Systems,” Int. J. Light Electron Opt. **126**(20), 2606–2611, (2015).

113. M. C. R. Medeiros, R. Avo, P. Laurencio, N. S. Correia, A. Barradas, H. J. A. da Silva, I. Darwazeh, J. E. Mitchell, and P. M. N. Monteriro, “Radio over fiber access network architecture employing reflective semiconductor optical amplifiers,” in *ICTON Mediterranean Winter Conf.* (2007), pp. 1–5.

114. N. Pleros, K. Vyrsokinos, K. Tsagkaris and N. D. Tselikas, “A 60 GHz Radio-over-Fiber Network Architecture for Seamless Communication With High Mobility,” J. Lightw. Technol. **27(**12), 1957–1967 (2009).

115. N. J. Gomes, P. P. Monteiro, and A. Gameiro, “Next Generation Wireless Communications Using Radio over Fiber,” (John Wiley & Sons, 2012), Ch. 4.

116. C. Lim, A. Nirmalathas, M. Bakaul, P. Gamage, K.-L. Lee, Y. Yang, D. Novak, R. Waterhouse, “Fiber wireless networks and subsystem technologies,” J. Lightw. Technol. **28(**4), 390–404 (2010).

117. A. Stöhr, A. Akrout, R. Buß, B. Charbonnier, F. Van Dijk, A. Enard, S. Fedderwitz, D. Jäger, M. Huchard, F. Lecoche, J. Marti, R. Sambaraju, A. Steffan, A. Umbach, and M. Weiß, “60 GHz radio-over-fiber technologies for broadband wireless services,” J. Opt. Netw. **8(**5), 471–487 (2009).

118. M. Zhu, L. Zhang, J. Wang, L. Cheng, C. Liu, and G.-K. Chang, “Radio-over-fiber access architecture for integrated broadband wireless services,” J. Lightw. Technol. **31(**23), 3614–3620 (2013).

119. H. Li, J. Hajipour, A. Attar, and V. C. M. Leung, "Efficient HetNet implementation using broadband wireless access with fiber-connected massively distributed antennas architecture," IEEE Trans. Wireless Commun. **18(**3), 72–78 (2011).
120. Y.-T. Hsueh, M.-F. Huang, S.-H. Fan, and G.-K. Chang, "A novel lightwave centralized bidirectional hybrid access network: seamless integration of RoF with WDM-OFDM-PON," IEEE Photon. Technol. Lett. **23(**15), 1085–1087 (2011).
121. I. G. Insua, D. Plettemeier and C. G. Schäffer, "Simple remote heterodyne radio-over-fiber system for gigabit per second wireless access," J. Lightw. Technol. **28**(16), 2289–2295 (2010).
122. Y. Li, M. Bystrom, D. Yoo, S. M. Goldwasser, P. R. Herczfeld, "Coherent optical vector modulation for fiber radio using electrooptic microchip lasers," IEEE Trans. Microw. Theory Tech. **53(**10), 3121–3129 (2005).
123. T. J. Hall, R. Maldonado-Basilio, S. Abdul-Majid, J. Seregelyi, R. Li, I. Antolín-Pérez, H. Nikkhah, F. Lucarz, J. L. de B. de L. Tocnaye, B. Francasso, P. Pajusco, C. Kärnfelt, D. Bourreau, M. Ney, R. Gumeri, Y. Josse, and H. Liu, "Radio-over-Fiber access for sustainable Digital Cities," Ann. Telecommun. - Ann. Télécommun. **68**(1–2), 3–21 (2013).
124. T. R. Clark, S. R. O'Connor, and M. L. Dennis, "A phase-modulation I/Q-demodulation microwave-to-digital photonic link," IEEE Trans. Microw. Theory Tech. **58(**11), 3039–3058 (2010).
125. V. J. Urick, M. E. Godinez, P. S. Devgan, J. D. McKinney, and F. Bucholtz, "Analysis of an analog fiber-optic link employing a low-biased Mach–Zehnder modulator followed by an erbium-doped fiber amplifier," J. Lightw. Technol. **27(**12), 2013–2019 (2009).
126. D. Zibar, R. Sambaraju, A. C. Jambrina, R. Alemany, J. Herrera and, I. T. Monroy, "16 Gb/s QPSK wireless-over-fiber link in 75-110GHz band employing optical heterodyne generation and coherent detection," in *Proc. 36th European Conf. on Optical Communication,* (2010), paper Th. 9. B. 6.
127. M. Mohamaed, X. Zhang, B. Hraimel, and K. Wu, "Frequency sixupler for millimeter-wave over fiber systems," Opt. Express **16(**14), 10141–10151 (2008).
128. A. H. M. R. Islam, M. Bakaul, A. Nirmalathas, and G. E. Town, "Simplification of millimeter-wave radio-over-fiber system employing heterodyning of uncorrelated optical carriers and self-homodyning of RF signal at the receiver," Opt. Express **20**(5), 5707–5724 (2012).
129. Z. Zheng, Y. Li, J. Xiao, and L. Chen, "A Radio-over-fiber system with a novel scheme for optical local oscillator and mm-wave distribution," J. Inf. Technol. **12**(1), 229–233 (2013).
130. M. Mohamed, B. Hraimel, X. Zhang, M. N. Sakib, and K. Wu, "Frequency quadrupler for millimeter-wave multiband OFDM ultrawideband wireless signals and distribution over fiber systems," J. Opt. Commun. Netw. **1(**5), 428–438 (2009).
131. J. Ma, "5 Gbit/s full-duplex radio-over-fiber link with optical millimeter-wave generation by quadrupling the frequency of the electrical RF carrier," J. Opt. Commun. Netw. **3(**2), 127–133 (2011).
132. R. Maldonado-Basilio, M. Hasan, H. Nikkhah, S. Abdul-Majid, R. Guemri, F. Lucarz, J. L. de B. de la Tocnaye, and T. J. Hall, "Electro-optic up conversion mixer amenable to photonic integration," J. Mod. Opt. **62(**17), 1405–1411 (2015).

133. M. Hasan, R. Guemri, R. Maldonado-Basilio, F. Lucarz, J.-L. de Bougrenet de la Tocnaye, and T. Hall, “Theoretical analysis and modeling of a photonic integrated circuit for frequency 8-tupled and 24-tupled millimeter wave signal generation,” Opt. Lett. **39(**24), 6950–6953 (2014).

134. R. Maldonado-Basilio, M. Hasan, R. Guemri, F. Lucarz, and T. J. Hall, “Generalized Mach–Zehnder interferometer architectures for radio frequency translation and multiplication: Suppression of unwanted harmonics by design,” Opt. Commun. **354**, 122–127 (2015).

135. R. Maldonado-Basilio, N. Nabavi, K. Aulakh, M. Hasan, and T. J. Hall, “Photonic integrated circuit for millimeter-wave signal generation by frequency multiplication,” in *proceedings of Photonics Conference*, (IEEE, 2015), pp. 130–131.

136. IEEE Standard for Information Technology— Telecommunications and information exchange between systems Local and metropolitan area networks—Specific requirements. Part 15.3: Wireless Medium Access Control (MAC) and Physical Layer (PHY) Specifications for High Rate Wireless Personal Area Networks (WPANs) Amendment 2: Millimeter wave-based Alternative Physical Layer Extension, IEEE Std 802153c-2009 Amend. IEEE Std 802153-2003, pp. c1–187, Oct. 2009.

137. IEEE Standard for Information technology—Telecommunications and information exchange between systems Local and metropolitan area networks—Specific requirements Part 11: Wireless LAN Medium Access Control (MAC) and Physical Layer (PHY) Specifications Amendment 3: Enhancements for Very High Throughput in the 60 GHz Band, IEEE Std 802.11ad™, pp. 1–598, Dec, 2012.

138. J. Armstrong, “OFDM for Optical Communications,” J. Lightw. Technol. **27**(3), 189–204, (2009).

139. EN300744: Digital Video Broadcasting (DVB): Framing Structure, Channel Coding and Modulation for Digital Terrestrial Television, EN300744, Eur. Telecommun. Standards Inst. (ETSI), 1997, Sophia Antipolis, France.

140. IEEE Standard for Information Technology— telecommunications and information exchange between systems Local and metropolitan area networks—Specific requirements. Part 11: Wireless LAN Medium Access Control (MAC) and Physical Layer (PHY) specifications - Amendment 4: Enhancements for Very High Throughput for Operation in Bands below 6GHz, IEEE P802.11ac™, pp. 1–395, Dec. 2013.

141. IEEE Standard for Local and Metropolitan Area Networks Part 16: Air Interface for Fixed Broadband Wireless Access Systems, IEEE Std. 802.16-2004, 2004, (Revision of IEEE Std. 802.16-2001).

142. Y. Han and G. Li, “Coherent optical communication using polarization multiple-input-multiple-output,” Opt. Express, **13**, 7527–7534 (2005).

143. K. Kikuchi, "Optical homodyne receiver comprising phase and polarization diversities with digital signal processing," in IEEE/LEOS Summer Topical Meetings (2007), pp. 55–56.

144. K. Kikuchi, “Analyses of wavelength- and polarization-division multiplexed transmission characteristics of optical quadrature-amplitude-modulation signals,” Opt. Express, **19**, 17985–17995 (2011).

145. M. S. Faruk and K. Kikuchi, “Front-end IQ-error compensation in coherent optical receivers,” in Opto Electronics and Communications Conference (IEEE, 2012), pp. 156–157.

146. M. Nakazawa, K. Kikuchi, and T. Miyazaki, “Coherent optical communications: historical perspectives and future directions,” in High Spectral Density Optical Communication Technology (Springer, 2010).
147. J. Renaudier, G. Charlet, B. O. Pardo, H. Mardoyan, P. Tran, M. Salsi, and S. Bigo, “Experimental analysis of 100Gb/s coherent PDM-QPSK long-haul transmission under constraints of typical terrestrial networks,” in European Conference on Optical Communication, (Optical Society of America, 2008), paper Th.2.A.3,
148. H. Sun, K.-T. Wu, and K. Roberts, “Real-time measurements of a 40 Gb/s coherent system,” Opt. Express, **16**, 873–879 (2008).
149. T. Pfau, S. Hoffmann, R. Peveling, S. Bhandare, S. K. Ibrahim, O. Adamczyk, M. Porrmann, R. Noe, and Y. Achiam, “First real-time data recovery for synchronous QPSK transmission with standard DFB Lasers,” IEEE Photonics Technol. Lett. **18**, 1907–1909 (2006).
150. T. Pfau, S. Hoffmann, O. Adamczyk, R. Peveling, V. Herath, M. Porrmann, and R. Noé, “Coherent optical communication: Towards real time systems at 40 Gbit/s and beyond,” Opt. Express, **16**, 866–872 (2008).
151. I. Roudas, A. Vgenis, C. S. Petrou, D. Toumpakaris, J. Hurley, M. Sauer, J. Downie, J. C. Mauro, and S. Raghavan, “Optimal polarization demultiplexing for coherent optical communications systems,” J. Light. Technol. **28**, 1121–1134 (2010).
152. Z. Yu, X. Yi, J. Zhang, M. Deng, H. Zhang, and K. Qiu, “Modified constant modulus algorithm with polarization demultiplexing in stokes space in optical coherent receiver,” J. Light. Technol. **31**, 3203–3209 (2013).
153. K. Kikuchi, “Performance analyses of polarization demultiplexing based on constant-modulus algorithm in digital coherent optical receivers,” Opt. Express **19**, 9868–9880 (2011).
154. T. F. Portela, D. V. Souto, V. N. Rozental, H. B. Ferreira, D. A. A. Mello, and H. Griesser, “Analysis of signal processing techniques for optical 112 Gb/s DP-QPSK receivers with experimental data,” J. Microw. Optoelectron. Electromagn. Appl. **10**, 155–164 (2011).
155. J. Tang, J. He, J. Xiao, and L. Chen, “Blind polarization demultiplexing for quadrature amplitude modulation coherent optical communication systems using low-complexity and fast-converging independent component analysis,” Opt. Eng. **53**, 056118–056118 (2014).
156. Z. Ling, W. Yeling, H. Guijun, C. Yunpeng, S. Jian, and L. Li, “Polarization demultiplexing by recursive least squares constant modulus algorithm based on QR decomposition,” Opt. Laser Technol. **49**, 251–255 (2013).
157. J. Gao, X. Zhu, and A. K. Nandi, “Independent component analysis for multiple-input multiple-output wireless communication systems,” Signal Process. **91**, 607–623 (2011).
158. P. Comon, “Independent component analysis, A new concept?,” Signal Process. **36**, 287–314 (1994).
159. A.K. Nandi (Ed.) Blind Estimation using Higher-order Statistics (Springer, 2010).
160. L. Liu, Z. Tao, W. Yan, S. Oda, T. Hoshida, and J. C. Rasmussen, “Initial tap setup of constant modulus algorithm for polarization de-multiplexing in optical coherent receivers,” in *Optical Fiber Communication Conference* (Optical Society of America, 2009), paper OMT2.

161. R. Maher, D. S. Millar, S. J. Savory, and B. C. Thomsen, “Widely tunable burst mode digital coherent receiver with fast reconfiguration time for 112 Gb/s DP-QPSK WDM Networks,” J. Light. Technol. **30**, 3924–3930 (2012).

162. F. Vacondio, O. Rival, Y. Pointurier, C. Simonneau, L. Lorcy, J.-C. Antona, and S. Bigo, “Coherent receiver enabling data rate adaptive optical packet networks.” in European Conference on Optical Communication, (Optical Society of America, 2011), paper Mo.2.A.4.

163. K. Kikuchi, “Polarization-demultiplexing algorithm in the digital coherent receiver.” in *IEEE/LEOS Summer Topical Meetings* (2008), pp. 101–102.

164. S. Araki, S. Makino, Y. Hinamoto, R. Mukai, T. Nishikawa, and H. Saruwatari, “Equivalence between frequency domain blind source separation and frequency domain adaptive beamforming for convolutive mixtures,” EURASIP J. Appl. Signal Process. **11**, 1157–1166 (2003).

165. N. Murata, S. Ikeda, and A. Ziehe, “An approach to blind source separation based on temporal structure of speech signals,” Neucomputing, **41**, 1–24 (2001).

166. H. Sawada, R. Mukai, S. Araki, and S. Makino, “Polar coordinate based nonlinear function for frequency domain blind source separation,” IEICE Trans. Fund. E86-A(3), 590–596 (2003).

167. L. Parra and C. Spence, “Convolutive blind separation of nonstationary sources,” IEEE Trans. Speech and Audio Processing, **8**, 320–327 (2000).

168. L. Schobben and W. Sommen, “A frequency domain blind signal separation method based on decorrelation,” IEEE Trans. Signal Processing, **50**, 1855–1865 (2002).

169. H. Zhang, Z. Tao, L. Liu, S. Oda, T. Hoshida, and J. C. Rasmussen, “Polarization demultiplexing based on independent component analysis in optical coherent receivers,” in *European Conference on Optical Communication*, (Optical Society of America, 2008), paper Mo.3.D.5.

170. P. Johannisson, H. Wymeersch, M. Sjodin, A. S. Tan, E. Agrell, P. A. Andrekson, and M. Karlsson, “Convergence comparison of the CMA and ICA for blind polarization demultiplexing,” J. Opt. Commun. Netw. **3**, 493–501 (2011).

171. X. Xie, F. Yaman, X. Zhou, and G. Li, “Polarization demultiplexing by independent component analysis,” IEEE Photonics Technol. Lett. **22**, 805–807 (2010).

172. J. Gao, X. Zhu, H. Lin, and A. K. Nandi, “Independent component analysis based semi-blind I/Q imbalance compensation for MIMO OFDM systems,” IEEE Trans. Wirel. Commun. **9**, 914–920 (2010).

173. Y. Jiang, X. Zhu, E. G. Lim, H. Lin, and Y. Huang, “Semi-blind MIMO OFDM systems with precoding aided CFO estimation and ICA based equalization,” in *Proceedings of Global Communications Conference* (IEEE, 2013), pp. 3499–3503.

174. Z. Ding, T. Ratnarajah, and C. F. N. Cowan, “HOS-based semi-blind spatial equalization for MIMO Rayleigh fading channels,” IEEE Trans. Signal Process. **56**, 248–255 (2008).

175. N. Nabavi and Trevor J. Hall, “Symmetric signal and local oscillator polarization diverse coherent optical receiver,” Opt. Express **24**, 2391–2405 (2016).

176. A. Hyvarinen and E. Oja, “Independent component analysis: algorithms and applications,” Neural Netw. **13**, 411–430 (2000).

177. J. Eriksson, E. Ollila, and V. Koivunen, “Essential Statistics and Tools for Complex Random Variables,” IEEE Trans. Signal Process. 58, 5400–5408 (2010).

178. D. N. Godard, “Self-recovering equalization and carrier tracking in two-dimensional data communication system,” IEEE Trans. Commun, COM-28, 1867–1875 (1980).

179. Seb J. Savory, "Digital filters for coherent optical receivers," Opt. Express **16**, 804–817 (2008).

180. S. Fiori and T. Tanaka, “An algorithm to compute averages on matrix Lie groups,” IEEE Trans. Signal Process. **57**, 4734–4743 (2009).

181. J. Nissfolk, T. Ekholm, and C. Elvingson, “Brownian dynamics simulations on a hypersphere in 4-space,” J. Chem. Phys. **119**, 6423–6432 (2003).

182. T. Carlsson, T. Ekholm, and C. Elvingson, “Algorithm for generating a Brownian motion on a sphere,” J. Phys. A: Math. Theor. **43**, 505001 (2010).

183. A. Ghosh, J. Samuel, and S. Sinha, “A ‘Gaussian’ for diffusion on the sphere,” Europhys. Lett. **98**, 30003 (2012).

184. http://www.gipsa-lab.fr/~pierre.comon/matlab.html.

185. D. S. Ly-Gagnon, S. Tsukarnoto, K. Katoh, and K. Kikuchi, “Coherent detection of optical quadrature phase-shift keying signals with carrier phase estimation,” J. Light. Technol. **24**, 12–21 (2006).

186. A. J. Viterbi and A. N. Viterbi, “Nonlinear estimation of PSK-modulated carrier phase with application to burst digital transmission,” IEEE Trans. Inf. Theory, **29**, 543–551 (1983).